Fusion reactor systems*

F. L. Ribe

University of California, Los Alamos Scientific Laboratory, Los Alamos, New Mexico 87544

In this review we consider deuterium–tritium (D-T) fusion reactors based on four different plasma-confinement and heating approaches: the tokamak, the theta-pinch, the magnetic-mirror, and the laser-pellet system. We begin with a discussion of the dynamics of reacting plasmas and basic considerations of reactor power balance. The essential plasma physical aspects of each system are summarized, and the main characteristics of the corresponding conceptual power plants are described. In tokamak reactors the plasma densities are about 10^{20} m^{-3}, and the β values (ratio of plasma pressure to confining magnetic pressure) are approximately 5%. Plasma burning times are of the order of 100–1000 sec. Large superconducting dc magnets furnish the toroidal magnetic field, and 2-m thick blankets and shields prevent heat deposition in the superconductor. Radially diffusing plasma is diverted away from the first wall by means of null singularities in the poloidal (or transverse) component of the confining magnetic field. The toroidal theta-pinch reactor has a much smaller minor diameter and a much larger major diameter, and operates on a 10-sec cycle with 0.1-sec burning pulses. It utilizes shock heating from high-voltage sources and adabatic-compression heating powered by low-voltage, pulsed cryogenic magnetic or inertial energy stores, outside the reactor core. The plasma has a density of about 10^{22} m^{-3} and β values of nearly unity. In the power balance of the reactor, direct-conversion energy obtained by expansion of the burning high-β plasma against the containing magnetic field is an important factor. No divertor is necessary since neutral-gas flow cools and replaces the "spent" plasma between pulses. The open-ended mirror reactor uses both thermal conversion of neutron energy and direct conversion of end-loss plasma energy to dc electrical power. A fraction of this direct-convertor power is then fed back to the ion-injection system to sustain the reaction and maintain the plasma. The average ion energy is 600 keV, plasma diameter 6 m, and the plasma beta 85%. The power levels of the three magnetic-confinement devices are in the 500–2000 MWe range, with the exception of the mirror reactor, for which the output is approximately 200 MWe. In Laser-Pellet reactors, frozen D–T pellets are ignited in a cavity which absorbs the electromagnetic, charged particle, and neutron energy from the fusion reaction. The confinement is "inertial," since the fusion reaction occurs during the disassembly of the heated pellet. A pellet-cavity unit would produce about 200 MWt in pulses with a repetition rate of the order of 10 sec^{-1}. Such units could be clustered to give power plants with outputs in the range of 1000 MWe.

CONTENTS

* Work performed under the auspices of the U. S. Atomic Energy Commission.

I. INTRODUCTION

During the past several years there have been notable developments in research on controlled fusion reactor systems. In the magnetic-confinement experiments these were demonstrations of plasma temperatures approaching or exceeding that (50 000 000 K) necessary to initiate reactor operation, and of plasma confinement times which approach the "classical" ideal whereby the confining magnetic field penetrates the plasma and the plasma diffuses at a rate determined by particle (ion and electron) coulomb collisions.

In magnetic-confinement systems, the plasma is held by magnetic fields in the desired configurations for times large compared to disassembly times against characteristic sound or particle thermal speeds, and heating is done by gas-discharge techniques involving large plasma currents or rapidly increasing magnetic fields, as well as by injection with energetic beams of neutral atoms. A new principle for heating and confining plasmas–laser fusion–has also produced a major research activity. In laser fusion, the confinement is "inertial," being essentially the sound–thermal disassembly time. The heating, obtained by the interaction of intense beams of laser radiation with a small plasma pellet, is

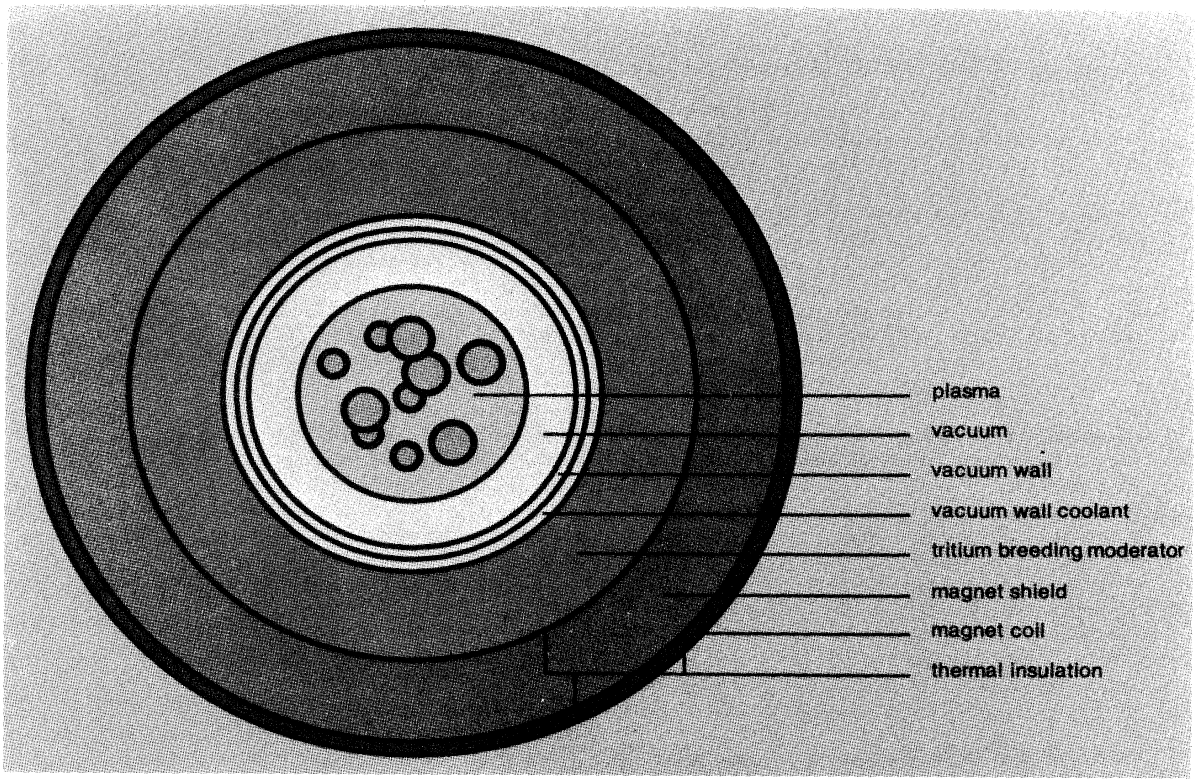

FIG. 1. Generalized cross section of a nuclear fusion reactor with magnetically confined plasma.

designed to take place within the short ($\approx 10^{-9}$ sec) disassembly time of the pellet, producing a microexplosion of fusion energy.

A recent development is the increasingly serious pursuit of conceptual fusion reactor designs based on the physical principles which characterize those experimental approaches which are generally recognized as having demonstrated significant degrees of plasma heating and confinement. In these reactor designs, heating and confinement are assumed to proceed in a more or less idealized fashion, consistent with known physical laws. The main questions addressed are those of the compatibility of the plasma properties with engineering feasibility in systems which are capable of producing electrical power at sufficiently high levels to be economical when compared with fossil fuel and nuclear fission systems. Typical problems are: materials integrity in the neutron and electromagnetic radiation environment and optimization of engineering components necessary for favorable power plant energy balance.

In the following, we shall briefly summarize the present status of conceptual reactor designs based on the tokamak diffuse toroidal pinch, the theta pinch, and the magnetic mirror, as predominant magnetic confinement systems, as well as the laser-pellet inertial-confinement system. Our approach will be primarily heuristic, attempting to relate each reactor system to physical principles of the basic thermonuclear plasma system. Relevant portions of the plasma physics are very briefly summarized, and the reader is referred to general reviews (Post, 1956, 1973; Leontovich, 1961; Rose and Clark, 1961; Artsimovich, 1964; Rose, 1971) as well as pertinent specific references. Summaries and reviews relating more specifically to fusion reactors are to be found in Rose (1969), Hall and Maple (1970), Ribe (1973), IAEA Workshop (1974), Draper (1974), Post and Ribe (1974).

II. BASIC CONSIDERATIONS

A. Typical reactor configurations and plasma parameters

Figure 1 is a generalized cross section of the core of a magnetic-confinement fusion reactor. The plasma, with temperature in excess of 100 000 000 K (correspondingly, T greater than 11.4 keV), is confined by magnetic fields (predominantly perpendicular to the plane of the figure) in excess of 5 T. Plasma ion and electron densities are in the range of 10^{20} m^{-3} for tokamak and mirror reactors, and 10^{22} m^{-3} for the theta-pinch reactor. The magnetic coil producing the magnetic field is protected from the nuclear radiation from the plasma by a moderator (often called the blanket) of the neutrons, by a magnet shield which absorbs neutrons and gamma rays, and by thermal insulation. In the case of a deuterium–tritium plasma, the moderator must breed tritium to replace that depleted as fusion reactions take place. The plasma is surrounded by vacuum or low-density plasma, the whole being contained in a vacuum vessel comprising the first wall. A coolant, consisting of flowing liquid metal, salt or high-pressure gas, removes heat deposited in the vacuum wall and blanket by nuclear and electromagnetic radiation from the plasma. The coolant transports this heat to the thermal-conversion equipment

(e.g., heat exchanges and turbogenerators) which produces electrical power.

A quantity of basic importance to fusion physics and reactor design is the ratio β of the kinetic pressure $p = 2nkT$ of the plasma ions and electrons to the pressure of the external confining magnetic field B perpendicular to the plane of Fig. 1

$$\beta = p/(B^2/2\mu_0) = 4\mu_0 nT/B^2. \qquad \text{(II.1)}$$

In present experiments, "low" β refers to values less than 0.01, and "high" β values lie between 0.1 and 1.0 (the maximum possible value).

A schematic view of a conceptual laser-pellet fusion-reactor core is shown in Fig. 2. Intense laser beams enter a cavity to irradiate a pellet of fusible material, initially in the form of cryogenically frozen deuterium and tritium. A thin layer of material, for example liquid lithium, protects the solid cavity wall from the impulse of the nuclear microexplosion by ablating. The lithium blanket absorbs 14-MeV neutrons from the fusion reactions, breeds tritium, and provides heat to the thermal-conversion equipment. The quantity β does not usually apply, since there is usually no confining magnetic field. Reacting plasma densities are in the range of 10^{31} to 10^{33} m^{-3} with temperatures in excess of 10 keV.

B. Nuclear fusion reactions

Those nuclear reactions which occur at the lowest plasma temperatures are listed in Table I. In this review we shall be concerned primarily with the deuterium–tritium (D–T) reaction for which ignition (cf., Sec. II.D) occurs at temperatures greater than 4–5 keV. The major fraction of the reaction energy is carried out of the plasma by the 14-MeV neutrons; most of the 3.5-MeV alpha particles remain in the plasma, depositing their energy as they slow down by collisions with (first) the electrons, and (finally) the deuterons and tritons (Butler and Buckingham, 1962). The two branches of the D–D reaction typically occur at approximately one percent of the D–T reaction rate at the temperatures and densities of D–T systems. Because of its high reaction rate at relatively low temperature, the D–T system is the most feasible for the first-generation fusion reactors considered here. Next-generation reactors will probably be based on the higher-temperature (~100 keV)

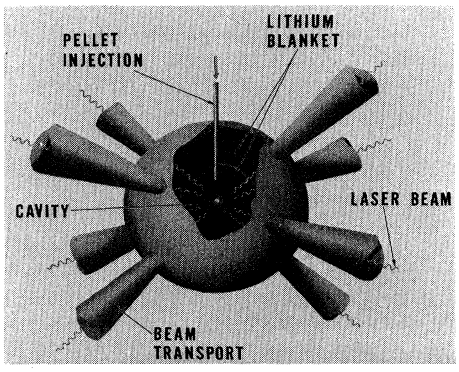

FIG. 2. Schematic view of a laser–pellet fusion reactor core.

TABLE I. Nuclear fusion reactions which occur at the lowest plasma temperatures. The quantities E and E^* refer to the total nuclear energy release in one reaction and to the energy released in the form of charged particles, respectively.

	$E(MeV)$	$E^*(MeV)$
(1) D + T → ^{4}He(3.52 MeV) + n(14.06 MeV)	17.58	3.52
D + D → ^{3}He(0.82 MeV) + n(2.45 MeV)	3.27	0.82
(2) D + D → T(1.01 MeV) + p(3.03 MeV)	4.04	4.04
(3) D + ^{3}He → ^{4}He(3.67 MeV) + p(14.67 MeV)	18.34	18.34
(4) T + T → ^{4}He + n + n	11.32	···

D–D system which requires no fuel breeding, and for which neutron activation of the reactor structure would be greatly reduced because of the smaller neutron energy, or a system based on the (~600 keV) D–^{3}He reaction, all of whose reaction products are charged. The D–^{3}He system would greatly reduce the need for thermal conversion of the nuclear energy to electrical work, since the reaction of the charged particles on magnetic and electrical fields can produce this work "directly," converting fusion energy at high efficiency. The T–T reaction occurs with a small reaction rate.

Figure 3 is a graph versus ion temperature T of the reaction rate parameter which is the product $\langle\sigma v\rangle$ of the D–T reaction cross section and the relative velocity of the D and T nuclei, averaged over a Maxwellian velocity distribution. If we assume equal number densities n of deuterons and tritons the thermonuclear power available from each m^3 of plasma for thermal conversion to electricity or some other form of work is

$$p_T = \tfrac{1}{4}n^2\langle\sigma v\rangle Q_T, \qquad \text{(II.2)}$$

where $Q_T = ME_n + E_\alpha$. Here E_n and E_α are the neutron and α-particle energies of Table I, and the quantity M is the blanket energy multiplication factor defined below. Substituting n from (II.1) we find

$$p_T = 0.62 \times 10^{29}\beta^2 B^4 Q_T\langle\sigma v\rangle/T^2 \quad \text{(W/m}^3\text{)}, \qquad \text{(II.3)}$$

where Q_T and T are in electron volts. The dependence on β^2 shows the importance of the quantity beta as a measure of utilization of magnetic-field energy in fusion reactors.

The basic nuclear reactions by which tritium is produced (bred) in excess of its consumption, by means of neutrons in the blanket (Fig. 1) of a D–T reactor are as follows:

$$^6\text{Li} + n = {}^4\text{He} + T + 4.80\ \text{MeV}$$
$$^7\text{Li} + n = {}^4\text{He} + T + n - 2.47\ \text{MeV}. \qquad \text{(II.4)}$$

The first reaction produces tritium by the capture of slow neutrons in ^{6}Li, while the second produces tritium by inelastic scattering of fast neutrons on nuclei of the more abundant ^{7}Li isotope, followed by subsequent decay of the ^{7}Li into tritons and α particles. The competition between these processes and neutron leakage and absorption processes, e.g., in nuclei of the metallic structure of the blanket, determines the breeding ratio T/n of tritons per 14-MeV neutron; in practical blanket structures this ratio is approximately 10% greater than unity. Another quantity of interest

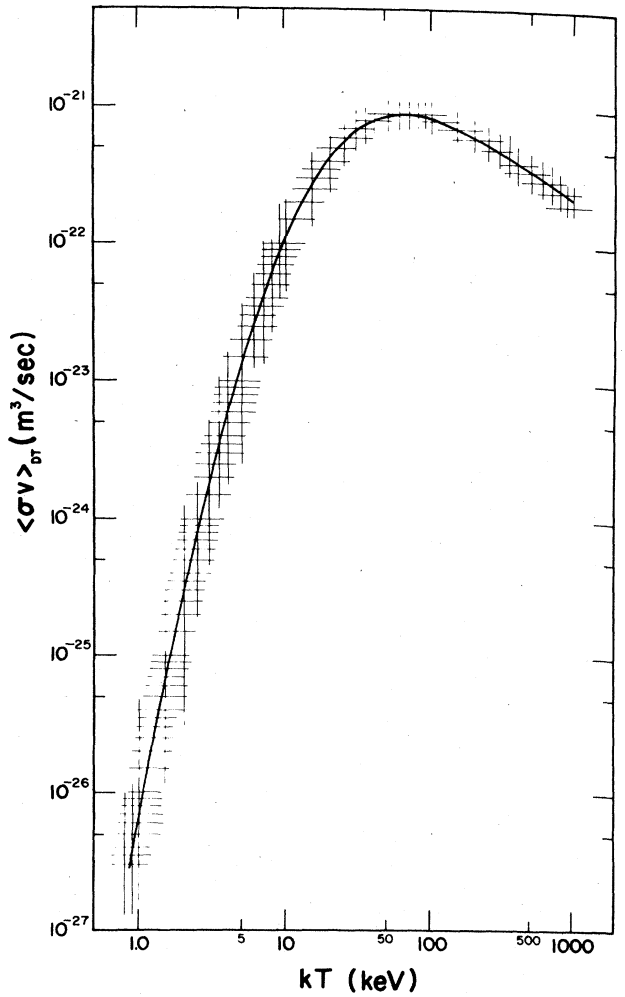

FIG. 3. The D–T reaction-rate parameter versus plasma ion temperature. The ordinate is the average over a Maxwellian velocity distribution of the product of the fusion reaction cross section and the relative deuterium–tritium velocity.

is the energy multiplication factor M of the reactor blanket. This quantity is the ratio of the mean energy produced in all nuclear reactions produced by a neutron, including contributions from secondary charged particles, neutrons and gamma rays, to the energy E_n with which the neutrons are incident on the reactor first wall.

It is also useful to define some quantities having to do with the passage of neutrons through the first wall and blanket of a reactor. We distinguish the uncollided 14-MeV neutrons incident on the first wall from those neutrons having a continuous spectrum of energies resulting from scattering and other nuclear reactions in the blanket and other structure. The *neutron current density* J, measured in neutrons/m²/sec, is a vector quantity measuring directed flow of neutrons across a unit area. *Neutron flux*, measured in neutrons/m²/sec, is a scalar quantity measuring the product of neutron density and velocity, regardless of direction. *Neutron fluence* is the time integral of the neutron flux. A primary reference quantity in reactor designs is the "wall loading" P_w/A, expressed in MW/m², which is the total energy carried through the first wall per unit of time by uncollided 14-MeV neutrons. The uncollided neutron current density at the first wall is given by

$$J_{uc} = 4.44 \times 10^{17} P_w/A. \quad \text{(n/m}^2\text{/sec)} \qquad \text{(II.5)}$$

C. Quantities affecting the plasma power balance

Assuming that all α particles, each of energy E_α, are absorbed by the plasma, the power deposited per unit volume of plasma is (Glasstone and Lovberg, 1960, p. 20)

$$p_\alpha = \tfrac{1}{4} n^2 \langle\sigma v\rangle E_\alpha \approx 5.3 \times 10^{-29} n^2 [\exp(-200/T_i^{1/3})/T_i^{2/3}] \quad \text{(W/m}^3\text{)}, \qquad \text{(II.6)}$$

where T_i (eV) is the (assumed) common temperature of the deuterons and tritons, each of which is assumed to have number density $n/2\,(\text{m}^{-3})$.

The bremsstrahlung power density (Spitzer, 1962, p. 148) for the range of n and T values appropriate to D–T reactors is given approximately by

$$p_{br} = 1.7 \times 10^{-38} n_i^2 Z^3 T_e^{1/2} \quad \text{(W/m}^3\text{)}, \qquad \text{(II.7)}$$

where Z is the ionic charge, n_i is the density of ions in m^{-3}, and T_e is the electron temperature in eV. This represents the total emission of all wavelengths of the continuum from the free–free energy transitions of the (optically thin) plasma electrons.

In case the electrons and ions have different kinetic temperature, the rate at which energy is lost from the higher-temperature species (assumed here to be the electrons) by means of coulomb collisions with the lower-temperature species is (Spitzer, 1962, p. 135)

$$p_{ei} = 0.76 \times 10^{-33} [n^2 \ln\Lambda (T_e - T_i)/A_i T_e^{3/2}]. \quad \text{(W/m}^3\text{)}. \qquad \text{(II.8)}$$

Here the quantity Λ is the ratio of the Debye shielding distance to the minimum impact parameter for electron–proton collisions (Spitzer, 1962, p. 127), and A_i is the mass of an ion relative to the proton mass. The ions are assumed to have unit charge.

At low plasma densities, low beta values, and high temperatures, the synchrotron radiation (Spitzer, 1962, p. 152) emitted by the electrons from their magnetic orbits is an important factor in the plasma power balance. An approximate expression derived for slab geometry (Rose, 1969) and generalized to use for plasma cylinders (Etzweiler, Clarke and Fowler, 1973) is

$$p_S \approx 2.9 \times 10^{-19} n^{1/2} T_e^{11/4} B^{5/2} (1 - R)/a^{1/2}, \quad \text{(W/m}^3\text{)} \qquad \text{(II.9)}$$

where B is in T, R is the reflection coefficient of the reactor wall, and a is a characteristic plasma absorption length, taken here to be approximately the plasma radius. Rosenbluth (1970) has derived a more accurate expression for the case of a toroidal plasma with weakly relativistic electrons ($T_e \lesssim 10$ keV). Recent numerical calculations (Yang,

1973) have generalized Rosenbluth's result to the electron temperature range above 10 keV.

An important means of increasing the energy of a plasma is adiabatic (isentropic) compression. Assuming the plasma to be a perfect gas characterized by a specific heat ratio γ, the density and temperature respond to a rate of increase of magnetic field $\dot{B}$ as follows: $\dot{n}/n = (2/\gamma)\dot{B}/B$; $\dot{T}/T = [2(\gamma - 1)/\gamma]\dot{B}/B$. The rate of increase of plasma internal energy density $w = 2nT/(\gamma - 1)$ is given by $\dot{w}/w = 2\dot{B}/B$. Assuming (II.1) for β, we find

$$\dot{w} = \beta\dot{B}B/(\gamma - 1)\mu_0. \tag{II.10}$$

A heating means particularly appropriate to tokamaks is "Ohmic" heating produced by the current flowing along the plasma. The heating power density p_Ω is ideally the product of the square of the current density j and the classical resistivity η due to electron–ion collisions (Spitzer, 1962, p. 136). Thus

$$p_\Omega = 0.5j^2\chi_\Omega \ln\Lambda/T_e^{3/2}, \qquad (\mathrm{W/m^3}), \tag{II.11}$$

where we have included a dimensionless factor χ_Ω to account for "nonclassical" plasma collective effects which raise η above its collisional value.

It will sometimes be convenient to define the density of power deposition in a plasma by beams of neutral atoms, each of energy E_0:

$$p_{\mathrm{inj}} = SE_0, \tag{II.12}$$

where S is the atom injection rate per unit volume.

Finally, an important loss of plasma energy is that given by the heat flow to the reactor wall. In a strong uniform longitudinal magnetic field B the ion and electron heat flow vectors $\mathbf{Q}$ (whose units are w/m^2) have the form

$$\mathbf{Q}_{e,i} = -\tfrac{3}{2}T_{e,i}D_{\mathrm{cl}}\nabla n - \kappa\nabla T. \tag{II.13}$$

The "classical" particle diffusion coefficient D_{cl} describes the diffusion of electrons and ions together across the magnetic field and is characterized by the electron–ion collision rate ν_{ei} and the electron gyroradius ρ_e:

$$D_{\mathrm{cl}} = \rho_e^2\nu_{ei}. \tag{II.14}$$

Using Spitzer's value (Spitzer, 1962, p. 136) of ν_{ei} in a strong magnetic field, we have

$$D_{\mathrm{cl}} = 0.84 \times 10^{-22}(nZ \ln\Lambda/B^2T^{1/2}) \qquad (\mathrm{m^2/sec}). \tag{II.15}$$

The classical thermal conduction coefficient κ describes heat flow characterized by the ion–ion collision rate ν_{ii} and the ion gyroradius ρ_i:

$$\kappa_{\mathrm{cl}} = n\rho_i^2\nu_{ii}. \tag{II.16}$$

For a plasma cylinder of radius a the power loss per unit length is

$$P_Q = 2\pi a[Q_i(a) + Q_e(a)], \tag{II.17}$$

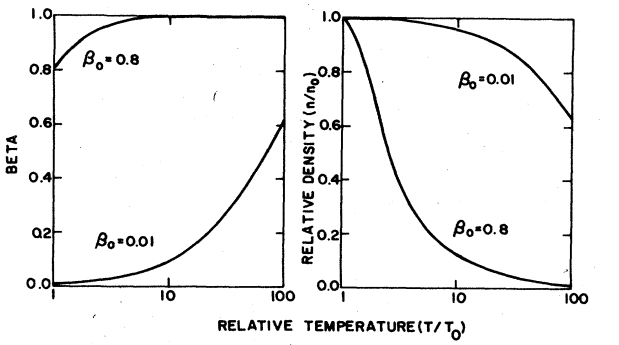

FIG. 4. Effects of plasma heating at constant total particle number and magnetic field for low- and high-β plasmas.

where $Q_{e,i}$ are the radial components of $\mathbf{Q}_{e,i}$. It will sometimes be convenient to characterize the heat flow by an energy-loss e-folding time τ_E:

$$P_Q = \tfrac{3}{2}\pi a^2 n(T_e + T_i)/\tau_E. \tag{II.18}$$

In this discussion of τ_E we have assumed ideal conditions where only ion–ion and ion–electron collisions contribute to the heat loss. It is observed in tokamaks that neutral particles in the plasma cause particle and energy losses by charge exchange making an additional contribution to P_Q and τ_E^{-1}.

D. Heating of low- and high-beta plasmas

It is instructive to consider the manner in which the quantity beta changes during the heating of a plasma having a fixed number of particles, confined by a constant magnetic field. In the case of a low initial β value ($\beta_0 = 0.01$, Fig. 4) e.g., in a tokamak, as the temperature increases the value of beta also increases, while the particle number density remains nearly constant, since the plasma volume is nearly constant. Since the gross stability of a tokamak is a sensitive function of β, heating may drive it unstable ($\beta \gtrsim 0.1$) unless energy is drained from the plasma. For a high initial beta value ($\beta_0 = 0.8$, Fig. 4), e.g., in a theta pinch, beta does not change appreciably, while the density decreases, owing to the volume change as the plasma expands. Such a plasma performs work against the confining magnetic field, an important effect in the theta-pinch reactor power balance (cf., Sec. V.D.2).

As an example of plasma power balance in a low-beta reactor (where β is assumed constant) consider the tokamak case illustrated in Fig. 5 (Sweetman, 1973). The Ohmic heating rapidly declines with rising temperature and becomes ineffective in the thermonuclear range of a few kiloelectron volts. The α-particle heating, on the other hand, rises rapidly in this temperature region. At the highest temperatures achieved by Ohmic heating, the sum of Ohmic and α-particle heating is not sufficient to overcome the losses due to ion heat conduction and bremsstrahlung. (Compare the minimum of the curve at $T \approx 2$ keV with the corresponding ordinate of the dashed line.) Therefore the plasma cannot enter the "ignited" regime $T \gtrsim 5$ keV, where α-particle heating alone exceeds the losses and the plasma would become thermally self-sustaining. This is the intersection of the α-heating and total-heat-loss curves. In

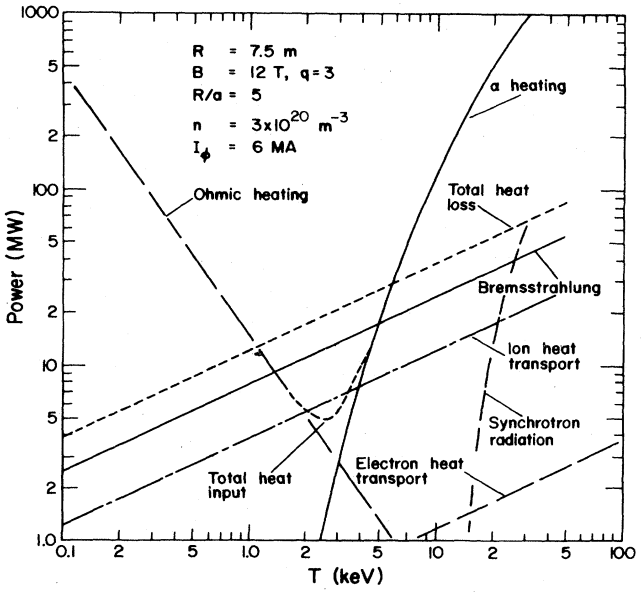

FIG. 5. Plasma power balance for a low-β (tokamak) reactor. For definitions of the quantities in the legend see Sec. IV.A.

order to achieve ignition in this example an additional heat source of ~20 MW is necessary to bridge the gap between the minimum of the total heat-input curve and the rising curve of total heat loss. At this writing the most promising means of supplying this loss is by neutral-beam injection.

An example of ignition by adiabatic compression in a theta-pinch reactor (Sec. V.D.1) is shown in Fig. 6. Application of a shock-heating magnetic field of $1.3T$ produces a plasma temperature of 1.1 keV which is below that of the ignition condition $p_\alpha = p_{\rm br}$ at $T \approx 4$ keV. As the magnetic field rises to $11T$ and the temperature rises to ~3 keV, the rate of adiabatic-compression work input [$= \dot{w}$, Eq. (II.10)] to the plasma rises to a maximum of 100 MW/m, followed by a decrease (in this example) to a value of 50 MW/m, after which the α particles sustain the ignited plasma.

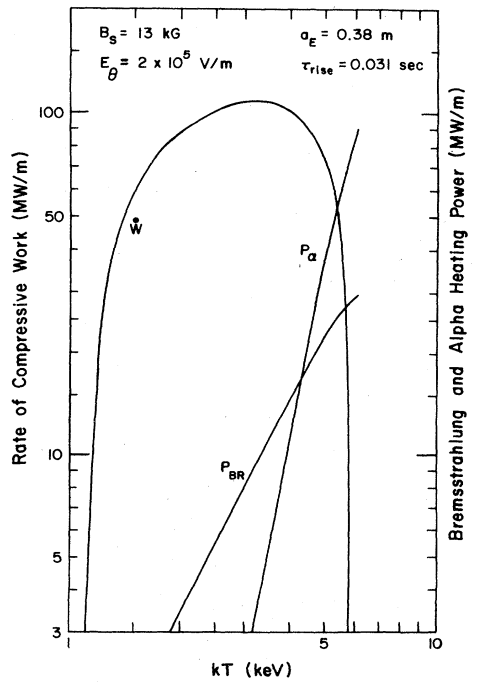

FIG. 6. Ignition trajectory of a theta-pinch reactor by means of adiabatic compression. Power quantities are stated per meter length of the plasma column assuming no thermal conduction losses.

III. POWER BALANCE, REACTOR STABILITY AND FUEL BURNUP

A. Plasma power balance

We now examine the time dependence (Ohta, Yamoto and Mori, 1971) of the plasma temperature under the influence of the power input and loss quantities discussed in Sec. II. Neglecting synchrotron radiation, plasma energy conservation requires[1]

$$3ndT/dt - 2T\,dn/dt = p_\alpha - p_{\rm br} - p_Q + p_{\rm inj}, \qquad \text{(III.1)}$$

Here the second term represents expansion work done by the plasma. We characterize the thermal conduction power p_Q by a characteristic energy-loss e-folding time τ_E [Eq. (II.18)], and the injected power, Eq. (II.12), by an injection rate S of particles of energy E_0. As a simple example, we consider a low-β reactor with constant plasma volume and density and negligible particle loss. Using (II.6) and (II.7),

$$dT/dt = nf(T) - T/\tau_E + \tfrac{1}{3}SE_0/n \qquad (\text{low } \beta), \qquad \text{(III.2)}$$

where

$$f(T) = f_\alpha(T) - f_{\rm br}(T) = \tfrac{1}{12}\langle\sigma v\rangle E_\alpha - 0.5 \times 10^{-38}T^{1/2}, \qquad \text{(III.3)}$$

and we have taken $T_e = T_i = T$ and $Z = 1$.

In the case of high-β ($\beta \approx 1$) reactor with negligible particle loss, the plasma pressure is constant if the magnetic field is constant, and we have $d(nT)/dt = 0$. In this case, $-2T\,dn/dt = 2ndT/dt$, and (III.1) reduces to

$$dT/dt = \tfrac{2}{5}nf(T) - 3T/5\tau_E + \tfrac{1}{5}SE_0/n. \qquad (\text{high } \beta) \qquad \text{(III.4)}$$

The condition for thermal equilibrium of the reactor plasma occurs when $dT/dt = 0$. Denoting equilibrium values by the subscript zero, we find in the absence of injection:

$$n_0\tau_E = T_0/f(T_0). \qquad \text{(III.5)}$$

Thus at thermal equilibrium the product of density and

[1] In this simple, idealized example we have assumed that the radiation losses are entirely accounted for by bremsstrahlung with $Z = 1$. In present tokamak experiments, impurity ions are present in appreciable quantities, leading to effective values of Z of approximately 2 to 3 in Eq. (II.7). Additional energy losses from line and recombination radiation also arise. In this and the tokamak discussion of Sec. IV we neglect impurity radiation and the charge-exchange losses mentioned in Sec. II.C.

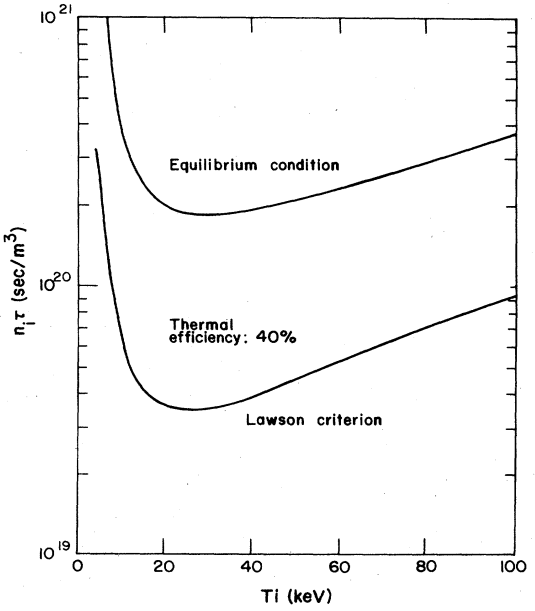

FIG. 7. The Lawson condition and the equilibrium condition Eq. (III.5) as functions of plasma temperature for D–T plasmas (Mills, 1970).

energy confinement time is a function of temperature alone. The equilibrium $n_0\tau_E(T_0)$ is shown on the upper curve in Fig. 7.

B. Thermal stability

The equilibrium described by Eq. (III.5) and Fig. 7 is dominated by the shape of the $f(T)$ function which is essentially that of the D–T reaction rate parameter $\langle\sigma v\rangle$ of Fig. 3. Once ignition is achieved, α-particle heating far outweighs bremsstrahlung loss from the D–T plasma, and the plasma can make an unstable temperature excursion. If the excursion is toward larger temperatures, and bremsstrahlung is the only loss, stability will occur in the neighborhood of the maximum of the $\langle\sigma v\rangle$ curve of Fig. 3, where the derivative $f'(T) = 0$. Otherwise the plasma must be stabilized by external means whereby a servo loop or negative "feedback" system produces changes in some parameters, such as the relative D and T fuel mixture or fuel-injection power, in response to sensed first-order changes Δ from the equilibrium value of the temperature.

To estimate a growth rate γ_T for exponentiation of the thermal instability, we consider a low-β system with constant n, τ_E, and S. Setting $T = T_0 + \Delta$ in Eq. (III.2), and using the zero-order equilibrium relation (III.5), we find in first order:

$$d\Delta/dt = n_0 f_0' \Delta, \tag{III.6}$$

whose solution is

$$\Delta = \Delta_0 \exp\gamma_T t. \tag{III.7}$$

The growth rate is

$$\gamma_T = n_0 f'. \tag{III.8}$$

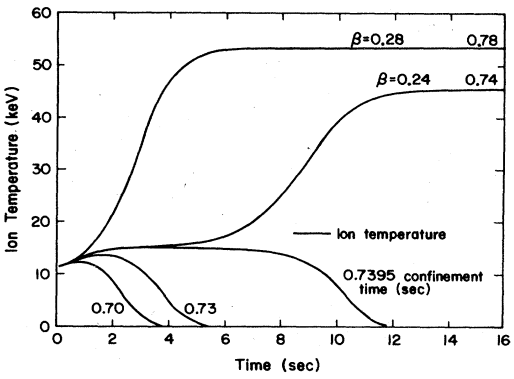

FIG. 8. Illustrating the effects of confinement time on the unstable thermal excursions of a low-β reactor plasma (Mills, 1970). The equilibrium corresponds to the operating point at time zero at $T_0 = \sim 10$ keV, with $\beta_0 \approx 0.10$.

For the high-β, constant-pressure case with plasma expansion γ_T is smaller by a factor of 3/5.

Mills (1970) has calculated the unstable excursions of a D–T plasma about an operating point at $T_0 = 10$ keV, $\beta_0 = 0.10$, with $\tau_{E0} = 0.74$ sec (Fig. 8), taking separate account of the electrons and ions. He made use of power balance quantities corresponding to Eqs. (II.6) through (II.9) with injected particle energy $E_0 = 0$, and treated the thermalization of the α particles by means of a simplified kinetic model. The upper curves of Fig. 8 show that when τ_E becomes too long, an unstable excursion is made to temperatures in the neighborhood of 50 keV, and β values near 0.25. At lower τ_E values, the temperature decays, and the reactor "goes out." A significant consequence of operating at a stable high-temperature point, as opposed to an unstable low-temperature point, is that considerably more confining magnetic field is required in the former case. In a conceptual tokamak design, Badger *et al.* (1973) (Sec. IV, below) estimate plasma parameters for stable and unstable cases. In the stable case, T_i is much higher, and for a given beta, the required magnetic field is also higher. The added cost of the toroidal-field magnet (55%) must then be compared with the cost of feedback control to maintain the lower-temperature, unstable equilibrium at lower magnet cost.

C. Reactor power (energy) balance

Figure 9 is a power (energy) flow diagram of a fusion reactor. A quantity basic to the operation of a fusion reactor is the ratio Q of the thermonuclear power output P_T from the plasma core which goes to the thermal conversion equip-

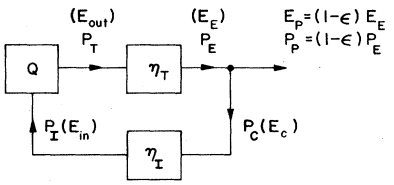

FIG. 9. Simplified power-flow diagram of a fusion reaction. The power P refers to the magnetic-confinement case, and the energies E in parentheses to the laser-fusion case.

ment, to the injected power P_I necessary to sustain the plasma in a thermonuclear state:

$$Q = P_T/P_I. \tag{III.9}$$

The electrical power output of the thermal converter is

$$P_E = \eta_T P_T, \tag{III.10}$$

where η_T, related to the Carnot efficiency, is the efficiency at which heat is converted to output electrical power P_E in the thermal converter (e.g., turbogenerators). Its values range from 0.35 to at most about 0.6, depending on the temperature of the working fluid. In order to provide the injection energy at some efficiency η_I, a fraction ϵ of the plant electrical output P_E must be "recirculated." The circulating power fraction

$$\epsilon = P_C/P_E = 1/\eta_T\eta_I Q \tag{III.11}$$

is important as a cost determining factor, since it adds to the required capacity of the thermal conversion equipment. The fusion plant output power

$$P_P = (1 - \epsilon)P_E = \eta_P P_T \tag{III.12}$$

is related to the thermal power P_T of the reactor core by the plant efficiency

$$\eta_P = (1 - \epsilon)\eta_T. \tag{III.13}$$

Detailed definitions of fusion-reactor power-balance quantities have been provided by Persiani, Lipinski, and Hatch (1972). A systematic comparison of the four types of fusion reactors in terms of their energy-balance requirements has been made by Nozawa and Steiner (1974).

D. The Lawson or "breakeven" criterion

Leaving aside all elements of a fusion power plant except the plasma and a thermal conversion system, we can calculate the plasma conditions necessary for energy breakeven, referred to unit volume of plasma. This is the condition of 100% circulating power and no net plant output p_P, where the electrical output of the thermal converter ideally sustains the plasma energy content $3nT$ with only bremsstrahlung losses. The thermal energy available in one confinement time τ_c is thus

$$p_T\tau_c = 3nT + 1/4n^2\langle\sigma v\rangle Q_T\tau_c + p_{\rm br}\tau_c, \tag{III.14}$$

where $Q_T = ME_n + E_\alpha$ (cf. Sec. I.B) is the total energy release from a fusion reaction, including the neutron-induced blanket reactions. The minimum recirculated (injected) energy necessary to provide the plasma energy plus bremsstrahlung loss is

$$\eta_I p_C\tau_c = p_I\tau_c = 3nT + p_{\rm br}\tau_c. \tag{III.15}$$

The breakeven condition $p_C = p_E = \eta_T p_T$ is therefore

$$\eta_I\eta_T(3nT + 1/4n^2\langle\sigma v\rangle Q_T\tau_c + p_{\rm br}\tau_c) = 3nT + p_{\rm br}\tau_c. \tag{III.16}$$

Solving gives

$$n\tau_c = \frac{(1 - \eta_T\eta_I)T}{\eta_I\eta_T(Q_T/E_\alpha)f_\alpha(T) - (1 - \eta_T\eta_I)f_{\rm br}(T)}, \tag{III.17}$$

where $f_\alpha(T)$ and $f_{\rm br}(T)$ are given by Eq. (III.3). The quantity E_α is the α-particle energy given in Table I. This is the well-known Lawson criterion (1957) whose functional form is somewhat similar to that of the equilibrium condition (III.5) as can be seen from Fig. 7, where $n\tau_c$ is plotted versus T for $\eta_I = 1$. However, the two conditions represent quite different physical situations. In Fig. 7 the region above the lower curve represents excess plasma energy production over plasma energy input.

The Lawson criterion at temperatures somewhat above D–T ignition ($T \approx 5$ keV) is commonly taken as a measure of the achievement of "scientific feasibility" whereby plasma experiments reach that degree of heating and confinement that would justify proceeding to fusion reactors. This condition is that $n\tau_c \gtrsim 10^{20}$ sec/m^3. We may also take as a scientific-feasibility criterion the achievement of an e-folding growth of the temperature in an ignited D–T plasma having a thermal growth rate γ_T. In order to compare these conditions we set $\tau_c = \gamma_T^{-1}$ in (III.17), and substitute (III.8). Neglecting $f_{\rm br}$ in (III.17), we find the required temperature from the condition

$$\frac{Tf'}{f} = \frac{d\ln\langle\sigma v\rangle}{d\ln T} = \frac{\eta_I\eta_T Q_T}{(1 - \eta_I\eta_T)E_\alpha} \approx 4. \tag{III.18}$$

To evaluate the right-hand side of (III.18), we have taken $\eta_T = 0.4$, $\eta_I = 1$, and $Q_T = 22$ MeV. Referring to Fig. 3, we find that this condition is met at $T \approx 5$ keV. Thus the Lawson criterion and the ignition criterion are approximately equivalent for a D–T plasma.

E. Plasma burnup and reaction time

Consider a plasma whose D and T ions have total number density n before any fusion reactions have taken place. As the reaction progresses, the number density $n_i = n_{\rm D} + n_{\rm T}$ of reacting D and T ions is decreased by the number n_p of product particles (neutrons plus α particles) which are produced per unit volume. We define the burnup fraction

$$f_B = n_p/n = 1 - n_i/n \tag{III.19}$$

which measures the depletion of D and T ions. Since $n = n_i + n_p$ is constant, the rate of change of ion density is given by

$$\dot{n}_i = -\dot{f}_B n. \tag{III.20}$$

For an equal mixture of D and T ions the reaction rate per unit volume is given by

$$R_i = n_{\rm D}n_{\rm T}\langle\sigma v\rangle = 1/4n_i^2\langle\sigma v\rangle, \tag{III.21}$$

where $\langle\sigma v\rangle$ is the D–T reaction rate parameter of Sec. II.B and Fig. 3. Since $R_i = -\dot{n}_{\rm D} = -\dot{n}_{\rm T} = -1/2\dot{n}_i$, we have

$$-\dot{n}_i = 1/2n_i^2\langle\sigma v\rangle. \tag{III.22}$$

Substituting (III.19) and (III.20), gives (Chu, 1972)

$$\dot{f}_B = 1/2(1 - f_B)^2 n\langle\sigma v\rangle. \tag{III.23}$$

Defining the reaction time $\tau_r = 1/n\langle\sigma v\rangle$, we have

$$\dot{f}_B = (1/2\tau_r)(1 - f_B)^2. \tag{III.24}$$

Assuming constant τ_r (constant $\langle\sigma v\rangle$), the solution of (III.24) for which $f_B(t = 0) = 0$ is

$$f_B(t) = \frac{t/2\tau_r}{1 + t/2\tau_r}. \tag{III.25}$$

For small t, $f_B = t/2\tau_r = (1/2)nt\langle\sigma v\rangle$. If we consider typical burn conditions of $T = 10$ keV, for which $\langle\sigma v\rangle = 10^{-22}$ m^3/sec, then the Lawson condition $nt = 6 \times 10^{19}$ sec/m^3 (Fig. 7) corresponds to a burnup fraction of 0.3%.

IV. TOKAMAK REACTORS

A. Principles of operation

The essential features of a tokamak diffuse toroidal pinch are shown in Fig. 10. The plasma of major radius R and minor radius a forms the secondary of a set of transformer cores whose primaries are driven by a pulse of current which induces an axial (or toroidal) current I_ϕ and current density j_ϕ in the plasma. This current serves two purposes: (a) it heats the plasma by Ohmic processes [Eq. (II.11)] such that nj_ϕ^2 is the heating power density (η is the plasma resistivity); (b) the poloidal field B_θ which encircles the plasma ring contains the plasma pressure p according to the relation

$$p = \beta_\theta B_\theta^2/2\mu_0 = \mu_0\beta_\theta I_\phi^2/8\pi^2a^2. \tag{IV.1}$$

The quantity β_θ (the poloidal beta) is limited theoretically (Mukhovatov and Shafranov, 1971) to a value equal to the aspect ratio $A = R/a$ and has a value of about 0.5 in present experiments.

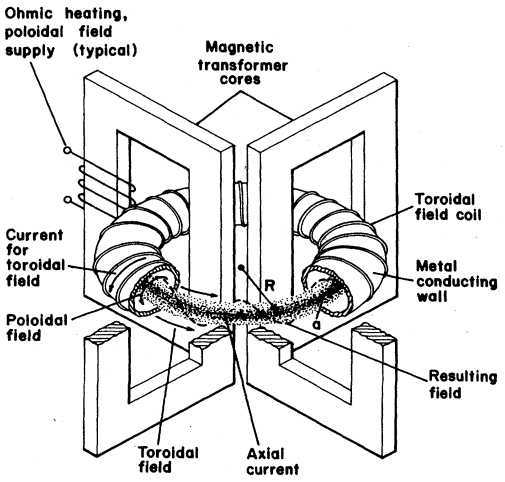

FIG. 10. Illustrating the main features of a tokamak.

Because of its dual function, the pulsed power supply which drives the primary windings is called the Ohmic-heating or poloidal-field supply. It is generally recognized that the Ohmic heating can produce plasma ion temperatures no greater than about 3 keV in large tokamaks, whereas temperatures greater than 6 keV are required for ignition or breakeven and about 10 keV for reactor operation. Thus supplemental heating is required. A method generally accepted as quite promising is to inject beams of energetic neutral D–T ions into the plasma.

A plasma subject only to a poloidal field is unstable to gross fluid motions driven by accidental inhomogeneities in the magnetic field or by plasma fluctuations. In order to avoid these magnetohydrodynamic (MHD) modes, an additional toroidal field B_ϕ parallel to the plasma ring is added so that the field lines resulting from B_ϕ and B_θ are helical, surrounding the plasma as shown in Fig. 10. The ratio of the pitch length of these helical lines to the circumference $2\pi R$ of the plasma is the so-called stability margin

$$q = \frac{a}{R}\frac{B_\phi}{B_\theta} = \frac{B_\phi}{AB_\theta}. \tag{IV.2}$$

For helical magnetic lines, the MHD modes are helical displacements following the pitch of the lines. When $q > 1$, the plasma cannot be unstable to a mode which displaces it into a helix of circular cross section, since the motion cannot be accommodated in the circumference. For $q > 2$, an elliptical distortion of the plasma which follows the helicity of the lines cannot be accommodated; and so on for trefoil distortions, etc., which are stable for $q > 3$, etc. In present experiments, q is chosen to be $\gtrsim 3$ at the plasma edge, and $\gtrsim 1$ near the center.

In controlled fusion research, the quantity β most often referred to, and the parameter whose square is a factor in the thermonuclear power, is the toroidal beta [compare β without subscript of Eq. (II.1)]:

$$\beta_\phi = \frac{p}{B_\phi^2/2\mu_0} = \frac{\beta_\theta}{(qA)^2}. \tag{IV.3}$$

In present practice for plasmas with circular cross sections, since β_θ is about 0.5, and qA is commonly greater than 10, the values of β_ϕ in tokamaks are about 0.5% or less.

Another feature of tokamaks in most present practice is a thick metal conducting wall whose main function is to produce an equilibrium of the plasma ring. This occurs because the toroidal current I_ϕ of the plasma produces an image current in the metal shell when the plasma moves off the circular axis of the shell. The effect of this image current is to produce a magnetic field $B_\perp$ perpendicular to the plane of the torus. The body force $I_\phi B_\perp$ acts inward on the plasma ring to hold it in place against the outward force which arises from the imbalance of magnetic pressures $B_\phi^2/2\mu_0$ on the outside (weaker B_ϕ) and the inside (stronger B_ϕ) of the ring; i.e., there is a gradient ∇B_ϕ of toroidal field toward the major axis of the torus. In practice there is also a toroidal liner which can be evacuated, placed inside the conducting wall, and the plasma is kept from touching the liner by means of "limiters," which are annular diaphragms inside the liner. In practice the minor radius a is the inner radius

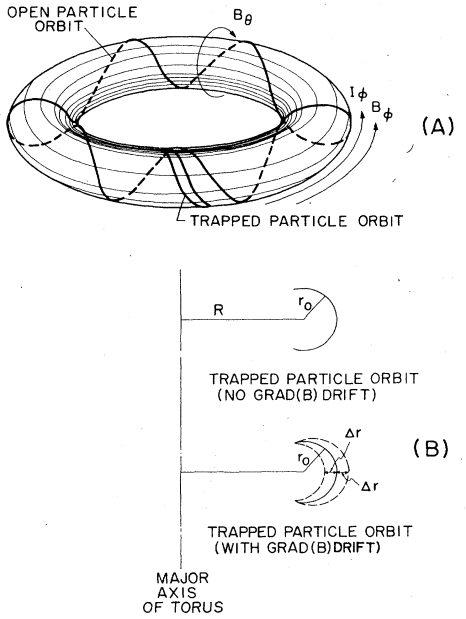

FIG. 11. Illustrating charged-particle orbits in a tokamak device.

of the limiter. A thick metal wall would not be practical in a fusion reactor because of its neutron absorption and the difficulty of heat removal. Experiments have shown that it can be eliminated and that stable plasma behavior occurs when only $B_\perp$ is applied without a conducting shell to produce the equilibrium.

B. Toroidal effects on heat and particle flow

In a tokamak the particle-diffusion and heat-conduction coefficients, described by Eqs. (II.14) and (II.16) for uniform axial magnetic fields are modified by the effects of the toroidal geometry on the ion and electron orbits. This effect is illustrated in Fig. 11 which shows orbits in the combined toroidal and poloidal fields. Since the field is stronger on the inside of the torus there is a certain fraction of particles in trapped "banana" orbits, where the particle motion along a helical line is stopped by the mirroring effect (see Sec. IV.B below) of the higher field as it moves toward the inside of the torus at each end of the closed orbit (upper portion of Fig. 11). The lower portion of Fig. 11 is a projection of a particle orbit on a (r, θ) plane, where the radial half-width of the orbit at the toroidal midplane is Δr. It can be shown (Rosenbluth, Hazeltine and Hinton, 1972) that the fraction of particles on trapped orbits is $A^{-1/2}$. The orbit width Δr determines the collisional step size in the diffusion and thermal conduction coefficients and is given approximately by

$$\Delta r \approx \rho_\theta / A^{1/2} = A^{1/2} q \rho_\phi. \tag{IV.4}$$

Thus the step size is characterized by the gyroradius ρ_θ in the weaker poloidal field, rather than in the longitudinal (toroidal) field as in Eqs. (II.14) and (II.16). [From (IV.2) we see that the poloidal gyroradius is larger than the toroidal gyroradius ρ_ϕ by a factor Aq.] Another banana-orbit effect is that the collision frequency is greater by the factor A than the value ν_{ei} in the uniform-field case, since smaller angular deflections are required to effect the Δr step than are required for a 90° deflection in the uniform-field case, as is assumed Eqs. (II.14) and (II.15). The net effect of the three factors $A^{-1/2}$, $(A^{1/2}q)^2$, and A is that the particle diffusion coefficient of (II.15) is modified by the factor $A^{3/2}q^2$. The new diffusion coefficient is denoted by the name "neoclassical" and is given by

$$D_{\rm nc} \approx q^2 A^{3/2} D_{\rm cl}. \tag{IV.5}$$

Since in a reactor q is about 3, and A also about 3, the neoclassical coefficient is more than an order of magnitude greater than the classical coefficient. A more exact expression for the case where ν_{ei} is less than the banana-orbit circulation or "bounce" time is

$$D_{\rm nc} = 1.12[1 + (T_i/T_e)] q^2 A^{3/2} \nu_{ei} \rho_{e\phi}^2 \qquad (m^2/\text{sec}). \tag{IV.6}$$

Similarly the classical ion thermal conductivity is modified by banana effects on the ion orbits and collision times, with the result that

$$\kappa_{\rm nc}{}^i = 0.68 \times 10^{-4} \rho_{i\theta}^2 \nu_{ii} / A^{1/2} \qquad (\text{m}^2/\text{sec}). \tag{IV.7}$$

For a tokamak with nearly uniform temperature, the $\kappa_{\rm nc}{}^i$ effects can be neglected. This may be the case if the separatrix of a divertor (cf., Sec. IV.C) keeps the plasma boundary away from the wall, effectively insulating it and imposing the boundary condition $dT/dr = 0$. Then the temperature distribution across the plasma is nearly flat and heat and particle flows are characterized by the particle (energy) confinement time [cf. Eq. (II.18)]

$$\tau_E \approx \tau_{\rm nc} = a^2 / D_{\rm nc}. \tag{IV.8}$$

For typical reactor parameters: $T_i \approx T_e = 10^4$ eV, $n = 10^{20}$ m^{-3}, $B_\phi = 4T$, $a = 5m$, $q \approx 2$, $A \approx 3$, $\ln\Lambda \approx 15$, we find $D_{\rm nc} \approx 45\, D_{\rm cl}$ and $\tau_{\rm nc} \approx 3 \times 10^5$ sec. Thus the value of $n\tau_{\rm nc} \approx 3 \times 10^{25}$ sec/m^3 would far exceed the $n\tau$ value (10^{20}–10^{21} sec/m^3) of Fig. 7 required for thermal equilibrium

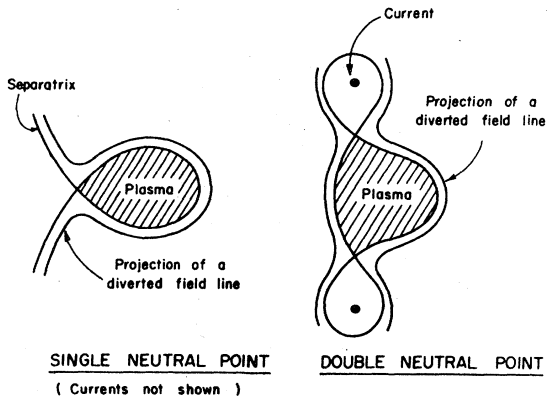

FIG. 12. Magnetic-field configurations of poloidal field divertors (Badger *et al.*, 1973).

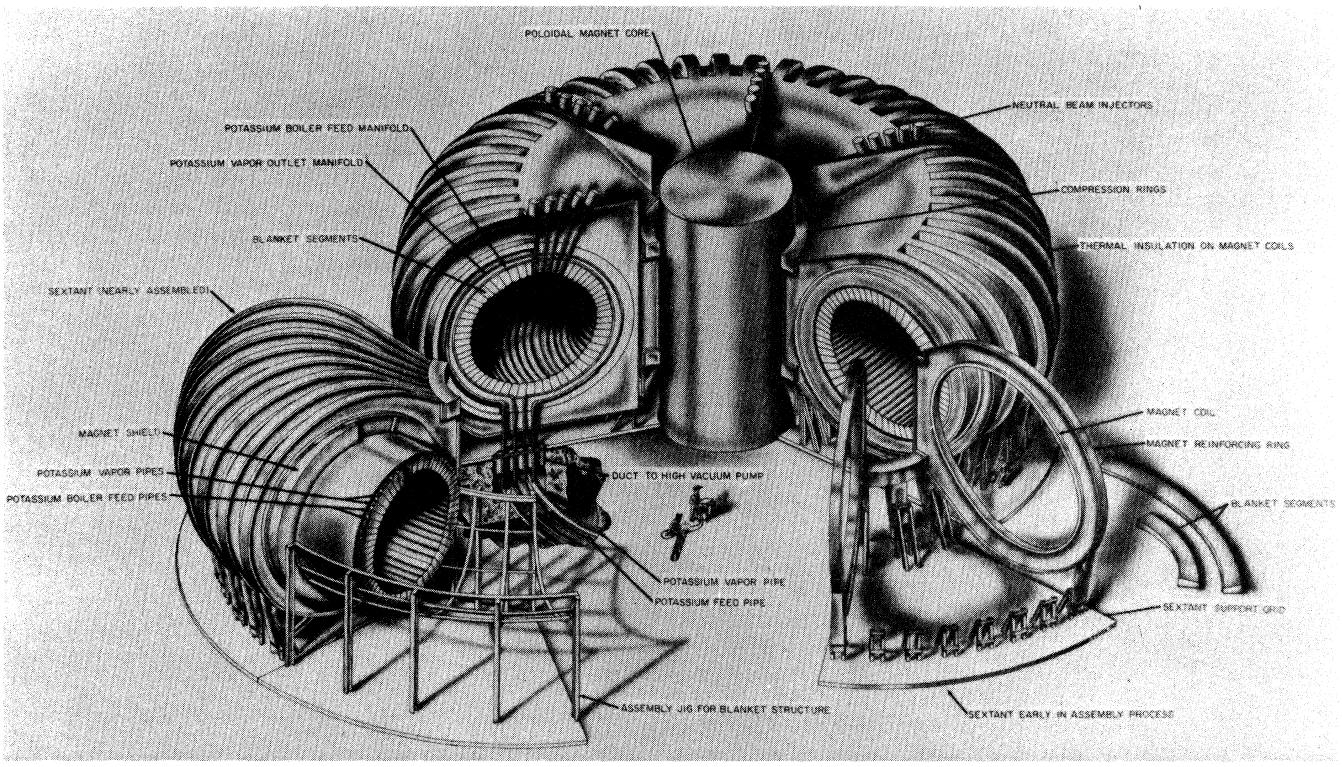

FIG. 13. General view of the ORNL conceptual tokamak fusion reactor.

To achieve lower $n\tau_c$ values, high-Z (Argon) impurity is deliberately introduced in two of the conceptual reactor plasmas to be discussed below in order to increase the bremsstrahlung loss by a factor ~ 10 [Eq. (II.7)], and the diffusion coefficient (IV.6) is imagined to be enhanced by a factor of thousands. The latter enhancement may occur unavoidably because of microinstabilities which produce turbulent fluctuating electric fields that greatly increase the diffusion coefficients over their classical, collisional values.

C. Divertors

The basic object of a divertor is to prevent particles diffusing out of the plasma from hitting the first wall and to provide a means of removing α-particle "ash" and impurities, while maintaining a steady through-put of fuel from injectors. The divertor also provides a shield for the hot plasma against impurities released from the wall, or flowing back from the divertor chamber.

The magnetic divertors considered here are based on the idea of generating a null in the poloidal (r, θ) field as shown in Fig. 12. This generates a separatrix outside of which field lines are carried away from the plasma as they pass the neutral points shown in Fig. 12 at the crossings of the zero-field lines (separatrices). Inside a separatrix the magnetic flux surfaces remain closed, and the separatrix, rather than a material wall is the effective boundary of the plasma. Plasma particles diffuse across the separatrix and then follow the open field lines to particle collectors. The tokamak design of the Princeton group (Fig. 16) uses the single neutral-point divertor, while that of the University of Wisconsin group (Fig. 17) uses the double neutral-point divertor.

D. Conceptual tokamak reactor designs

In this review we consider three conceptual designs: (1) that of the Oak Ridge National Laboratory (ORNL) (Etzweiler, *et al.*, 1973, Fraas, 1973a, 1973b), (2) the UWMAK conceptual reactor of the University of Wisconsin (Badger *et al.*, 1973; Kulcinski and Conn, 1973), and (3) the design of the Princeton Plasma Physics Laboratory (PPPL) (Mills, 1974a, 1974b; Tenney, 1974; Gralnick, 1973). A good earlier reference on tokamak reactors is Golovin, *et al.*, (1970). The ORNL design (Fig. 13) represents a composite of the plasma and burn cycle of Etzweiler, *et al.*, (1973), adapted by the author to the core and power-conversion system of Fraas (1973a, 1973b). It has no divertor and uses a power cycle in which joule-heating and neutral-beam injection produce ignition and peak power density. The plasma power density then subsides to a lower level which is sustained by the injectors. The UWMAK design (Fig. 14) operates in the unstable steady state, but in pulses whose length is determined by the decay of the poloidal field and the necessity to dispose of impurities not removed by the divertor. It has a double-null divertor and uses joule-heating and neutral-beam injection, followed by D–T pellet injection. The PPPL design (Fig. 15) is conceived as a long-pulse, essentially steady-state system, fueled by D–T pellets.

Table II gives a comparison of the plasma and magnetic field parameters for the three conceptual reactors. In respect to poloidal beta the ORNL device operates near the theoretical mean limit A (Mukhovatov and Shafranov, 1971), while the UWMAK and PPPL values lie closer to present practice (~ 0.5) and correspond to a value between

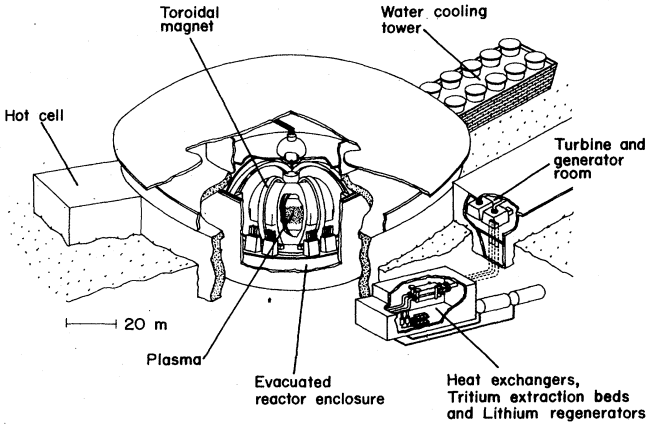

FIG. 14. General view of the UWMAK conceptual tokamak fusion power plant.

the equilibrium-limiting value A and the value $A^{1/2}$ on axis for which diffusion would drive a maximum allowable self-sustaining current I_ϕ [the "bootstrap" current (Galeev and Sagdeev, 1970)] in the absence of a toroidal electric field. Note the large values of toroidal current (15–20 MW) and toroidal magnetic energy (100–300 GJ). In the UWMAK case the poloidal energy of 58 GJ would require a local inertial or superconducting magnetic-energy store (somewhat similar to that of a theta-pinch reactor) if the risetime of B_θ were of the order of 10 secs or less, while for times greater than 100 sec the power to build up the poloidal energy [$\lesssim$500 MW(e)] could be taken "off the line."

Figure 16 shows a section of the PPPL blanket divertor and a toroidal magnet coil (one of 48), while Fig. 17 is one of the 12 blanket-magnet modules of the UWMAK reactor. The double-null design of the latter allows the smaller aspect ratio indicated in Table II. The superconducting UWMAK magnets (poloidal and toroidal) are Cu-stabilized Nb Ti (4 K), while the PPPL design uses Nb_3Sn ($\sim$12 K).

Table III gives a comparison of the first-wall neutron-blanket and fueling characteristics of the three conceptual reactors. The ORNL blanket operates at high temperature (1000 C), corresponding to the use of Nb—1% Zr structural material. The PPPL and UWMAK designs utilize stainless steel and PE 16 Austinitic material and correspondingly lower operating temperatures (680 C and 500 C, respectively). In the ORNL and UWMAK designs, lithium is used both as the neutron moderator and coolant, while the PPPL design uses a nonconducting salt, eutectic FLIBE [$(LiF)_2BeF_2$] moderator with helium coolant, thereby avoiding problems associated with the flow of conducting lithium across magnetic fields and simplifying tritium recovery. The ORNL blanket (Fraas, 1973a) utilizes segments (Fig. 13) with longitudinal lithium flow (parallel to B_ϕ) except at turning sections where radial currents pump the lithium electromagnetically and reverse its flow direction. Outside the blanket regions are radiation shields which reduce the total heat load on the superconducting magnets to very small levels (1.5 to 15 kW).

The wall loading of the ORNL design IIA, at the lower extreme in Table III is chosen sufficiently small so that the first wall and blanket structure can survive neutron radiation damage for relatively long times (6–10 years). In the UWMAK design, first-wall changeout is expected every two years because of radiation damage, the critical consideration being embrittlement of the stainless steel. The tritium breeding ratios are quite adequate, resulting in short ($\sim$100-day) doubling times which can be lengthened by deliberately spoiling the breeding. The lithium inventories are of the order of 10^6 kG, and tritium inventories are of the order of 10 kG, corresponding to T_2 concentrations of $\sim$5 parts per million. This small concentration is necessary to keep the radioactive tritium loss from the plants within acceptable bounds. Note the small tritium consumption.

TABLE II. Plasma and magnetic field parameters of the three conceptual tokamak reactors.

	ORNL	PPPL	UWMAK
Plasma:			
Poloidal beta β_θ (Av.)	3.0	1.8	1.08
Toroidal beta β_ϕ	0.15	0.13	0.052
Major Radius R (m)	10.5	10.5	13
Minor Radius a (m)	3.3	3.25	5
Aspect Ratio A	3.2	3.2	2.6
Safety factor q	1.4	2.1	1.75
Magnetic fields:			
Av, Tor, B_ϕ (kG)	60	60	38
Max, Tor, B_ϕ (kG)	147	160	87
Pol. field B_θ (a) (kG)	13	9	8.4
Plasma current MA	21	15	21
Tor. mag. en. (GJ)	120	223	240
Pol. mag. en. (GJ)	$\sim$10	$\sim$8	58

The power-balance quantities of the three conceptual power plants are given in Table IV. The ORNL reactor IIA is characterized by low thermal and electrical powers, corresponding to its small wall loading and low plasma density. However it has a large thermal conversion efficiency, corresponding to its refractory metal structure and a correspondingly high operating temperature. The thermal conversion plant (Fraas, 1973a) consists of a set of steam-

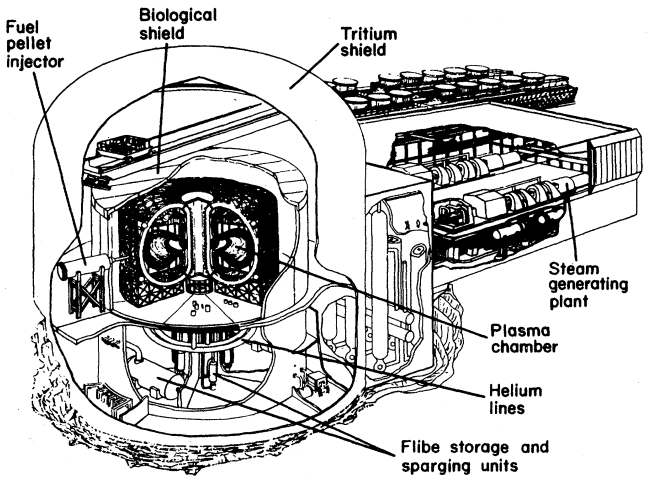

FIG. 15. General view of the PPPL conceptual fusion power plant.

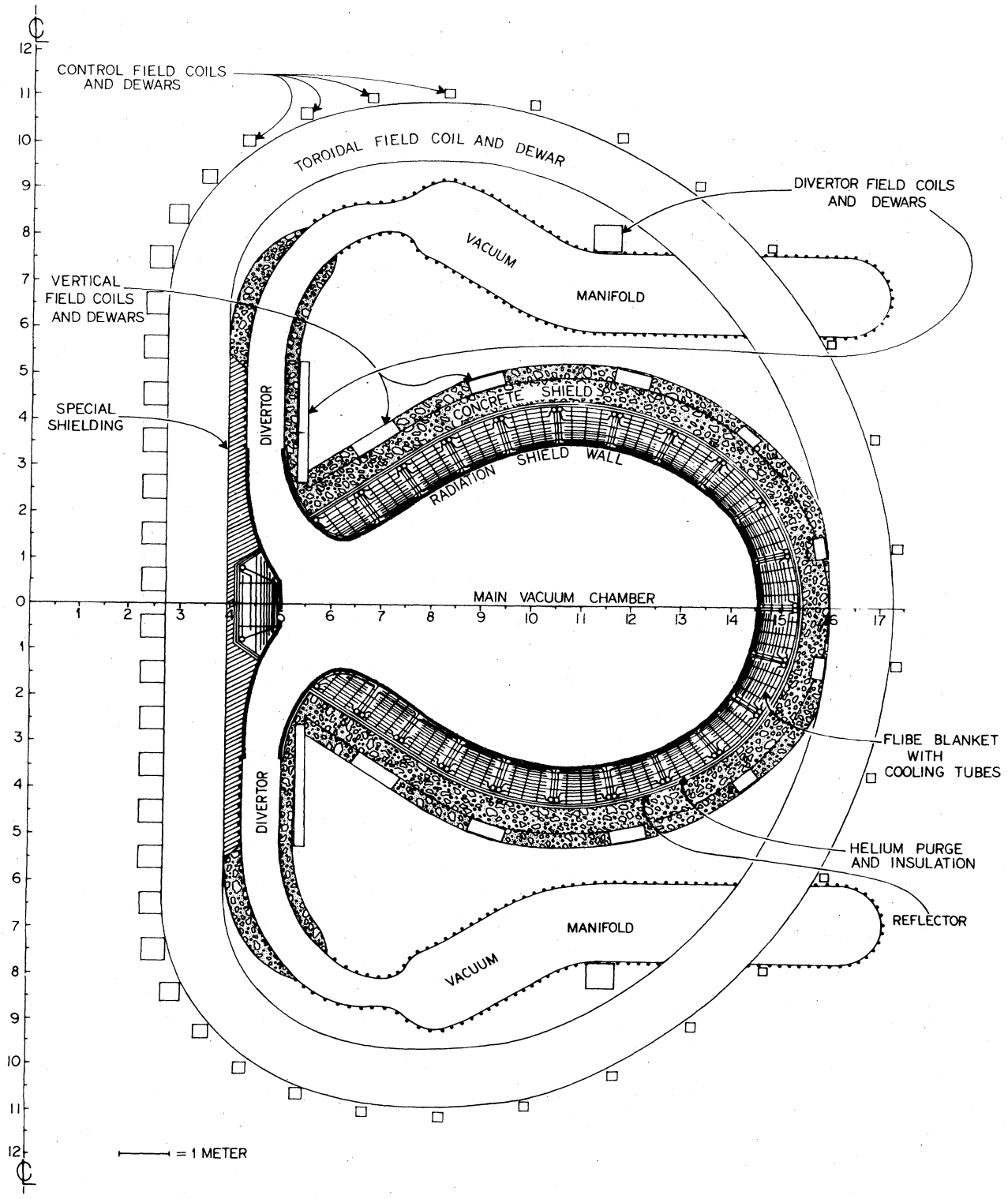

FIG. 16. Radial cross section of the PPPL tokamak-reactor divertor and toroidal magnet coil.

turbines (560 C to 370 C) operating off the reject heat of a "topping" potassium-vapor turbine (980 C to 590 C). The other two designs use lower-temperature structure and therefore more conventional steam conversion plants with correspondingly low thermal efficiencies. Their thermal and electrical power outputs are much larger (5000 and 1500-to-2500 MW, respectively). The recirculating power of the PPPL design derives largely from the helium circulators, while in the ORNL design the major component is the input to the neutral-beam injectors. The UWMAK design

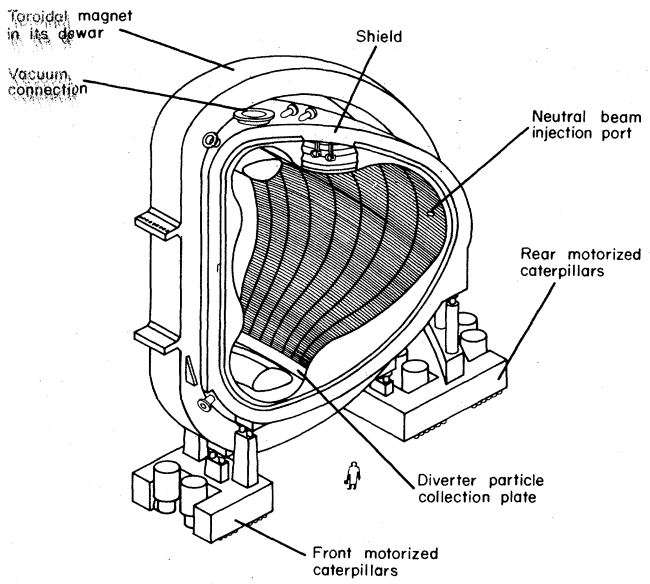

FIG. 17. Toroidal magnet, blanket and divertor module of the UWMAK.

assumes neutral-beam injection only during its 10-sec ignition phase, and it thereby makes a negligible contribution.

E. Conceptual burning, injection and fueling cycles

The burning cycles (Table V) are quite different for the PPPL and UWMAK devices, as opposed to the ORNL case. For the assumed neoclassical diffusion (cf., Sec. IV.B) the confinement time is much too long for burning equilibrium and the confinement time, τ_c, is "spoiled" to a value of 4 to 14 sec. For example in the UWMAK design the bremsstrahlung loss is increased by a factor of 7.5, and the confinement is decreased by a factor of 1800. The long burn time τ_B(5400 sec) is set by the L/R time of the plasma ring. Thus even though the PPPL and UWMAK reactors operate on long pulses, they are essentially steady-state devices since $\tau_B \gg \tau_c$. They are sustained by injection of D–T ice pellets, cored with argon impurity. The UWMAK burning equilibria are unstable (cf., Sec. III.B) and must be servo or feedback stabilized, while stability is maintained in the PPPL case, largely by the argon impurity. The burnup fraction is 7% to 8%. In the ORNL burning cycle (Etzweiler, *et al.*, 1973) the approach is quite different. The plasma, after ignition, is allowed to make an unstable excursion at its natural exponentiation growth rate γ_T (cf., Sec. III.B) to a high peak temperature, and beta, subsequently D–T fuel depletion (burnup fraction, 0.8) and synchrotron radiation cause a similarly sudden decrease in reaction rate, temperature, and beta. The plasma is then "driven" at an amplification factor Q between 6 and 13 by the neutral-beam injectors. No confinement spoiling is used and the neutral-beam injectors also fuel the plasma. The main burn and injection parameters are summarized in Table V.

In the UWMAK reactor, the Ohmic heating is excited for about 100 sec at low plasma density (3×10^{19} m^{-3}) with the plasma temperature leveling off at 2.13 keV. During the 100-sec rise of the toroidal current, the poloidal field also "soaks into" the plasma. Figure 18 shows that, for an initial temperature of 500 eV, with classical resistive heating at a constant current of 20 MA, the UWMAK plasma temperature on axis will level off at 2 to 3 keV after about 10 sec. In order to achieve ignition neutral beams of 500 keV, D and T ions are injected tangentially to a major circumference. At least 350 keV are required to penetrate the plasma adequately to cause the ion temperature to peak on axis. A total beam power input of 15 MW will cause ignition to occur in 11 sec. After ignition the temperature

TABLE III. First-wall neutron-blanket and fuel characteristics of the three conceptual tokamak reactors. The two ORNL columns refer to different burning cycles.

	ORNL			
	IIA	II	PPPL	UWMAK
First wall				
Radius (m)	4.1	4.1	4	5.6
Composition	Nb-1% Zr	Nb-1% Zr	PE-16	316 S.S.
Uncoll. 14-MeV fluence n/m²/yr[a]	0.46×10^{25}	0.70×10^{25}	2.1×10^{25}	1.5×10^{25}
Neutron curr. wall load (MW/m²)	0.42	1.04	1.76	1.25
Neutron blanket				
Thickness (m)	1.1	1.1	0.74	0.73
Breeding ratio	1.5	1.5	1.04	1.49
Material	Li, C, Nb	Li, C, Nb	Flibe,[b] PE–16	Li, 316 S.S.
Fuel				
Total T_2 inventory (kG)	6	6	5.6	13.5
Consumption (kG/D)	0.12	0.22	0.527	0.69
Doubling time, D	70	70	270	70
Total Li inventory, tonne	540	540	1855 flibe 163 Li	1400

[a] 85% Load factor.
[b] Helium cooled.

TABLE IV. Power balance quantities for the three conceptual tokamak power plants. Options for two different burn cycles are shown in the ORNL case. In all cases the output powers are time averaged over the burn cycle.

	ORNL			
	IIA	II	PPPL	UWMAK
Power balance:				
Thermal power P_T (MWt)	1136	3000	5250[a]	4690
Therm. Conv. eff, η_T	0.56	0.56	0.44	0.31[b]
Gross el. power Pe (MWe)	636	1680	2440[a]	1454
Circ. power frac, ϵ	0.27	0.060	0.14	0.084
Plant output P_P (MWe)	465	1500	2100[a]	1332
Amplification Q	10	37	15	...
Plant eff, η_P	0.41	0.50	0.40	0.29[b]

[a] These power levels may be reduced by 23% owing to recent re-estimates of the nuclear energy derived from neutron blanket reactions (M. W. Abdou and R. W. Conn, private communication).
[b] These low efficiencies stem from the 550 K operating temperature of UWMAK, required to limit corrosion in the SS–Li system.

TABLE V. Burn and injection parameters of the three conceptual tokamak reactors. In the ORNL case two burn-cycle options are shown.

	ORNL			
	IIA	II	PPPL	UWMAK
Burn:				
Ion dens, initial (m^{-3})	6×10^{19}	6×10^{19}	5×10^{17}	3×10^{19}
Ion dens, Burn (m^{-3})	5×10^{19}	3×10^{19}	5×10^{19}	8×10^{19}
Ion temp. Max (keV)	100	100	30 (av)	11
Ion temp, burn (keV)	20	40	30	11
Burn time (sec)	600	270	5820	5400
Cycle time (sec)	630	300	6000	5790
Confinement time (sec)	10^5–10^6 sec	10^5–10^6 sec	3.9	4
Fuel burnup	0.8	0.8	0.088	0.072
Fuel	Neutral beam		DT pellet	
Injection:				
Type	Neutral beam		...	Neutral beam
Injector eff, η_I	0.66[a]	0.45[a]	...	...
Inj. power (MW)	114 (av.)	80 (av.)	...	15 Peak
Beam energy (MeV)	0.3–3	0.3	...	0.5
Total inj. curr. (A)	94	320	...	30

[a] Corrected for plant housekeeping power.

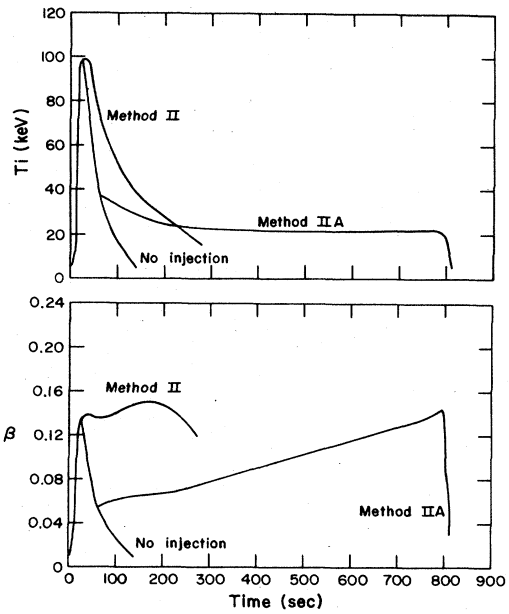

FIG. 19. ORNL tokamak burn-injection cycle (Etzweiler *et al.*, 1973). Toroidal beta and ion temperature versus time.

rises to its servo-stabilized equilibrium value of 11 keV ($T_e \approx T_i$), and the density is raised to its final value of 8×10^{19} m^{-3} by pellet injection (20-μm pellets at the rate of 20×10^6 sec^{-1}). After the burn the fueling and toroidal current are decreased and impurities are injected to cool the plasma to 500 eV, and the plasma is driven to the walls. The system is then pumped out and refueled with fresh gas. The divertors and poloidal field are then reestablished. From the end of one burn to the beginning of the next is 390 sec, giving a 93% duty factor.

In the ORNL case we consider two injection-burn strategies (II and IIA of Etzweiler, *et al.*, 1973) as shown in Figs. 19 and 20. The authors also treat additional Cases I and IA where the fuel density is kept constant. Each begins with a pulse of toroidal current for preignition heating followed by neutral-beam injection to ignition at a temperature of about 5 keV. Thereafter the plasma makes an unstable excursion in about 20 sec to a peak temperature of 100 keV, and a peak toroidal beta of 15%. In Method II the injectors are then turned on to sustain the plasma at constant power, nearly constant β, but decreasing T_i, for 270 sec. In Method IIA the injectors are turned on when T_i has fallen to 40 keV, and β to 5.5%, and sustain the plasma at a lower constant power for 600 sec. Beta is restored to its maximum value of 15%. At the end of each burn cycle injection is stopped, and T_i falls below ignition in tens of seconds. The plasma diffuses to the wall and the system is pumped, refueled, and reignited after a time τ_p, assumed to be 30 sec. The duty factors of 0.5 and 0.3, as well as the large injected powers in relation to the small thermal powers, result in the recirculating power fractions of Table IV.

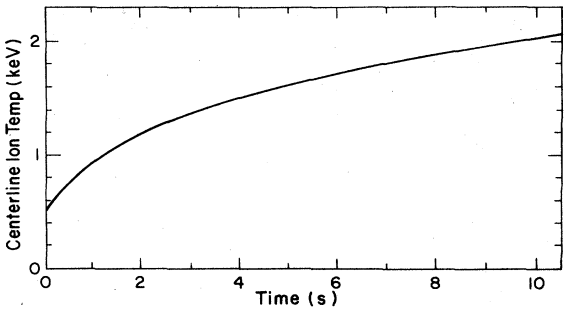

FIG. 18. UWMAK tokamak reactor ion temperature as a function of time for joule heating alone.

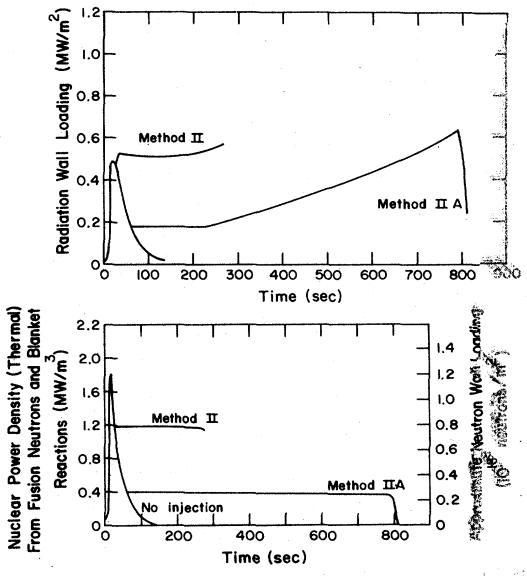

FIG. 20. ORNL tokamak burn-injection cycle (Etzweiler *et al.*, 1973). Nuclear power density and wall loading (Sec. II.B) versus time.

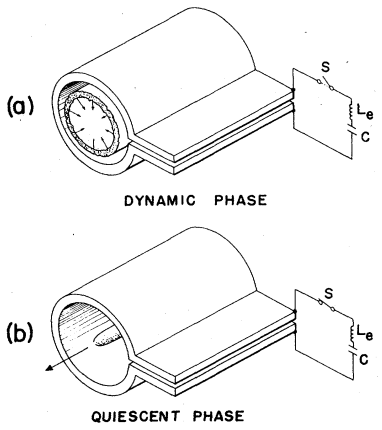

FIG. 21. Illustrating the operation of a theta-pinch experiment.

V. THE THETA-PINCH REACTOR

A. Basic concepts of theta-pinch systems

Unlike the other magnetic confinement systems, the theta pinch is a high-beta device ($\beta \approx 1$) in which very little penetration of the magnetic field into the plasma occurs. It is characteristic of these devices in toroidal geometry that the aspect ratio is very large, of the order of 100, roughly two orders of magnitude larger than for the tokamaks. The toroidal confinement principle is that of a high-beta stellarator (Scyllac) (Ribe and Rosenbluth, 1970; Burnett *et al.*, 1971; Fünfer *et al.*, 1973, 1974; Ellis *et al.*, 1974) in which small poloidal helical fields are superimposed on the confining toroidal field to provide toroidal equilibrium (See Appendix I). (In the case of the tokamak, the poloidal field of the toroidal current provides the toroidal equilibrium.) In the theta pinch the plasma density ($\sim 10^{22}$ m^{-3}) is also two to three orders of magnitude larger than in the magnetic mirror and tokamak, and confinement times are correspondingly shorter. Burning times τ_B in the theta-pinch reactor are of the order of 0.1 sec, rather than $\sim$1000 sec, for the tokamak case. This relative ordering of magnitudes follows from Eq. (II.2) where thermonuclear power density varies as n^2. The theta pinch is inherently a pulsed device because of its impulsive method of heating and its high instantaneous power density. For a typical cycle time $\tau_C \sim 10$ sec, the duty factor $\tau_B/\tau_C \approx 10^{-3}$ results in average power densities and wall loading which are about the same as for the other two concepts. Total toroidal magnetic energies are of the order of 100 GJ, also comparable to those of the other concepts. However, this energy is pulsed repetitively in and out of the compression-confinement coil from an external power supply (typically a superconducting magnetic or inertial energy store) with risetimes of approximately 0.03 sec. This feature and the requirement of adapting the high voltage necessary for shock heating to the nuclear environment of the reactor core are essential determining factors in the design of the theta-pinch reactor.

In the following, we discuss the Los Alamos–Argonne Reference theta-pinch reactor (RTPR) conceptual design (Burnett *et al.*, 1974; Krakowski *et al.*, 1973; Ribe *et al.*, 1974) which is an outgrowth of earlier exploratory work (Ribe *et al.*, 1965; Bell *et al.*, 1970) on high-β fusion reactors.

B. Principles of operation

The basic principles of present-day θ-pinch experiments are illustrated in Fig. 21. Ionized gas (usually deuterium) is produced inside a single-turn coil by a high frequency oscillating magnetic field in the axial direction. Following this, a large current (in the poloidal, or θ, direction) is suddenly fed to the coil from a capacitor bank. This rapidly fills the coil with magnetic field parallel to its axis. During the dynamic (or "shock-heating") phase, the surface of the plasma is driven rapidly inward by this axial field, heating the ions and electrons. Later, there is a quiescent (adiabatic-compression) phase after the magnetic field is built up on a much slower (adiabatic) time scale to a steady value in the coil. The plasma is then held in a cigar shape by the steady magnetic field, gradually being lost out its ends along magnetic lines as indicated by the arrow for a linear geometry. For a torus the ends and the end loss are eliminated.

In the present experiments a single-turn coil and a single capacitor bank furnish both the shock-heating and adiabatic-compression fields. However, a theta-pinch reactor will be a staged theta-pinch, (Friedberg *et al.*, 1974) so-called because it employs separate energy sources for the shock-heating and adiabatic-compression stages. The shock-heating coil is thin and can be liquid-metal-cooled. It is connected to a low-energy, high-voltage circuit whose energy content is a minor factor in the overall energy storage system. The energy in the magnetic-compression field, which is preponderant, is furnished by a low-voltage multiturn coil which produces a more slowly rising magnetic field (following the shock-heating field), appropriate to adiabatic compression of the shock-heated plasmas [cf., Sec. II.C, Eq. (II.10)]. Such a coil is economical of joule electrical losses and leads to a satisfactory excess of reactor power output (low circulating power fraction). The compression coil is also of sufficient size to accommodate an inner neutron-moderating blanket.

Figure 22 shows schematically the essential time sequence of a staged theta-pinch fusion reactor. In the shock-heating stage, a magnetic field B_s having a risetime of the order of one μsec and a magnitude of 1–2 T drives the implosion of

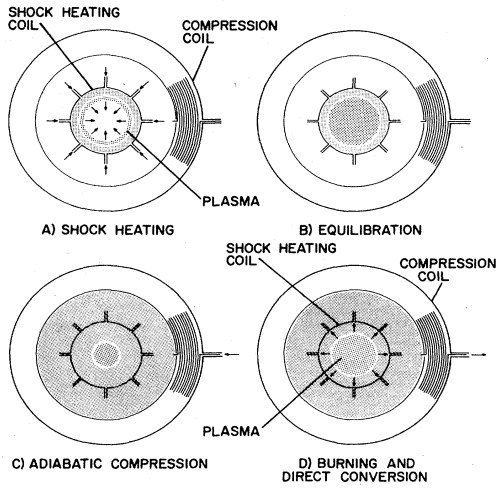

FIG. 22. Illustrating plasma heating and burning in a staged theta-pinch conceptual fusion reactor.

a fully ionized plasma whose initial density is of the order of 10^{21} m^{-3}. After the ion energy associated with the radially directed motion of the plasma implosion has been thermalized, the plasma assumes a temperature T_E of the order of 1 keV, characteristic of collisional equilibration of the ions and electrons [cf., Eq. (II.8)]. In Fig. 22 the darkly shaded areas represent magnetic field perpendicular to the plane of the figure. After some hundreds of μsec the adiabatic compression field, applied by energizing the compression coil, rises to the value B_s. The arrow in Fig. 22c indicates the direction of magnetic energy flow into the magnetic-compression system. The plasma is then compressed to a smaller radius during the risetime ($\sim$0.03 sec) of the compression field, and its temperature is raised to a value somewhat above ignition ($\sim$5 keV). The D–T plasma then burns for $\sim$0.1 sec, and it produces 3.5-MeV α particles which partially thermalize with the electrons and the D–T ions as the burned fraction of plasma increases to a few percent. As a result, the plasma is further heated. During the burning phase, since β is approximately unity, and since B is approximately constant, the plasma expands against the magnetic field (cf., Sec. II.D, Fig. 4), doing work ΔW which is about 62% of the thermonuclear energy deposited by α particles. This work produces an emf which forces magnetic energy out of the compression coil (cf., the arrow in Fig. 22D) and back into the compression magnetic-energy store. This high-β, α-particle heating and the resulting direct conversion are important factors in the overall reactor power balance.

Figure 23 shows an idealized implosion-heating coil with eight feed slots to admit the magnetic field B_s which drives the plasma implosion of velocity v_s. Ideally, as the sheath separating the magnetic field from the $\beta = 1$ plasma of density n_A (corresponding to an undissociated filling pressure p_A of D_2) advances, the plasma deuterons are propelled elastically radially inward at velocity $2v_s$. After the ions have passed the axis of the system and been repeatedly reflected from the cylindrical magnetic piston, they assume a temperature T_{sh} given by (Friedberg *et al.*, 1974)

$$B_s^2 = 7.12 \times 10^{-2} p_A T_{sh}, \tag{V.1}$$

where p_A is expressed in Torr, T_{sh} in electron volts, and B_s in T. For deuterons, the sheath velocity v_s is related to T_{sh} by the relation

$$v_s = 7.68 \times 10^3 T_{sh}^{1/2}. \quad \text{(m/s)} \tag{V.2}$$

As the plasma sheath leaves the insulated wall of the implosion-heating coil it generates a back emf corresponding to an azimuthal electric field

$$E_\theta = v_s B_s = 2.06 \times 10^3 p_A^{1/2} T_{sh}. \quad \text{(V/m)} \tag{V.3}$$

In the RTPR this voltage has a magnitude of about 2×10^5 V/m (2kV/cm).

During the implosion-heating process the electrons (having small mass) receive negligible momentum or energy from the implosion. After a few $\times 10^{-5}$ sec however, electron–ion collisions lead to a common equilibrium temperature $T_E = 1/2 T_{sh}$ for the ions and electrons. It can be shown (Friedberg *et al.*, 1974) that the plasma radius after equilibration is $a_E = x_{sh} b$, where the inverse compression factor is x_{sh}, independent of n_A, and B_s, as long as B_s rises in a time short compared to implosion time b/v_s and remains constant thereafter. Here b is the first-wall radius.

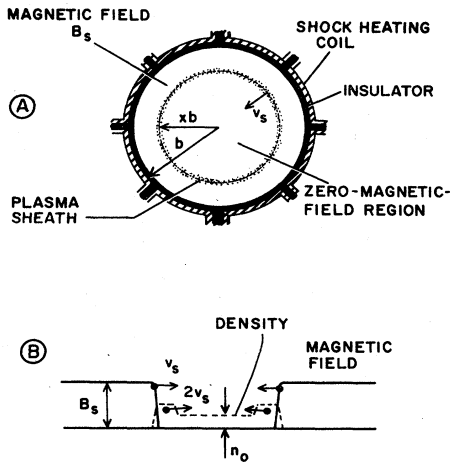

FIG. 23. Illustrating the processes involved in the shock (implosion) heating of plasma in a theta pinch.

In theory and in present experiments a programmed "free-expansion" field is applied such that a field $B_s/\sqrt{2}$ provides the initial implosion. After the ions are propelled through the axis, the piston field is removed for a short period while the plasma ions expand freely to a radius almost equal to b. A field B_s is then reapplied to reflect the ions, after which equilibration occurs in the constant field B_s. Under these circumstances it can be shown that $x_{sh} = 0.76$ and the three coefficients of Eqs. (V.1, 2, 3) become (using now the average D–T ion mass, instead of the deuteron mass) 4.93×10^{-2}, 4.08×10^3, and 0.64×10^3, respectively.

Following equilibration, the plasma is compressed from x_{sh}, B_s to the final values x_0, B_0 according to the adiabatic-compression laws, (cf., Sec. II.C)

$$T_0 = T_e (x_{sh}/x_0)^{2(\gamma-1)}, \tag{V.4}$$

$$B_0 = B_s (x_{sh}/x_0)^{\gamma}, \tag{V.5}$$

where γ is the specific heat ratio of the plasma, which is equal to $\frac{5}{3}$ on the compression time scales of the reactor. There result the scaling relations (Krakowski *et al.*, 1973) (corresponding to free-expansion implosion of D–T ions):

$$E_\theta = 0.244 x_0^{7/3} T_0^{1/2} B_0 \tag{V.6}$$

$$B_s = 4.31 (B_0^{2/5} E_\theta / T_0^{1/2})^{5/7}. \tag{V.7}$$

C. Reactor design and component considerations

A cross section of the reactor core is shown in Fig. 24. The first wall is composed of the ends of insulator-coated, niobium blanket segments in which lithium is used as a breeder, moderator, and coolant. The insulator must be thin enough to allow extraction of heat from the plasma bremsstrahlung and nuclear radiation, as well as to allow passage of heat from the plasma as it is being quenched at

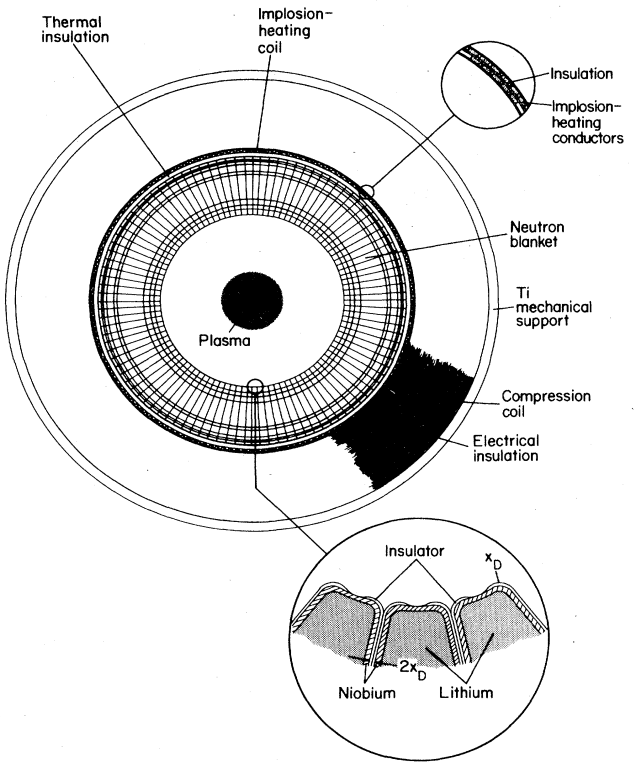

FIG. 24. Cross section of the neutron blanket, shock-heating coil and adiabatic-compression coil of the LASL–ANL Reference theta-pinch reactor (RTPR).

the end of a burning pulse. Simultaneously the insulator must support the back-emf electric field E_θ during the fraction of a microsecond of implosion heating. During this short time of high-voltage stress there is negligible radiation present, compared to that later during the burn when the density and temperature are much higher (cf. Fig. 29). Hence the insulator requirement of a resistivity of $\gtrsim 10^6$ Ω-m and a dielectric strength $E_D \sim 10^7$ V/m at a temperature in the neighborhood of 1000°C need not be met in the presence of a high radiation field. Allowing N blanket segments, each coated with an insulator of thickness X_D, to support a total voltage of $2\pi bE_\theta$, we find

$$N = \pi bE_\theta / X_D E_D. \tag{V.8}$$

Heat transfer calculations (Krakowski *et al.*, 1973) show that $X_D = 3 \times 10^{-4}$ m is adequately thin, corresponding to $N = 100$ blanket segments. With niobium metal structure as shown in Fig. 24 it is found that the blanket provides a tritium breeding ratio of 1.11 and an energy multiplication (Sec. II.B) such that $ME_n = 20.5$ MeV, while adequately protecting the room-temperature copper compression coil from nuclear radiation.

In the RTPR design (Krakowski *et al.*, 1973; Bunch *et al.*, 1973) a reference insulator of polycrystalline Al_2O_3 is chosen because of its favorable dielectric properties at high temperatures. However neutron-induced swelling presents a severe limitation in this substance. Research on Y_2O_3 indicates an absence of swelling at fluences approaching 10^{26} neutrons/m², which would allow a first-wall life of one to two years at the reactor power level corresponding to a cycle time of 10 sec. This is comparable to the two-year limit imposed by neutron embrittlement in the UWMAK first wall, as discussed in Sec. IV.D. Another promising approach is to develop glassy insulators of known favorable high-temperature dielectric properties which have present neutron-damage tolerances of the order of 10^{25} neutrons/m².

The implosion-heating coil of Fig. 24 is of an end-fed design (Krakowski *et al.*, 1973) in which a double layer of V-shaped conductors (Fig. 25, Item 3) allows E_θ and B_s to be induced inside the first wall without appreciable components of (longitudinal) E_ϕ and B_θ. The field B_s is admitted to the plasma region by flux flow between the insulated metal blanket segments, being excluded from them by the skin effect during the short shock-heating times. Later the magnetic field penetrates the segments during the longer times of electron–ion equilibration and adiabatic compression.

The compression coil has sufficient thickness (low current density) that joule losses of the theta currents which produce the compression field B_0 are reduced to such a level that their contribution to the plant circulating power is acceptable. The coil is layered in ~2-mm thicknesses to reduce to negligible proportions the eddy-current losses during the 0.03-sec rise and fall of the compression field. Similarly the segments of the blanket provide negligible eddy-current losses in the lithium and graphite since their thicknesses are less than the skin depth in the rising compression field. An assembled 2-m module of the reactor core is shown in Fig. 25. Figure 26 shows such a module in place in a con-

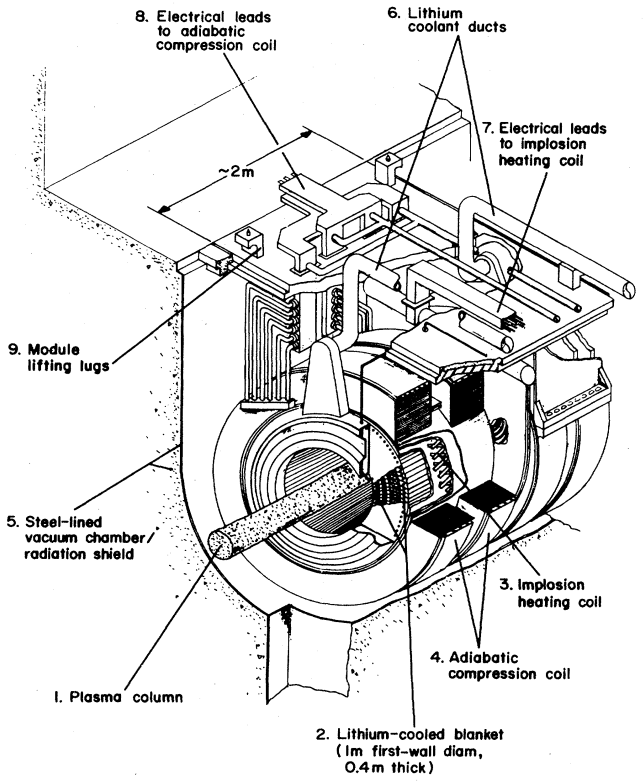

FIG. 25. Illustrating an assembled theta-pinch reactor core module.

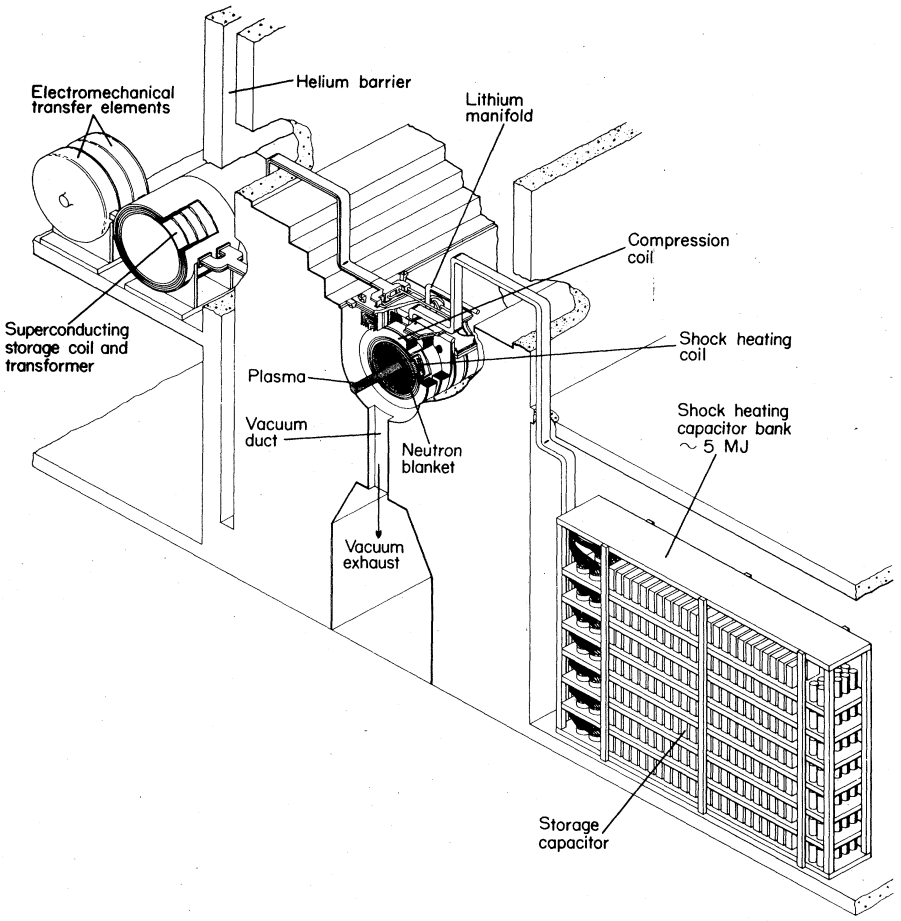

FIG. 26. Section of the conceptual RTPR power plant corresponding to one two-meter core module.

ceptual section of the power plant. At the left is indicated a realistically sized element of the superconducting magnetic energy storage system where a rotating transfer element energizes the compression coil. An over-all view of the conceptual 2000-MWe RTPR power plant is shown in Fig. 27. The reactor ring is below ground in an evacuated tunnel with a helium barrier to prevent escape of tritium. The transfer cask allows removal of the radioactive core modules to the central hot cell for easy replacement in case of failure.

D. D–T burn dynamics

1. The burn cycle

When a plasma begins to burn, the α-particle reaction products thermalize within the plasma, thereby increasing the internal energy of the ions and electrons. In a low-β plasma confined by a constant magnetic field B with negligible particle and energy losses, the plasma pressure increases and the plasma beta also increases. The pressure in a unity-β plasma, however, remains constant and work is done against the magnetic pressure, $B_0^2/2\mu_0$ (cf. the discussion in connection with Fig. 4). This work represents a direct conversion of thermonuclear energy into electrical energy.

The magnetic compression and decompression cycle, as well as important energy quantities, is shown in Fig. 28. Here B_0 is the maximum compression field and B_Q is the "quench" field. After the ion–electron equilibration which follows the implosion-heating stage, the compression field rises in 31.4 msec to a peak value of 11 T at point b, as energy is transferred to the compression coil from a cryogenic magnetic energy storage. The major portion of the D–T burn occurs between points b and c under conditions of constant magnetic pressure, $B_0^2/2\mu_0$. The compression field is reduced at point c and attains a value $B_Q = 3.2$ T at point d, most of the magnetic energy being permitted to flow back into the magnetic energy storage. Note that the burn bc represents the beginning of a thermally unstable excursion (cf., Sec. III.B), which is terminated by the decompression and quench stage cd.

At the end of the quench stage, point d, the D–T reaction rate is negligibly low ($kT \sim 9$ keV). On a much longer time scale, the magnetic field is programmed to decrease slowly, thereby preventing the hot plasma from touching the first wall. During the period from points d to e, the plasma is maintained at a constant radius and internal energy is transferred through a neutral-gas layer (Oliphant, 1973) to the reactor blanket.

The alpha-particle thermalization, plasma heating, and plasma expansion have been computed numerically (Oliphant *et al.*, 1973). These calculations indicate that ignition occurs slightly prior to point b, and the burn continues almost to point d. Shown as a function of time on Fig. 28

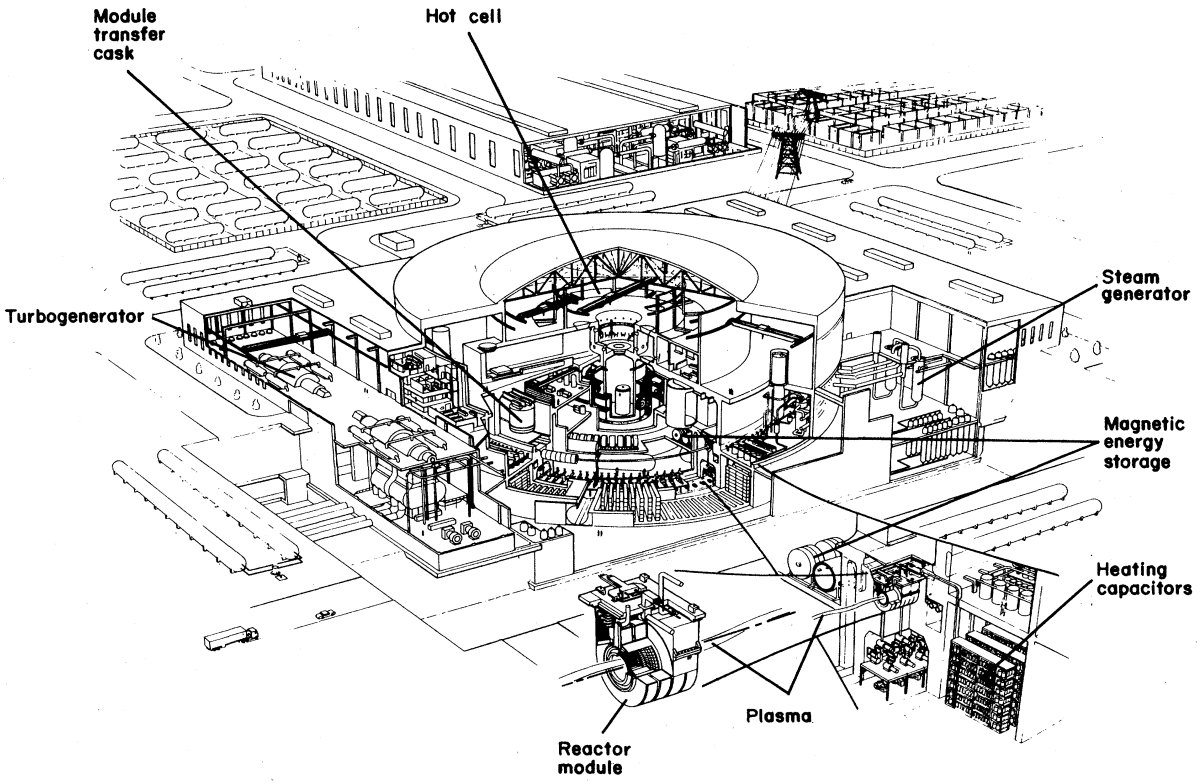

FIG. 27. Overall view of the LASL–ANL conceptual theta-pinch reactor (RTPR) power plant.

are the plasma internal energy $W_{\rm int}$, the energy deposited in the blanket by neutrons (Q_N = 20.5 MeV/neutron), W_n, and the bremsstrahlung energy, $W_{\rm br}$. Estimates of heat transport from Eqs. (II.13) through (II.18) show ion–ion thermal conduction to be the dominant process. For the parameters of Fig. 29 the corresponding quantity τ_E exceeds the burn time by about an order of magnitude.

Figure 29 summarizes the time dependence of the plasma radius, ion density, α-particle density, plasma temperature, and α-particle energy. Numerical values from these computations are used to determine the overall energy balance. The nominal 31 msec risetimes of the compression field represents a first estimate of an optimal process. The inertia associated with the massive machinery that transfers the compression field dictates large values for this time, whereas the need to maintain the implosion-heating field B_s for times of the order of milliseconds in order to allow the compression field to rise to the value B_s introduces complexities into the design of the implosion-heating power supply.

2. The direct-conversion cycle

The burn cycle (Oliphant *et al.*, 1973) is represented in the form of pressure volume and temperature-entropy diagrams in Fig. 30, and the stages of the cycle defined by Figs. 28 and 29 are indicated. In both cases, the portion of the cycle between points *e* and *a* is designated by dashed lines to indicate uncertainty in the path taken from the end of the cooling stage through the end of the implosion-heating stage. The direct-conversion work, ΔW = 9.8 MJ/m, generated during each cycle, is represented by the area of the pressure–volume curve, while the heat input Q_α = 15.8 MJ/m of the α particles is given by the area of the temperature–entropy curve. The intrinsic thermodynamic conversion efficiency of the cycle is $\Delta W/Q_\alpha$ = 62%, and ΔW is available to the reactor system at ~100% efficiency through the magnetic energy store. The thermonuclear energy W_n = 931 MJ/m, however, is available only through thermal conversion at an efficiency η_T (Sec. I.C.). The ratio of direct-conversion energy to thermally converted energy is $\Delta W/\eta_T W_n$ = 0.26 for η_T = 0.40.

The direct-conversion work has an appreciable effect on the net plant efficiency η_P, and the circulating power fraction ϵ for the theta-pinch reactor; in a sense, the direct-conversion process represents a topping cycle for the thermal-conversion plant.

E. Plasma cooling by a neutral gas layer

An attractive feature of a pulsed fusion reactor is the possibility of removing the α-particle "ash" resulting from the burnup of the D–T fuel mixture and injecting fresh fuel between burning pulses. No divertor is required, as in the case of a steady-state, toroidal reactor. A layer of neutral gas injected between the hot central plasma and the first wall is used to cool, neutralize and purge the partially burned D–T plasma (Oliphant, 1973). Preliminary calculations show that sputtering problems are alleviated because heat transfer to the wall, which would otherwise occur by

energetic ions, will now occur primarily by means of low-energy neutral atoms and to a lesser extent by ultraviolet and visible radiation.

The fuel cycling is accomplished in the following manner. At the end of the burning phase (point c in Fig. 28), the reaction is quenched by suddenly reducing the confining field to a value which allows the hot central plasma to expand to a radius which is close to that of the wall. Cold, neutral gas is rapidly introduced into the space between the central plasma and the wall at some time during the thermonuclear burn. The central plasma is cooled by the outward radial flow of heat through this gas layer to the wall. The confining field, which is programmed to maintain the outer radius of the plasma at a fixed value, decreases with time as the plasma is cooled. After the central plasma has lost most of its energy and is neutralized, it is removed by vacuum pumps.

In calculating the rate of heat transfer throughout the gas blanket, (Oliphant, 1973) it is assumed that the cooling layer is formed immediately after quenching by the introduction of a neutral gas of uniform density n_B and temperature T_w. A quasisteady temperature profile is quickly established by heat conduction through the gas layer to the wall. The thermal conduction within the plasma is high enough to maintain an essentially uniform temperature profile through the plasma region, since the plasma contains a very small magnetic field ($\beta \approx 1$). Therefore, the central plasma is represented in the calculation by a rigid, isothermal cylinder with a temperature T_a, which decreases in time in accordance with the amount of energy extracted. A "break point" in the thermal conduction from the plasma cylinder to the wall occurs at the transition from ion to neutral-atom heat conduction, reflecting the fact that atom thermal conduction is much greater than ion thermal conduction.

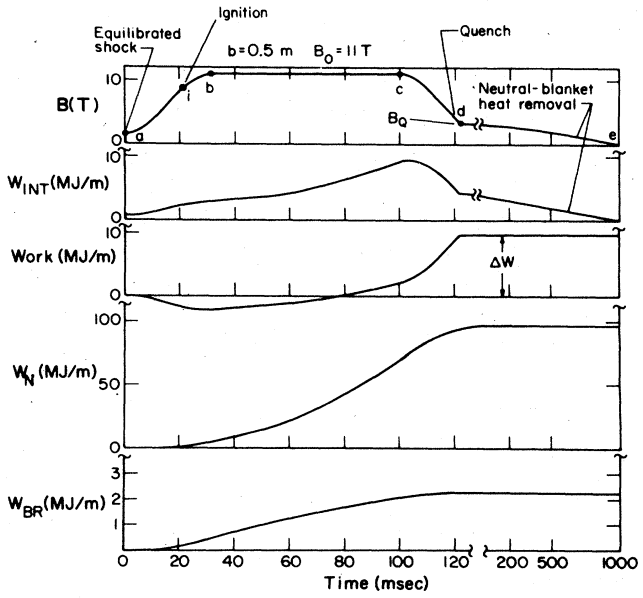

FIG. 28. Time history (Oliphant, *et. al.*, 1973) of the magnetic field used for adiabatic compression and time history of important energy parameters in the RTPR.

W_{int}: Total internal energy of plasma including the contribution from alpha particles;
ΔW: Direct-conversion work done by the plasma expanding against the compression field;
W_N: Total thermonuclear energy deposited in the blanket by neutrons;
W_{br}: Total bremsstrahlung energy radiated from the plasma.

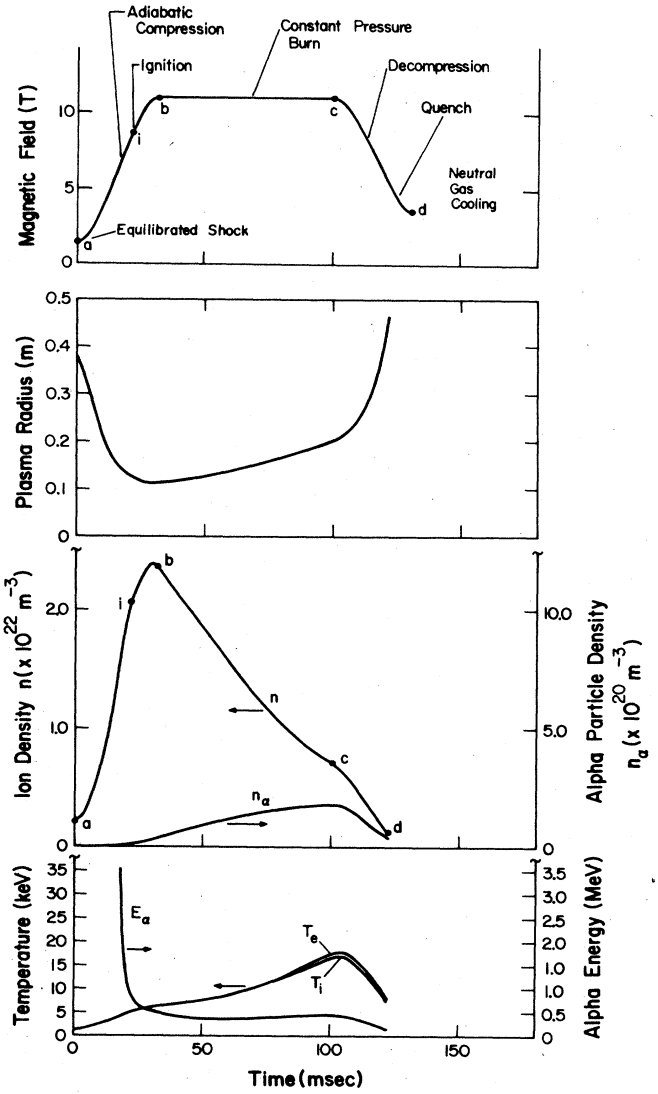

FIG. 29. Time history (Oliphant *et al.* 1973) of the RTPR electron and ion temperatures, mean α-particle energy, ion, and α-particle density, plasma radius and magnetic field.

An important feature which emerges from this analysis is that the central plasma temperature drops approximately linearly with time. To a good approximation therefore, it is possible simply to use a constant value for heat flow to the first wall. Typically the heat removal time is one second.

F. Reactor power plant characteristics and energy balance

Tables VI and VII provide a summary of the *RTPR* plasma, magnetic-field, first-wall, neutron blanket and fuel characteristics. The tritium inventory, breeding ratio and doubling time are seen to be comparable to those of the

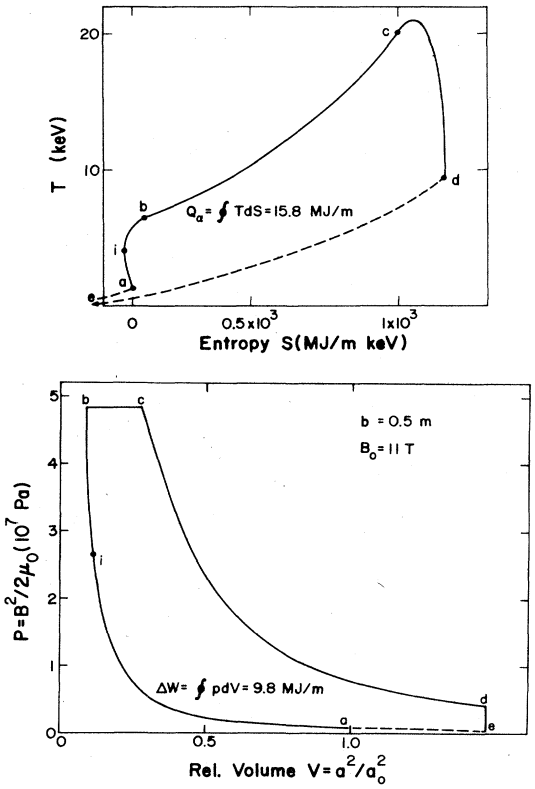

FIG. 30. Temperature–entropy and pressure–volume of the RTPR plasma during its compression, burn, and decompression phases (Oliphant *et al.* 1973). The letters *a* through *e* identify points corresponding to those in Fig. 28 and Fig. 29.

tokamak reactors (Table III). The wall loading is about 40% higher than for the PPPL and UWMAK reactors. The toroidal magnetic energy is less for the RTPR by a factor to 2 to 3, but owing to its pulsed character it should be compared to the poloidal magnetic energy of UWMAK. It is twice as large and rises much faster. The plasma burn quantities of Table VIII are quite different than those of the tokamaks, with the exception of the $n\tau$ and fuel-burnup parameters which are comparable.

In the power balance quantities of Table VIII we see power outputs, and circulating-power fractions comparable to those of the tokamak systems, with the exception of the UWMAK which has low thermal efficiency. A unique feature of the RTPR is the direct-conversion power, discussed above, which offsets the compression-coil joule losses to provide the relatively low circulating power and high plant efficiency. In Table VIII the value $Q = 31$ is the ratio of the maximum value of W_n to the value $W_{\rm int}$ at point *i* in Fig. 28.

In Krakowski *et al.*, (1973) two alternative thermal-conversion systems are used. One system involves a conventional steam cycle using a lithium–sodium-steam cycle at moderate temperatures (813 K maximum lithium temperature), which gives a thermal efficiency of 40%. The other system combines a potassium-vapor-topping cycle with a lithium-potassium-steam heat exchanger chain at high temperatures (1400 K maximum lithium temperature), which gives a more desirable thermal efficiency of 56%. Only the case of higher thermal efficiency is shown in Table VIII. The power level of the RTPR is inversely proportional to the cycle time τ_C since the essential plasma operation and energy balance are determined for a given burn pulse. The value $\tau_C = 10$ sec of Table VIII is chosen to give low wall

TABLE VI. Plasma and magnetic-field parameters for the RTPR conceptual theta-pinch reactor.

Plasma:	
Beta	0.8–1.0
Major radius R (m)	56
Plasma radius a: shock, burn (m)	0.38, 0.12
Plasma aspect ratio A, max	465
Magnetic fields:	
Shock, comp. coil radii (m)	0.91, 0.94
Shock field (T)	1.4
Compr., burn field (T)	11.0
Helical poloidal field (T)	0.8
Compr. field risetime (sec)	0.031
Supercond. mag. energy (GJ)	102
Shock-heating energy (GJ)	0.6

TABLE VII. First-wall, neutron-blanket and fuel characteristics of the RTPR power plant.

First wall:	
Radius b (m)	0.5
Composition	0.3 mm Ins, 1 mm Nb-1% Zr
Uncoll. 14-MeV fluence[a] (n/m²/y)	2.4×10^{25}
Neutron curr. wall load[a] (MW/m²)	1.9
Neutron blanket	
Thickness (m)	0.4
Breeding ratio	1.11
Doubling time (d)	40
Material	Li, Be, C, Ins, Nb
Fuel:	
Total T_2 inventory (kG)	2.2
T_2 Consumption[a] (kG/d)	0.35
Total Li inventory, Tonne	1580
Li consumption[a] (kG/d)	37

[a] 85% Load Factor

TABLE VIII. Plasma burn and plant power balance quantities for the LASL–ANL reference theta pinch reactor. Only the option having high thermal efficiency and larger cycle time is shown.

Burn:	
Shock ion density (m⁻³)	2.1×10^{21}
Burn initial ion density (m⁻³)	2.5×10^{22}
Shock temperature (keV)	1.1
Temperature at quench (keV)	17
Burn time (sec)	0.07
Burn parameter $n\tau$ (sec/m³)	8×10^{20}
Fuel burnup fraction	0.048
Cooling time (sec)	1–3
Power balance:	
Thermal power P_T (MWt)	3600
Thermal conv. Eff. (η_T)	0.56
Gross el. power $P/_E$(MWe)	2016
Circ. power fract. (ϵ)	0.13
Plant output P_P (MWe)	1750
Direct conv. power P_D (MWe)	350
Amplification q	31
Plant eff (η_P)	0.49
Duty cycle time (sec)	10

loading and long first-wall lifetime, rather than the most favorable economy, which would occur at the shortest cycle time allowed ($\tau_C \approx 3$ sec) by first-wall thermal loading.

VI. THE MAGNETIC-MIRROR REACTOR

A. Basic concepts

The toroidal reactors described in the previous sections allow the possibility, under sufficiently favorable confinement conditions, of plasma ignition; i.e., the plasma can be self-sustaining, requiring little or no injected energy. Under these conditions the amplification factor Q of the plasma (Sec. III.3) becomes very large. The magnetic-mirror, because it is an open-ended device with an intrinsic loss of plasma through the ends, does not admit such operation. Under ideal collisional circumstances, the theoretical value of Q for the plasma is only slightly greater than unity (Fowler and Rankin, 1966; Futch *et al.*, 1972). The magnetic-mirror reactor is therefore a driven power amplifier whose thermonuclear power output is a factor Q times its injected power. In order to achieve economical net electrical output with such low values of Q, a magnetic-mirror reactor would make use of the plasma energy which escapes from its mirrors in order to power the injectors. The means by which this is accomplished at high efficiency is called direct conversion (Post, 1970; Moir *et al.*, 1972; Smith *et al.*, 1974). This leads to a large recirculating power fraction, (Sec. III.3) of order unity. However the injection-power circulation loop need not pass through the thermal-conversion equipment, and the magnetic-mirror reactor should be economical if the efficiency of the direct conversion is sufficiently high and if the efficiency-weighted cost is lower than that of the thermal-conversion plant.

B. Principles of operation

In a simple magnetic mirror (Fig. 31), as in other containment devices, the plasma is contained transverse to the axis because of its inability to diffuse at an appreciable rate across magnetic lines. However, containment along the axis results from the "mirroring" of individual ion orbits by the converging field lines at the two ends, where the magnetic field strength B is larger than in the central plane by the ratio R, called the mirror ratio. An ion (Fig. 31) whose motion is directed predominantly toward a mirror with longitudinal kinetic energy $w_{||}$ will gain perpendicular (circular) energy $w_\perp$ around the field lines as it approaches a mirror. At the mirror it will have $w_\perp$ (mirror) $= w_\perp$ (center) $\times R$ and will have subtracted correspondingly from the longitudinal energy. In the case of sufficient $w_\perp$ (center) the ions are brought to rest so that $w_{||}$ (mirror) $= 0$. This occurs for those particles for which $w_\perp$ (center)$/w_{||}$ (center) is sufficiently large that the direction of the ion velocity lies outside some angle to the axis of the mirror. This angle defines a cone of directions called the loss cone, such that ions whose velocity directions lie outside it are contained, and the others are lost out the ends. Collisions between ions can send them into the loss cone and vice versa. There results a velocity distribution, called a loss-cone distribution (Fowler and Rankin, 1966), which is not Maxwellian and which largely determines the degree to which loss may exceed the collisional lower limit by influencing the kinds of unstable plasma waves that may occur.

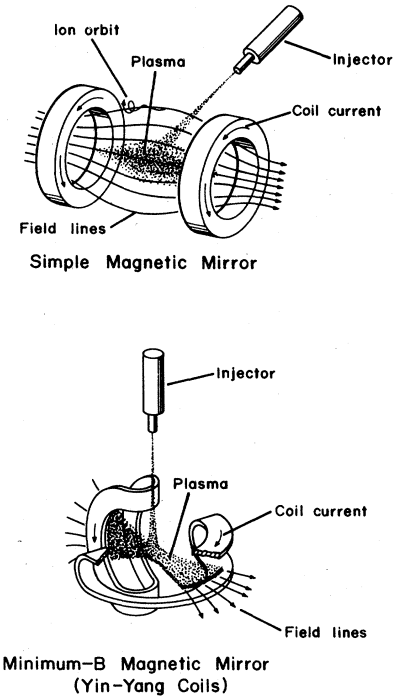

FIG. 31. Illustrating the principles of a magnetic-mirror device in cylindrical (upper) and minimum-B (lower) geometries.

It has long been known that plasma in the simple mirror geometry of Fig. 31 is unstable to magnetohydrodynamic (MHD) motions in which the plasma moves grossly across the magnetic lines. These MHD instabilities are driven by the gradients of magnetic field which occur when the field lines are curved convexly away from the plasma, as in the simple mirror system. However it has been shown theoretically and experimentally (Gott *et al.*, 1962) that a system whose magnetic lines are everywhere convex toward the plasma (lower part of Fig. 31) is stable to MHD modes. Such a system has minimum field strength B on its axis at the center of the system, and B increases outward in all directions. The minimum-B system of Fig. 31 has fan-shaped ends, one vertical and one horizontal, and the field is supplied by "Yin-Yang" coils (Moir and Post, 1969), which are among the most economical of the various possible coil systems for producing minimum-B mirror fields. This coil system has been chosen by the Lawrence Livermore Laboratory (LLL) group as the basis for their reactor design.

C. Mirror-reactor power balance and direct conversion

To sustain the plasma in a mirror device against collisional end loss it must be injected with a neutral beam from an injector whose power input is P_I, as shown in Fig. 31. The plasma is nearly opaque to this beam and absorbs its energy to sustain the thermonuclear reactions. The plasma thereby becomes an energy amplifier, because of the total thermonuclear power P_N, which it produces. The amplification factor Q (Sec. III.3) is an important quantity and is defined by the power flow diagram of Fig. 32:

$$Q = P_N/\eta_I P_I, \tag{VI.1}$$

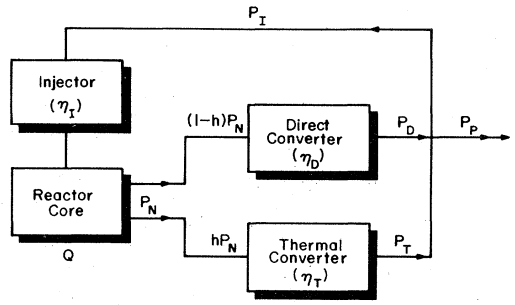

FIG. 32. Power flow diagram showing the main features of a magnetic-mirror fusion power plant with direct conversion.

where P_N is the sum of the neutron and α-particle contributions. We also consider η_I, the injector efficiency, which is the ratio of power deposited in the plasma to the power input to the neutral beam injector. In a reactor in which only that fraction h of P_N which occurs as neutron energy is available, through a thermal conversion cycle having efficiency η_T, the fraction of output energy which must be recirculated from the output of the thermal converter would be

$$\epsilon(\eta_D = 0) = P_I/h\eta_T P_N = 1/h\eta_T\eta_I Q. \quad \text{(VI.2)}$$

Here we have neglected the small effects of electromagnetic radiation from the plasma. Since η_I is at most unity, $h = 0.84$ (for D–T), and η_T is at most about 1/2 we see that a practical value for ϵ of about 10% would require $Q \approx 24$ and breakeven ($\epsilon = 1$) would require $Q = 2.4$. Under ideal conditions however, coulomb collisions between ions will limit Q to values in the neighborhood of unity. Thus a simple, thermally-converted D–T mirror reactor would not be economical because of the large amount of injector power recirculated from the thermal-conversion plant.

This unfavorable situation can be remedied by supplying the injection power directly from the energy of plasma ions which escape out the mirrors, as illustrated in Fig. 32. The fraction $(1 - h)P_N$ of thermonuclear power which occurs as α particles remains in the plasma and, along with $\eta_I P_I$, is converted to useful electrical output through a direct converter of efficiency η_D. The thermal converter provides useful output and that recirculating power necessary to sustain itself. According to Fig. 32 net power output occurs when

$$\eta_T h P_N + \eta_D[(1 - h)P_N + \eta_I P_I] - P_I > 0. \quad \text{(VI.3)}$$

Using Eq. (VI.1), this corresponds to the condition

$$Q > (1 - \eta_D\eta_I)/\eta_I[h\eta_T + (1 - h)\eta_D]. \quad \text{(VI.4)}$$

For $\eta_D = 0$, this reduces to the thermal breakeven condition given by Eq. (VI.2) with $\epsilon = 1$. The principle of direct conversion allows reactor operation at attainable Q values. The LLL group have shown (Warner *et al.*, 1973, 1974, 1974a) that values of η_D as large as 0.8 can be expected in a reactor situation. For $\eta_I = 0.8$, the inequality (VI.4) shows that reactor breakeven can occur for Q values as low as 0.8. In a practical system (cf., the power-flow diagram of Fig. 37) the injector power (560 MW) is comparable to the gross electrical power (750 MW). For this reason the direct-conversion equipment must cost substantially less, per kW, than the thermal-conversion plant to be economically acceptable.

It is to be noted that the existence of mirror losses, though disadvantageous with respect to confinement, also has some important positive aspects. It provides for a natural divertor action which is advantageous in several ways. Firstly, it will reduce wall sputtering effects since particles generally will escape through the mirrors before they can reach the reactor chamber walls. Secondly, mirror losses, which are selectively high for high atomic number particles and particles of low energy (owing to the positive ambipolar potential of mirror-confined plasmas) provide a powerful self-purification means whereby impurity ions are preferentially distilled from the plasma, thus helping to solve one of the potentially serious problems of future fusion reactors. Lastly, the mirrors help to make practical a means for the direct conversion of particle losses to electricity, an important element in the mirror reactor, to be later described.

D. High-energy neutral-beam injection

The efficiency of injection of energetic neutral beams into a mirror plasma has a substantial effect on the overall reactor efficiency. In addition the recent development of neutral-beam sources with "currents" of tens of amperes at ~20 keV has given considerable impetus to magnetic-mirror and tokamak experiments, in both of which the electrical-discharge-heated plasma serves as a target for further injection heating. However, in a reactor beam, energies greater than 100 keV will be required to penetrate the large plasmas. It is therefore important to extend both the energy and current of present sources. Hovingh and Moir (1973) and Hamilton and Osher (1974) provide an analysis of attainable values of injection efficiency and give a review of the literature on neutral-beam sources.

Figure 33 illustrates the injection of a neutral deuterium beam perpendicular to the axis of a magnetic-mirror reactor. To obtain high injection efficiency positive ions are produced in an ion source consisting of a plasma and an ion-extraction system at $E^+ \approx 2$ keV, after which the D^+ ions pass through an alkali (e.g., Cs)-vapor cell capable of about 25% conversion to negative ions. The negative ions are separated from the positives and neutrals and accelerated to energy $E_a \sim 200$ keV in order to be efficiently converted in a plasma neutralizer to deuterium atoms. It is estimated (Sweetman *et al.*, 1971), for example, that such an accelerator has a power efficiency of 92% at 3 MeV for 17 A of D_3^+ ions. For energies above 100 keV Riviere (1971) estimates that D^- ions are much more efficient producers of D^0 than any of the positive ion species and that the conversion efficiency is approximately 90%. Finally the neutrals enter the plasma where ionization by the electrons and charge exchange with the ions turn them into D^+ ions. Above ~150 keV the trapping fraction of the D^0 beam in the plasma is ~90%, while only 5% penetrate the plasma and a few percent cross the plasma as slow neutrals which do not ionize. Hovingh and Moir (1973) postulate thermal converters (Fig. 33) for the unused D^+ and D^0 ions at the input and a direct converter for the atoms which emerge from the reactor plasma. With this recovery of otherwise wasted energy the overall injection efficiency is about 90% for injected ener-

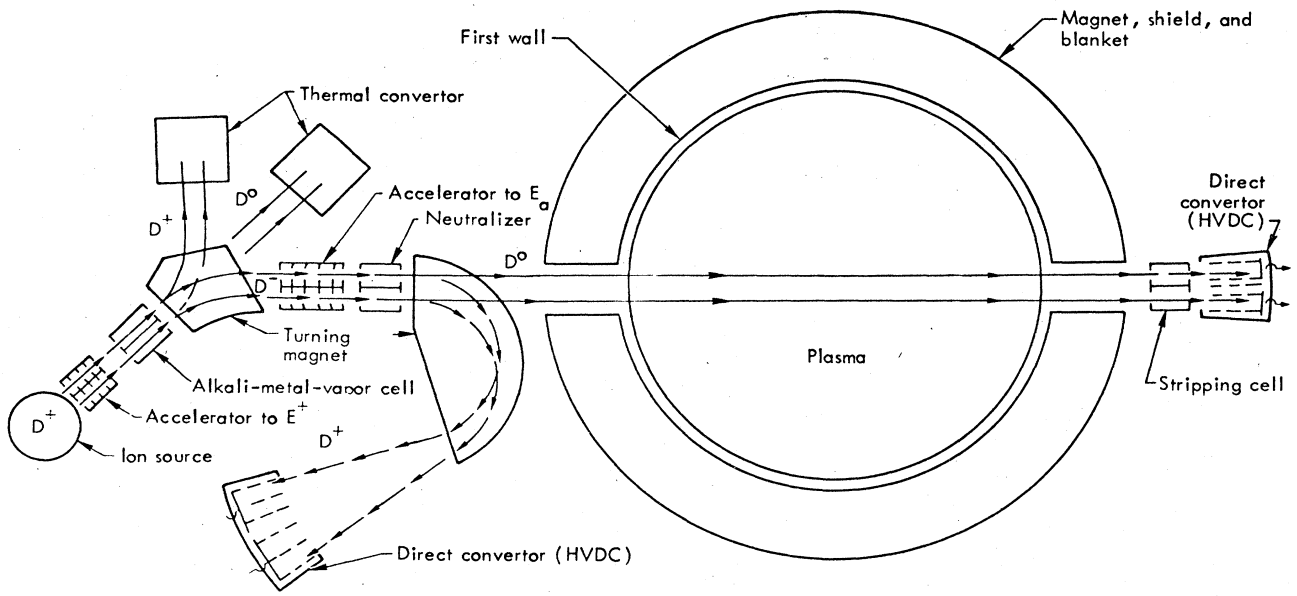

FIG. 33. Schematic diagram of a neutral-beam injection system for a magnetic-mirror reactor.

gies greater than 150 keV. Below this energy the efficiency decreases rapidly.

E. Direct conversion of the plasma energy

The method by which end-loss plasma energy from a magnetic mirror is converted to useful electric power is illustrated in Fig. 34. This shows a vertical section of a minimum-B mirror system like that in the lower part of Fig. 31 and a typical escaping ion orbit. First the escaping plasma is expanded in the decreasing horizontal fan-shaped magnetic field which extends 76 m from the mirror. In this process the plasma density is reduced, and the ion motion is converted, by means of an inverse of the mirroring process, into motion parallel to the field lines. After expansion, the plasma density is sufficiently low ($\sim 10^{13}$ ion/m^3) that charge separation of ions and electrons can occur. The electrons (whose energy is negligible) are diverted away vertically in the separator along the magnetic lines, but the ions escape across the lines and continue horizontally to a collector. Here, depending on their energy, the ions are decelerated in a periodic set of charge-collecting electrodes which collect them as they are brought to rest by the retarding potentials. There results a distribution of high voltages (corresponding to the energies of the escaping ions) on the collector electrodes which store the energy of the slowed-down ions. These voltages may then be brought to a common dc potential V_D by means of a set of inverters operating from electrodes with potentials greater than V_D and rectifiers from electrodes with potentials less than V_D.

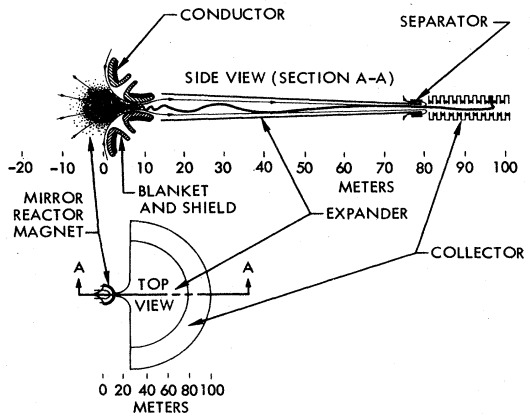

FIG. 34. Illustrating the main components of an apparatus for converting end-loss ion energy from a mirror reactor into direct-current electrical output.

F. Design features of a 200-MW conceptual D–T mirror reactor

The main parameters of the Lawrence Livermore Laboratory (LLL) conceptual magnetic mirror reactor (Warner *et al.*, 1973, 1974, 1974a) are summarized in Table IX through XII and in Figs. 35 and 36. The central plasma core is a

TABLE IX. Plasma and magnetic field parameters of the LLL 200 MWe DT mirror reactor.

Plasma	
Shape	Ellipsoidal, min. B, vol
Beta	0.85
Mean ion energy (MeV)	0.62
Z axis intercept (m)	3.5
Volume (m^3)	130
Density (m^{-3})	1.2×10^{20}
Beam area at mirror (m^2)	1.5
Magnet coil	
Radius (m)	10
Width of coil (m)	6.6
Coil separation, $2h$ (m)	4.2
Central field, (T)	5
Mirror field, (T)	15
Mirror ratio, vac.	3
Mirror ratio, $\beta = 0.85$	7.7

TABLE X. First-wall, neutron blanket and injector parameters of LLL 200 MWe DT mirror reactor.

First wall	
Composition	S. S.
Neutron curr. wall load (MW/m²)	1.6
Neutron blanket	
Thickness (m)	1.0 Av.
Breeding ratio	1.0–1.4
Energy mult.	1.1
Material	Li, S. S.
Injector	
Type	Neutral beam
Inj. eff. η_I	0.88
Inj. power (MW)	490
Beam energy (MeV)	0.55
Total inj. curr. (A)	890
Total inj. area (m²)	5

TABLE XI. Direct conversion parameters of the LLL 200 MWe DT mirror reactor.

Expander	
Expans. Ratio	100
Expander angle deg.	240
Ion energy at expander (MeV)	0.62
Radius (m)	76
Beam height (m)	0.87
Collector	
Depth (m)	22
Direct conv. eff., η_D	0.70
Number of elements	20

TABLE XII. Power balance of LLL 200 MWe DT magnetic mirror power plant.

Thermal power, P_N (MW)	590
Therm. conv. eff, η_T	0.45
Gross el power, P_E (MWb)	750
Power in neuts (MW)	470
Power in end-loss ions (MW)	610
Net elec. output (MW)	170
Amplification Q	1.2

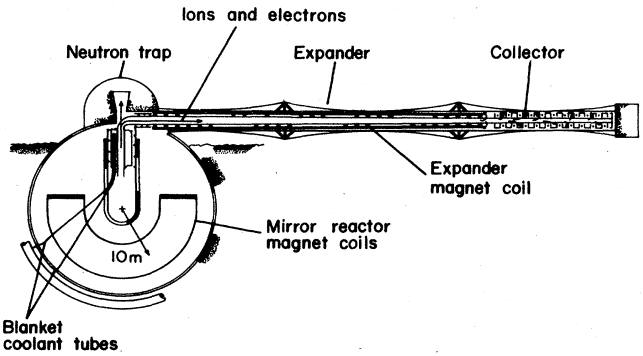

FIG. 35. Cross section of the LLL conceptual mirror reactor, showing the expander and collector of the direct-conversion equipment.

nearly spherical ellipsoid of about 3.3-m mean radius, injected by 490 MW of neutral beam at an average ion energy of 550 keV and a current of 890 A over a total area of 5 m². The mean plasma ion energy is 620 keV; its density is 1.2×10^{20} m^{-3}; and its β is 0.85.

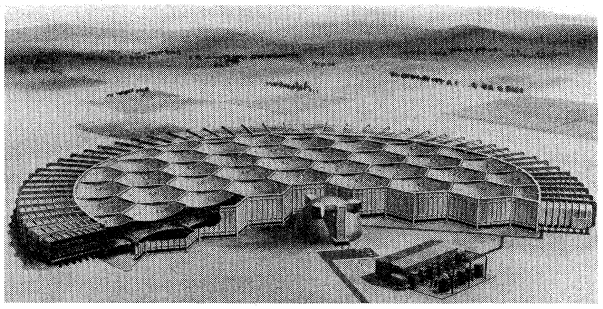

FIG. 36. Overall view of the LLL D–T magnetic-mirror fusion power plant. The direct-conversion equipment is shown behind the spherical reactor shield.

The Yin–Yang coils (Lee, 1973) have a mean radius in their "fan" planes of 10 m, a winding width of 6.6 m and a distance of 4.2 m between the parallel semicircular sides. All of the coil conductor is protected from neutron radiation by a 1 m-thick lithium blanket and shield, arranged so that the lithium flow is predominantly (90%) along magnetic lines. The coils are designed to produce a central field of $5T$ and a maximum field in the fans of $15T$ ($16.5T$ on the superconductor), corresponding to a vacuum mirror ratio $R_V = 3.0$ and an effective mirror ratio due to plasma diamagnetism $R_{\text{eff}} = R_V/(1-\beta)^{1/2} = 7.7$. The escaping plasma beam has an area of 1.5 m², produced by weakening the mirror field on one side over this limited area.

As shown in Fig. 35, the plasma beam escaping into the expander is first deflected by 90 degrees along the mirror magnetic lines which are bent by means of "steering" coils. The D–T neutrons emerging from the mirror are buried in a neutron trap. From the mirror to the end of the expander the magnetic field decreases from $15T$ to $0.15T$, decreasing the perpendicular ion energy by a factor of 100.

The expander has a horizontal radial extent of 76 m, accepting a beam height of 0.87 m over a total horizontal angle of 240°. Past the expander the electrons are deflected away by the separator coils, and the ion energies are stored over the 22-m radial length of the collector. The expander and collector are enclosed in a containment vessel of three radial sections separated by 1.7 m, composed of dished hexagonal modules, each with a horizontal dimension of about 32 m. Support columns intercept about 3% of the plasma beam. In addition to this flat containment vessel there is a spherical vacuum vessel, mostly below ground level, in order to limit tritium leakage to the atmosphere. An overall view of the power plant is shown in Fig. 36.

G. Reactor power balance

Table XII and Fig. 37 describe the power balance of the LLL mirror reactor. The thermonuclear power carried by neutrons is 470 MW, and the escaping power of charged particles is 610 MW. Emerging from the direct converter ($\eta_D = 0.70$) are 430 MW and from the thermal convertor ($\eta_T = 0.45$) are 320 MW, giving a gross electric power of 750 MW. Accounting for 560 MW of injection energy and 20 MW to power plant auxiliaries, the net electrical output is 170 MW, giving an overall plant efficiency of 27%. The system Q is chosen to be 1.2. The quantities in parenthesis

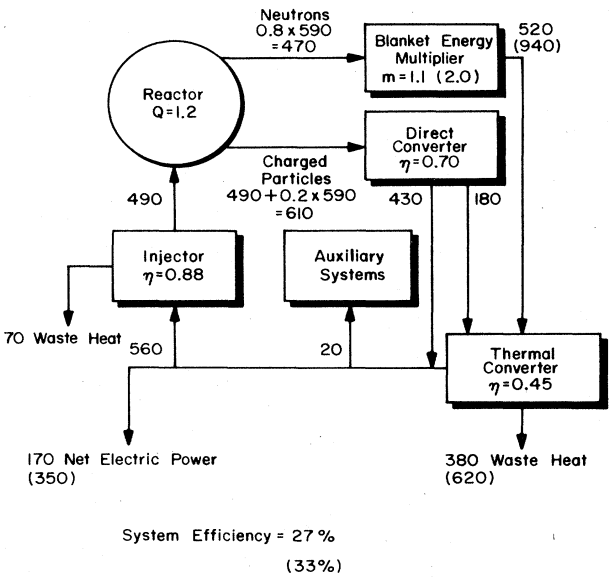

FIG. 37. Power flow diagram of the LLL 200-MWe magnetic-mirro power plant.

correspond to the power balance quantities with an assumed blanket energy multiplication $M = 2.0$, as might be obtained in blankets designed especially for high M values and low tritium breeding ratio. Note that the thermal efficiency of the *Li-SS* system here is taken as 0.45, in contrast to the value 0.31 for the UWMAK tokamak in Table IV. This reflects a less conservative view of the corrosion problem by the LLL group.

VII. LASER-DRIVEN REACTORS

A. Conditions for burning the plasma

The basic idea of the laser-driven fusion reactor (Lubin and Fraas, 1971; Metz, 1972) is to heat an initially frozen D–T pellet to ignition by the absorption of laser light (Fig. 38) in a time short compared to the time τ_e of its disassembly at the speed of sound in the material at the ignition temperature. The reaction time τ_r must also be short compared to τ_e, and a requirement for ignition is that the range of 3.5-MeV α particles must be short compared to the radius of the pellet.

It turns out that all of these conditions cannot be met at the solid (cryogenic) D–T density $\rho_0 = 0.213$ g/cm^3 (number density $n_0 = 4.7 \times 10^{22}$ cm^{-3}) with laser-beam energies which lie in what is now considered the range of attainable practice—hundreds of kilojoules. The solution is to compress the pellet by a factor of 10^3 to 10^4 (Nuckolls *et al.*, 1972; Brueckner and Jorma, 1973; Clarke *et al.*, 1973; Fraley *et al.*, 1973; Nuckolls *et al.*, 1973) above its solid or liquid density. In order to show how the laser energy is minimized we consider the various quantities which enter the plasma burn in terms of the pellet mass density ρ, radius R, and temperature T.

The speed of sound c_s at the extremely high temperatures in the pellet is closely related to the ion thermal speed

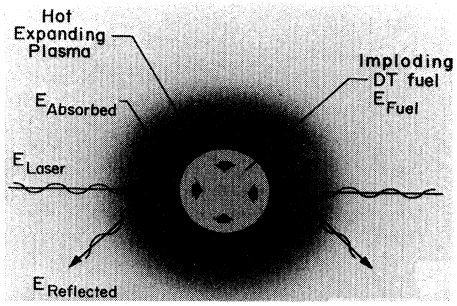

FIG. 38. Illustrating the absorption of laser light by a D–T fuel pellet in a laser-fusion reactor.

$v_{th} = (T_i/m_i)^{1/2}$, depending on what values of the specific heat ratios γ_e and γ_i apply to the electrons and ions. In general $c_s = [n(\gamma_e T_e + \gamma_i T_i)/\rho]^{1/2}$. However, because of the extremely high temperatures the material is usually fully ionized but not degenerate, and $\gamma_e = \gamma_i = 5/3$. Departures from these values can occur (Fraley *et al.*, 1973) but most often they are applicable and we shall take

$$c_s = (10/3)^{1/2}(T_i/m_i)^{1/2}. \tag{VII.1}$$

At $T_i = 10$ keV in D–T, $c_s = 0.9 \times 10^8$ cm/sec.

In both magnetic confinement and laser fusion the same general $n\tau$ conditions, discussed in Sec. III.D and III.E, must prevail if energy breakeven, ignition and appreciable burnup are to occur. However in the laser-fusion case it is conventional to replace the confinement time τ_c by the radial distance R traversed at sound speed, and the number density n by the mass density ρ. Thus the quantity ρR is used as a measure of many important effects. In order to take account of the fact that a pellet of initial radius R expands during the transit time R/c_s, reducing the D–T mass accessible in this time, and that spherical geometry places most of the mass near the outside of the pellet, the pellet disassembly time τ_e is reduced by a factor of four. Thus the confinement time at an effective temperature $T = 10$ keV is

$$\tau_e = R/4c_s \approx 0.3 \times 10^{-8} R. \tag{VII.2}$$

At $T = 10$ keV the Lawson breakeven condition that $n\tau_e = 6 \times 10^{19}$ s/m^3, corresponding to a burnup fraction $f_B = 0.003$ (Section III.E), becomes $\rho R \approx 4m_i c_s(n\tau) \approx 0.1$ g/cm^2, where we have used an average D–T ion mass $m_i = 4.2 \times 10^{-24}$ g.

In general D–T pellets in conceptual laser-fusion reactors make excursions after ignition to higher burnup fractions than in magnetic confinement reactors, and the temperature will remain in the region of 10 to 80 keV for most of the reaction time. From Fig. 3 we take $\langle\sigma v\rangle \approx 5 \times 10^{-22}$ m^3/sec and calculate the reaction time τ_r of Sec. III.E:

$$\tau_r = 1/n\langle\sigma v\rangle \approx 0.8 \times 10^{-8}/\rho, \tag{VII.3}$$

where ρ is in g/cm^3. The ratio τ_e/τ_r, which must be of order unity for appreciable burnup to occur, is given by

$$\tau_e/\tau_r = (\langle\sigma v\rangle/4m_i c_s)\rho R \approx 1/3\rho R, \tag{VII.4}$$

where ρR is in g/cm². The burnup fraction of Eq. (III.25) can now be expressed as

$$f_B(\tau_e) = \frac{\tau_e/2\tau_r}{1 + \tau_e/2\tau_r} = \frac{\rho R}{6 + \rho R}. \qquad \text{(VII.5)}$$

Thus for 30% burnup $\rho R \approx 3$ g/cm², while 5% burnup corresponds to $\rho R \approx 0.3$ g/cm².

As shown below, the feasibility of using pellet explosions to produce electrical power will depend on maximizing the ratio of the thermonuclear energy yield E_{out} to the thermal energy content E_{ie}. For a pellet of mass m (in g)

$$E_{\text{out}} = 1/2(m/m_i) f_B Q_T = 4.2 \times 10^{11} m f_B, \quad \text{(J)} \qquad \text{(VII.6)}$$

where Q_T (Eq. II.3) is the total energy (22 MeV) from a neutron and α particle which is available for thermal conversion. The thermal energy content of ions and electrons is

$$E_{ie} = 3(m/m_i) T = 1.1 \times 10^5 m T, \quad \text{(J)} \qquad \text{(VII.7)}$$

where T is in eV. Thus for an uncompressed pellet with $f_B = 0.3$, $T = 10$ keV we calculate $E_{\text{out}} \approx 10^{11}$ J/g and $E_{ie} \approx 10^9$ J/g, giving $E_{\text{out}}/E_{ie} \approx 100$. As we shall see below, for CTR applicability, this ratio must exceed 1000.

Since ρR is the quantity of interest in laser-pellet fusion, we express the mass as $m = (4\pi/3)(\rho R)^3/\rho^2$, and note that

$$E_{ie} = (4\pi/m_i)[(\rho R)^3/\rho^2]T = 4.5 \times 10^5 [(\rho R)^3/\rho^2] T. \quad \text{(J)} \qquad \text{(VII.8)}$$

For $\rho R = 3$ g/cm² (corresponding to $f_B = 30\%$) and a burning temperature of 10^4 eV, we find $E_{ei} = 2.7 \times 10^{12}$ J at the normal, solid D–T density of 0.213 g/cm³. Since the laser input energy will be larger than E_{ei} (by about one order of magnitude, see below) it is clear from (VII.8) that much higher densities must be used to reduce the required laser energies to the neighborhood of 1 MJ, which is in the range of attainable practice. This had led to the concept of using high compression ($\sim 10^4$) of the pellet density. Thus if we assume $\rho = 1000$ g/cm³, we find from (VII.8) the value $E_{ie} = 1.2 \times 10^5$ J, which is much more tractable.

Note that the sample pellet of the discussion above would have a mass of 110 μg and therefore a radius r at its cryogenic temperature of 0.5 mm. Equation (VII.2) gives a disassembly time $\tau_e = 1.38 \times 10^{-10}$ sec. The reaction time τ_r (Eq. VII.3) is 1.0×10^{-11} sec, and the fusion energy yield $E_{\text{out}} = 14$ MJ. The compressed radius of this sample pellet is 0.03 mm.

At such high densities as 1000 g/cm³, the spatial volume available to the electrons is so small that the Pauli exclusion principle forces them to occupy high momentum states. On the average, electrons with these momenta may have energies exceeding their temperature and thus become degenerate, exerting a pressure in excess of their thermal pressure nkT_e. The maximum energy of the degenerate electrons (the Fermi energy) is $\epsilon_F = (h^2/8m_e)(3n/\pi)^{2/3}$, and the "zero-point" pressure is $3/5 n\epsilon_F$. Thus we can identify an equivalent Fermi temperature

$$T_{ef} = 5.65\rho_0^{2/3} \quad \text{(eV)}. \qquad \text{(VII.9)}$$

At $\rho = 10^3$ g/cm³, $T_{ef} = 0.56$ keV.

An additional requirement for ignition and burn is that the D–T α particles be contained. Fraley *et al.* (1973) derive the following expression for the α-particle range λ_α at electron temperatures between ~4 and 20 keV:

$$\rho\lambda_\alpha = \frac{2.6 \times 10^{-6} T_e^{5/4}}{1 + 1.45 \times 10^{-6} T_e^{5/4}} \times [1 + 0.3 \log(\rho/\rho_0)] \quad \text{(g/cm}^2\text{)}. \qquad \text{(VII.10)}$$

At $\rho = 10^3$ g/cm³ and $T_e = 10^4$ eV, we find $\rho\lambda_\alpha \approx 0.5$ g/cm². Thus the α particles would be well contained in the sample reactor pellet being discussed here.

B. Reactor energy balance, pellet gain and laser energy

We can apply the reactor power flow diagram of Fig. 9 to the laser case by substituting the energies in parentheses for the powers. The energy E_{out} is related to the laser energy input E_{in} to the pellet by the ratio

$$Y_R = E_{\text{out}}/E_{\text{in}}. \qquad \text{(VII.11)}$$

This quantity is often called the yield ratio Y_R in the laser literature (Clarke *et al.*, 1973). We define an implosion efficiency

$$\eta_{\text{imp}} = E_{ie}/E_{\text{in}}, \qquad \text{(VII.12)}$$

which will be small because the laser input energy ablates pellet material into a cloud of expanding plasma whose velocity is much larger than that of the compressing core and which continues to absorb laser light. Implosion calculations predict $\eta_{\text{imp}} \approx 0.08$. Thus

$$Y_R = \eta_{\text{imp}}(E_{\text{out}}/E_{ie}). \qquad \text{(VII.13)}$$

In Fig. 9 the other energies are obvious analogues to the more conventional power quantities, with the injection efficiency being that of the laser and optical system

$$\eta_I = E_{\text{in}}/E_c, \qquad \text{(VII.14)}$$

where E_c is the input electrical energy to the laser system whose light output energy is E_{in}. It is expected that lasers for eventual reactors may have an efficiency $\eta_I \approx 0.1$. Finally we have for the circulating energy (power) fraction

$$\epsilon = 1/\eta_I \eta_T Y_R, \qquad \text{(VII.15)}$$

where the thermal conversion efficiency $\eta_T \approx 0.4$. Substituting (VII.13), we find for the required pellet gain

$$Q = (E_{\text{out}}/E_{ie}) = (\eta_{\text{imp}}\eta_I\eta_T\epsilon)^{-1}. \qquad \text{(VII.16)}$$

For $\eta_{\rm imp} = 0.08$, $\eta_I = 0.1$, $\eta_T = 0.4$, and an allowable ϵ of 0.3, we require that $Q = 1000$. This is one order of magnitude greater than the value derived from (VII.6) and (VII.7) for the homogeneously heated sample pellet with $\rho = 1000$ g/cm³. A value $Q = 1000$ would reduce the required energy absorbed by the pellet E_{ie} from 120 kJ to a more tractable value of 12 kJ. However it is unlikely that densities much larger than 1000 g/cm³ (compressions of 4700) can be obtained in a compressed pellet.

This discrepancy in Q for homogeneously heated pellets has led to the idea of igniting only a small ($\lesssim 10\%$) central region of the pellet (Fraley *et al.*, 1973; Nuckolls *et al.*, 1973) where the temperature at ignition (10 keV) exceeds the Fermi temperature. The outer region of the pellet at ignition is Fermi degenerate ($T \approx 100$ eV). At ignition both regions have $\rho \approx 1000$ g/cm³, and the ratio of the zero-point pressure of the outer region of the pellet to that of the small inner region is small ($T_{ef}/2T \approx 0.05$). Thus the energy required to compress the pellet to ignition is approximately only that of the small central core. Hence there is the possibility of increasing the pellet gain by an order of magnitude (Fraley *et al.*, 1973; Nuckolls *et al.*, 1973). Once ignition of the central core takes place, the burn propagates outward, raising the outer portion of the pellet to ignition also. Computed yield ratios $Y_R \geq 100$ (Nuckolls *et al.*, 1972; Clarke *et al.*, 1973) implicitly rely on such propagating burn.

C. Interaction of the laser light with the pellet plasma

A quantity of fundamental importance to the interaction of laser light with the pellet plasma is the electron plasma frequency

$$\omega_{pe} = (ne^2/\epsilon_0 m_e)^{1/2}. \qquad \text{(VII.17)}$$

In terms of the vacuum wavelength of light λ_c, corresponding to ω_{pe}, we can designate a critical density n_c from (VII.17) which becomes

$$n_c \lambda_c^2 = 10^{15} \quad (\text{m}^{-1}). \qquad \text{(VII.18)}$$

Light of wavelength $\lambda = \lambda_c$ will not penetrate a plasma beyond the critical density n_c. Thus 1-μm neodymium-glass laser light will penetrate only to $n = 10^{27}$ m^{-3}, while 10-μm CO_2 laser light will penetrate to 10^{25} m^{-3} (10^{19} cm^{-3}). Since (cf., Sec. VII.A) the plasma density corresponding to solid D–T density is 4.7×10^{28} m^{-3}, it is seen that the CO_2 light is held to an outer fringe of the pellet plasma where the density is 4700 times less than at the core, while the discrepancy for Nd light is only a factor of 47. Because of suspected difficulties with energy absorption and/or transport at low densities, this indicates the possible desirability of using lasers of short wavelength. However the lasers must also have large efficiencies η_I. Present CO_2 lasers are roughly two orders of magnitude more efficient than Nd glass lasers, when both are pulsed for short times, of the order of 10^{-9} sec. Chemical HF lasers with a wavelength of approximately 3 μm appear to offer about the same efficiency as CO_2 lasers.

Laser energy absorbed by a plasma is deposited first in the electrons and then shared with the ions by means of collisions. For an underdense plasma ($\lambda < \lambda_c$) the basic absorption mechanism is inverse bremsstrahlung whereby the electrons are oscillated by the electric field of the light wave and part of the energy of motion is thermalized by Coulomb collisions with the ions. The absorption length of this process is [Dawson (1973), Eq. (13)]

$$l_{\rm IB} = 5 \times 10^{33} T_e^{3/2}/Zn^2\lambda^2 \quad (\text{m}), \qquad \text{(VII.19)}$$

where T_e is in eV, n in m^{-3} and λ in m. The absorption length of 1-μm light at 10 keV and the critical density of 10^{27} m^{-3} is 0.5 cm, while that of 10-μ light is 50 cm. Both are large compared to the 0.1-cm size of the pellet plasma cloud, the first marginally so, and the second so much so that inverse bremsstrahlung cannot be a factor in CO_2 laser light absorption.

There are however collective means of light absorption, by turbulent charge fluctuations in the plasma which are produced by the light wave and which in turn interact with the electrons to absorb their energy much more strongly than do the electrical charges of the single ions. The means of producing these charge fluctuations is by growing plasma waves which are excited by the oscillating electric fields of the incident light wave. Near the critical density, where $\lambda = \lambda_c$, these waves can be made to grow unstably, scatter, or reflect as they propagate, owing to their coupling to periodic charge fluctuations which are also induced in the plasma by the incident light wave. These are called "parametric" processes, since the coupling of the incident wave to the induced charge fluctuations is analogous to the coupling of a harmonic oscillator to periodic changes in its spring constant, which lead to classical parametric oscillations. In a second type of collective absorption process, called resonant absorption (Friedberg *et al.*, 1972) large-amplitude plasma waves are excited near the critical density and absorb energy by wave breaking.

The net result of the parametric effects is absorption of the laser light near the critical density and its partial reflection from that region of increasing density. This process is qualitatively illustrated in Fig. 38. References to the literature on parametric instabilities of longitudinal electron waves excited by standing oscillatory electric fields are given in Kaw and Dawson (1969), Freidberg and Marder (1971), Brueckner and Jorna (1974), and Dawson (1973). Literature references to the interaction of light waves with longitudinal electron waves (Raman scattering) and of light waves with longitudinal ion waves (Brillouin scattering), all induced by an incident light wave in a density gradient near the critical density, are given in Forslund *et al.* (1973).

An important effect of these collective interactions is the production of super thermal electrons, i.e., electrons whose mean energy is much larger than T_e of the main plasma. These electrons may remain uncoupled with the ions in the imploding fuel core (Fig. 38) or they may heat it. In either case the plasma inside the interaction region is made difficult to compress by the large heating from these electrons, and means (hollow shells or high Z impurities) may have to be found to restore the compressibility of the pellet (Kidder and Zink, 1972) by eliminating their effects.

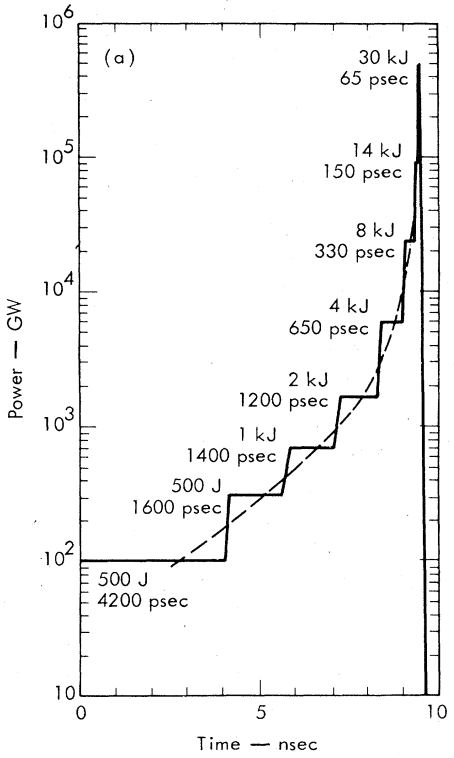

FIG. 39. Time distribution of power in a laser pulse programmed for producing burn propagation from a small central volume of a 60-μg laser pellet (Thiessen and Zimmerman, 1972, 1973).

D. Programmed pellet-compression calculations

Extensive numerical computations have been carried out at the Lawrence Livermore Laboratory (LLL) (Thiessen and Zimmerman, 1972, 1973; Nuckolls *et al.*, 1973), the Los Alamos Scientific Laboratory (LASL) (Clarke *et al.*, 1973), and by KMS Corporation investigators (Brueckner and Jorna, 1974) to study the implosion of laser pellets to compressions of the order of 10^4 by spherically incident laser light. These are hydrodynamic calculations with coupling between the light and the plasma and between electrons and ions, with photon and heat transport and with time-dependent, nonlocal α-particle energy deposition. The LLL computations are for 10 or 60 kJ of 0.5 or 1-μm laser light incident on a 400-μm radius D–T sphere (60 μg) with a 1200-μm radius low-density atmosphere (assumed to be generated by a laser prepulse) extending outward from the dense core. The LASL computations are for 10-μm laser light with energies between 2.2 and 178 kJ incident on spheres with masses between 3 and 60 μg.

The object of these calculations is to optimize the D–T fusion energy yield by computationally demonstrating heating of a small central core, surrounded by a Fermi-degenerate outer region, both with densities $\rho \approx 10^3$ g/cm^3, as discussed qualitatively in Sec. VII.B above. This is accomplished by using an especially shaped pulse of laser light power $\dot{E}(t)$ given by

$$\dot{E}(t) = \dot{E}_0(1 - t/\tau)^{-p}, \quad E \leq E_{\text{in}}$$
$$= 0, \quad E > E_n, \qquad \text{(VII.20)}$$

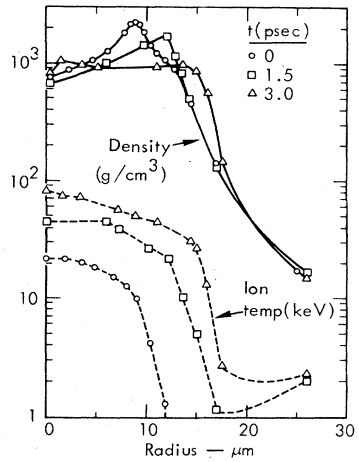

FIG. 40. Temperature and density distributions (Thiessen and Zimmerman, 1973) of a fully compressed 60-μg pellet at and slightly after ignition under the influence of the laser pulse of Fig. 39.

where (Clarke *et al.*, 1973) $p = (9\gamma - 7)/(3\gamma - 1) \approx 2$, for $\gamma = 5/3$. In the LASL calculations τ was taken between $0.5\tau_0$ and $3\tau_0$, where τ_0 is the transit time to the center of the sphere of the first shock produced by turning on the pulse. Figure 39 illustrates a 60-kJ pulse used with 60-μg spheres in the LLL calculations (Thiessen and Zimmerman, 1972, 1973). The function (VII.20) is approximated by eight successive pulses whose energies and time widths are indicated.

The initial shock from the leading edge of the pulse is near-sonic ($\sim 1/2 \times 10^6$ cm/sec), and the rising power essentially launches successive weak shocks which traverse the droplet, coalescing at a radius approximately equal to the α-particle range in D–T to give the very large near-adiabatic compression required at the center of the pellet. The shocks which precede the large adiabatic compression preferentially heat the center region because of spherical convergence, and prepare it for ignition. This is the small inner region discussed in Sec. VII.B where ignition originates and then propagates into the outer, Fermi-degenerate region which was compressed essentially along a $\gamma = 5/3$ isentrope ($T \sim n^{2/3}$, cf., Sec. II.3) as it was traversed by the weak shocks. Figure 40 shows the temperature and

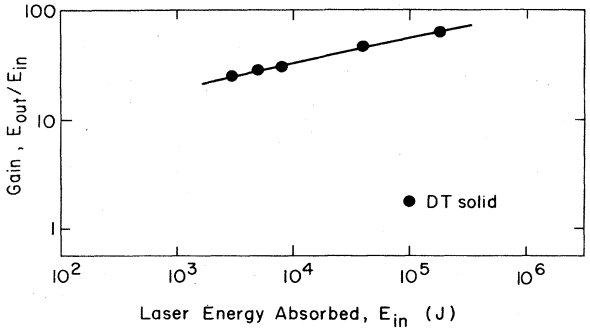

FIG. 41. Results of numerical calculations (Clarke *et al.*, 1973) of optimal yield ratio versus energy for D–T solid spheres. A value Q_T = 17.6 MeV is used [cf. Eq. (VII.6)].

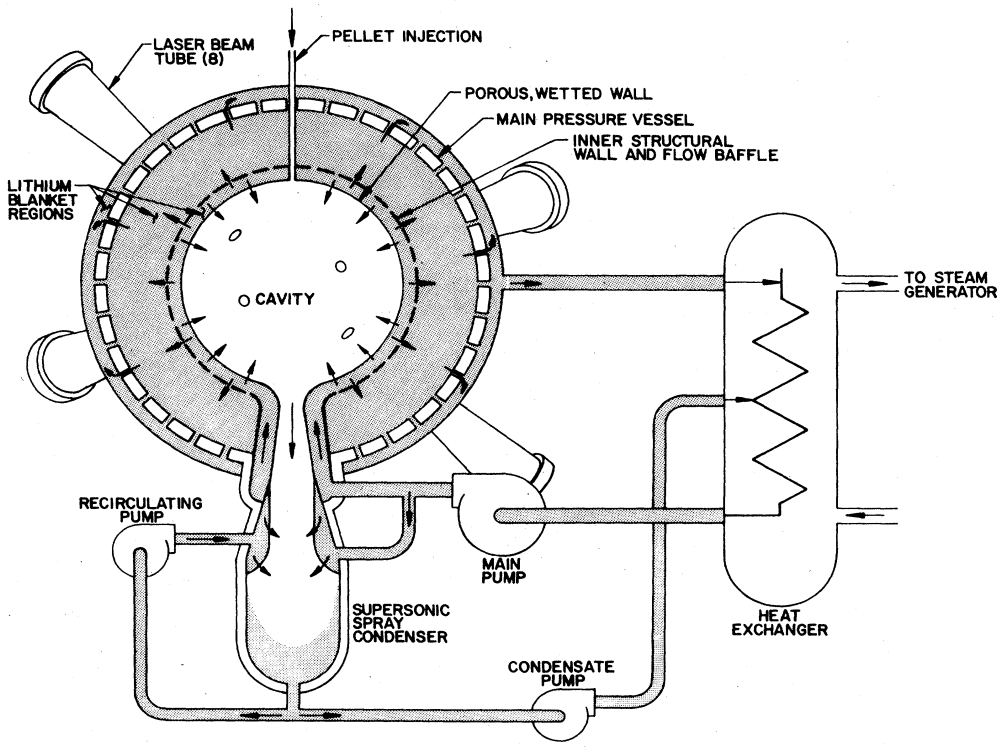

FIG. 42. Schematic diagram of a conceptual wetted-wall laser-driven D–T fusion reactor.

density distribution of the fuel core of the 60-μg LLL pellet at ignition (time zero) and for 1.5 and 3.0×10^{-12} sec thereafter, as the burn front begins to propagate outward.

In these calculations, the laser light is absorbed in the outer atmosphere of hot expanding plasma (Fig. 38) by inverse bremsstrahlung up to the critical density with the remainder being deposited at this radius by assumed anamolous mechanisms. From this radius thermal conduction carries heat to the surface of the pellet, which ablates, providing the essential mechanism for compressing and shock heating the pellet. The compressive pressure is the reaction to the outward momentum of the ablating outer region of the pellet. In these calculations the inner (fuel) region has a mass about 0.4 that the ablative region, and ablative (isentropic) compression proceeds until the internal pressure of the fuel slows the process down, after which the strong shock produces ignition in the small central volume.

Figure 41 summarizes the results of extensive numerical calculations at LASL (Clarke *et al.*, 1973) on solid D–T spheres in which for a given size the gain ratio Q (or Y_R) of Eq. (VII.12) was optimized. Gains (laser light input to pellet fusion output) approaching 100 are predicted for laser energies between 10^5 and 10^6 J. These curves provide the basic gain parameter for the conceptual fusion-reactor designs described in the next section.

E. Conceptual laser-driven fusion reactors

The central engineering problem of laser-fusion reactors is to contain the energy of the pellet explosions by the cavities' structural elements over some 10^9 to 10^{10} pulses of reactor life time. A typical pellet energy yield is 100 MJ, corresponding in energy to roughly 23 kg of high explosive. However, it has been estimated that, owing to the much smaller mass of the fusion debris, the high-explosive momentum equivalent may be reduced by three orders of magnitude (Nuckolls *et al.*, 1972). The x-rays (~4-keV peak energy) and charged particle debris from the pellet penetrate only ~10 μm and ~5 μm respectively, into first-wall materials and can lead to large temperature rises, as well as shock and fatigue effects, as can the impulse of the sudden (10^{-7} sec) heat release in the blanket by the neutrons.

From an economic point of view it is important to have a sufficiently large repetition rate of the cavity explosions that their average power output is large enough to amortize the costs of the laser system and its power supply (Hancox and Spalding, 1973). High repetition rates, approaching 10 Hz, are desirable; although, as in the theta-pinch concept, a balance must be found between favorable economy (low capital cost per kWe) and shortened core life, arising from the increased rate of radiation damage and other effects arising from the increased average neutron fluxes. A discussion of materials problems in laser-fusion reactors is given in Williams and Frank (1973). Another basic problem is that of pellet production, which to be economical, must produce D–T pellets at a cost of 0.1 to 1.0 cent each.

One of the earliest approaches to solving the first-wall problem and providing a conceptually reasonable power cycle was the wetted-wall concept (Booth, 1972), illustrated in Fig. 42. Here the D–T blast energy is absorbed by ablation and vaporization of a layer of liquid lithium on the metal first wall, causing approximately 1 kg of lithium to be vaporized from the protective layer. Sonic flow conditions of the cavity gas are quickly established at the lower outlet port, progressing to supersonic flow in a downstream length

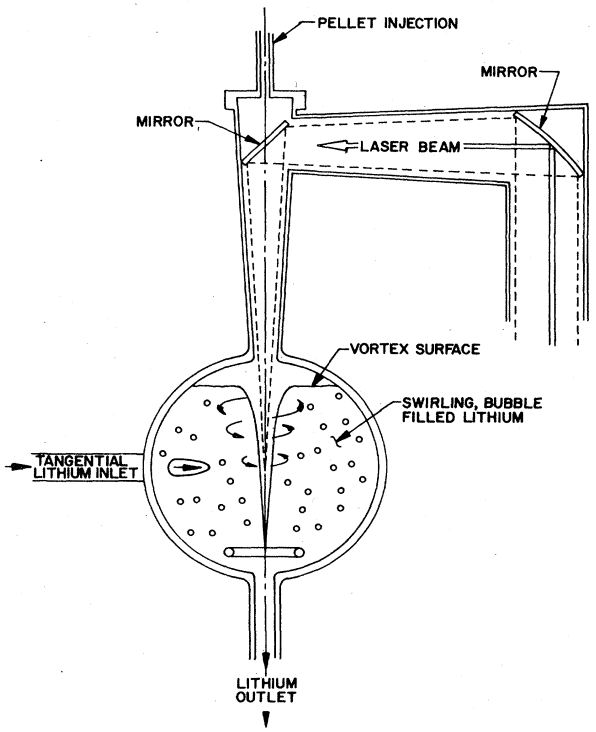

FIG. 43. Illustrating the Blascon laser-fusion reactor concept.

of duct where a finely atomized spray of lithium is injected. Finally the stream is made turbulent by the injection of larger drops and condensed at the bottom of the system. After the 1 second of the pulse cycle the cavity pressure is drawn down to less than ~1 Torr, and the cycle is reinitiated by the injection of another pellet and laser pulse. The lithium layer on the first wall is restored between pulses by radial inflow of liquid lithium through small holes in the first wall from the blanket region. The inner structural wall serves to restrain the movement of the inner blanket boundary caused by energy deposition in the blanket and cavity, and the main pressure vessel absorbs the shock load. This concept has the disadvantage of slow recovery time after a pulse in order to pump the lithium vapor density to a sufficiently low value ($\sim 10^{22}$ atom/m^3) that the laser light propagation is not impeded (Henderson, 1973).

The problem of slow recovery of the cavity gas density and of the first-wall layer is alleviated in the dry-wall concept (Williams, 1974) in which the evaporated portion of a layer of solid ablative material (carbon or beryllium) recondenses on a shorter time scale between pulses. Magnetic fields have also been proposed (Williams, 1974) in order to divert the α particles and ionized pellet debris axially along magnetic field lines to energy sinks at the ends of a cylindrical cavity.

In the Blascon concept (Fraas, 1971) of Fig. 43 the problems of fast-neutron damage to the reactor structure would be largely avoided, since the blast would be absorbed in a pool of liquid lithium which also prevents most of the neutrons from reaching the pressure vessel. The laser beam and D–T pellet are introduced into the cavity of a free vortex which is produced by the swirling pool of lithium. Bubbles of gas are introduced into the lithium to increase the absorption of the blast wave by scattering and spalling of the inner bubble surfaces. The lithium is returned through pumps to tangential nozzles in the perimeter of the pressure vessel to maintain the vortex after steady conditions of the lithium are reestablished. This requires a pellet design which will give suitable energy gain with one-sided irradiation, and care must be taken to reduce the lithium vapor pressure to allow sufficient light transmission.

F. Characteristics of a reference laser-driven power plant

Tables XIII, XIV and XV outline the main parameters of the reference laser-driven power plant based on CO_2 gas lasers driving multiple wetted-wall cavities (Williams, 1973). A conceptual-1000 MWe laser fusion power plant is

TABLE XIII. Laser characteristics of the LASL conceptual laser-driven fusion reactor based on the wetted-wall concepts.

CO_2 laser:	
Total beam energy on pellet E_{in} (J)	10^6
No. of beams per cavity (m)	8
Energy per beam, E_{in}/N (J)	0.125×10^6
Plant rep. rate (Hz)	30
Cavity rep. rate (Hz)	1.2
Laser eff. n_I	0.07
Pulse width (sec)	$\sim 10^{-9}$
Beam transport eff.	0.93
Max. laser flux on output window (J/m^2)	3×10^4

TABLE XIV. Cavity and neutron-blanket characteristics of the LASL conceptual reference laser-driven fusion reactor based on the wetted-wall concepts.

Cavities	
Radius (m)	1.7
No. of cavities	24
First wall material	1 mm Li on *Nb*
X-ray fluence per pulse J/m^2	2.5×10^4
Plasma-debris fluence, J/m^2	3.7×10^5
α-particle fluence, J/m^2	1.7×10^5
Uncoll. 14-MeV fluence[a] N/m^2/Yr.	2.3×10^{25}
Neutron blanket	
Thickness (m)	1.0
Breeding ratio	1.2
Lithium inventory, Tonne	760

[a] 85% load factor.

TABLE XV. Pellet characteristics and power balance of the LASL conceptual reference laser-driven fusion power plant, based on wetted-wall cavity concepts.

D–T pellet	
Mass (kg)	0.89×10^{-6}
Radius (m)	10^{-3}
Energy yield, E_{out} (J)	10^8
Yield Ratio, Y_R	100
Burnup, f_B	0.25
Power balance	
Thermal power, P_T (MWt)	3744
Thermal conv. eff., η_T	0.40
Gross el. power, P_E, MWe	1500
P_E per cavity, MWe	63
Circ. power frac. ϵ	0.33
Plant eff., η_P	0.27

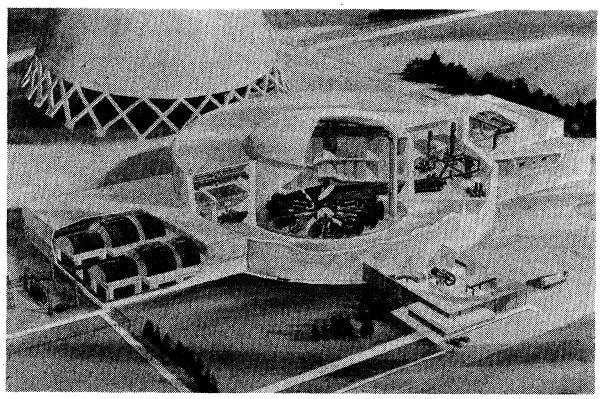

FIG. 44. Conceptual 1000-MWe laser fusion plant (Williams *et al.*, 1974).

shown in Fig. 44. It utilizes 16 separate laser amplifiers, 24 reactor cavities with associated beam-transport systems, and 12 pairs of primary lithium–sodium and sodium–steam heat exchangers. The laser beams from 8 of the 16 laser power amplifiers (Riepe and Stapleton, 1973; Williams, 1974) are reflected to 8 mirrors mounted on the central rotating assembly that successively directs the beams into the 8 beam transport tubes of each reactor cavity. The rotating mirror has an angular velocity of 1.2 revolutions per second, and the laser system has a pulse repetition rate of 29 pulses per second corresponding to a single-cavity repetition rate of 1.2 pulses per second. The reactor cavities are located in a separate, annular building surrounding the laser-system building. Each reactor cavity is in a separate shielded enclosure with penetrations for laser beams, liquid-metal coolant, and the introduction of fuel. Each reactor cavity can be isolated from the system for service and/or replacement without affecting the operation of the remainder. To achieve the gross electrical power output of 1500 MWe each of the 24 cavities produces 62 MWe. The maximum allowable CO_2 laser flux of 3×10^4 J/m^2 on the optics allows a minimum area of 4.2 m^2 for each laser-amplifier beam at its output window aperture.

The properties of the cavities and their neutron blankets are summarized in Table XIV. The neutron fluence has about the same value as for the magnetic-confinement reactors of Tables III, VII, and X. The fluences of x-rays, α particles, plasma debris (D–T ions and thermalized α particles), and neutrons account respectively for 1, 7, 15, and 77 percent of the pellet energy release. The blanket characteristics are not greatly different than those of the magnetic-confinement concepts, including the lithium inventory.

The pellet properties of Table XV are reasonable in view of the burn calculations referred to in Sec. VII.A and VII.D, and the results of Fig. 41. The basic quantity is the assumed gain [Eq. (VII.11)] of 100. The power balance assumes a modest thermal efficiency of 0.40, corresponding to stainless steel structural material. It is to be noted that the circulating power fraction of 33% is consistent with the value calculated from Eq. (VII.15) with $Y_R = 100$, $\eta_T = 0.40$, and $\eta_I = 0.07$. There is an additional requirement of 40 MW for cooling the laser gas (Riepe and Stapleton, 1973; Williams, 1974).

ACKNOWLEDGMENTS

The author acknowledges useful and interesting discussions with the following individuals, some of whom kindly read and criticized portions of the manuscript: J. F. Clarke, R. W. Conn, T. A. Coultas, D. W. Forslund, J. P. Freidberg, H. P. Furth, D. B. Henderson, R. A. Krakowski, G. L. Kulcinski, R. G. Mills, R. L. Morse, T. A. Oliphant, R. F. Post, D. Steiner, F. H. Tenney, K. I. Thomassen, R. W. Werner and J. M. Williams.

APPENDIX I. THE SCYLLAC TOROIDAL EQUILIBRIUM

When a straight theta pinch is bent into a torus (Fig. 45A), the combination of plasma pressure and the gradient of the theta-pinch compression field B_0 produces an outward force (Ribe and Rosenbluth, 1970) per unit length of the plasma column given by

$$F_R = \beta B_0^2 a^2/4R, \tag{A1}$$

where R is the major radius, a is the plasma radius, and β is the ratio of plasma pressure to the external magnetic-field pressure. The superposition of small $l = 1$ and $l = 0$ fields on the main theta-pinch field produces first-order distortions in the plasma surface of the form (cf., Fig. 45B and C)

$$r = a[1 + \delta_1 \cos(\theta - hz) - \delta_0 \cos hz], \tag{A2}$$

where $h = 2\pi/\lambda$ is the (common) $l = 1$ and $l = 0$ wavenumber, z is the toroidal coordinate, and θ is the azimuthal coordinate in a cylindrical coordinate system.

The plasma column amplitudes, δ_1 and δ_0 are related to the applied poloidal fields by

$$\delta_1 = [\epsilon(1 - \beta/2)]^{-1}(B_{l=1}/B_0), \qquad (\epsilon \ll 1), \tag{A3}$$

and

$$\delta_0 = [2(1 - \beta)]^{-1}(B_{l=0}/B_0), \qquad (\epsilon \ll 1), \tag{A4}$$

where $\epsilon = ha$ is the product of the $l = 1, 0$ wavenumber and the plasma radius. The applied poloidal field ratios, $B_{l=1}/B_0$ and $B_{l=0}/B_0$, are defined as coefficients in the expression for the (experimentally measurable) vacuum magnetic field,

$$\mathbf{B}/B_0 = \hat{e}_z[1 - (r/R)\cos\theta] + \nabla\phi, \tag{A5}$$

where $\hat{e}_z$ is a unit vector in the direction of the minor toroidal axis, and ϕ is the magnetic scalar potential.

$$\phi = (B_{l=1}/B_0)[2I_1(hr)/h]\sin(\delta - hz) + (B_{l=0}/B_0)[I_0(hr)/h]\sin hz. \tag{A6}$$

Here the I_l are modified Bessel functions. The basic $l = 1, 0$ amplitudes δ_1 and δ_0 are chosen to satisfy the toroidal equilibrium condition,

$$\delta_1\delta_0 = 2/(3 - 2\beta)h^2aR, \qquad (\epsilon \ll 1) \tag{A7}$$

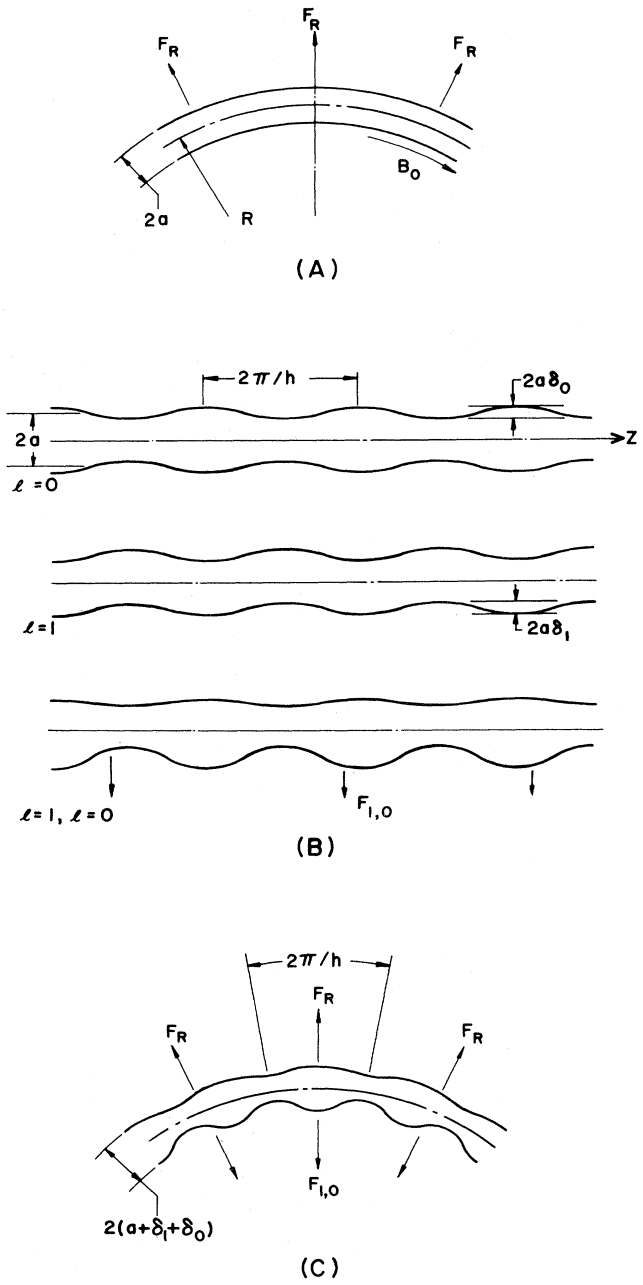

FIG. 45. (a) illustrating the outward toroidal drift force F_R on a plasma column of major radius R and minor radius a in a toroidal magnetic field B_0. (b) Illustrating the parameters involved when $l = 1$ helical and $l = 0$ bumpy fields are superposed on a plasma column to produce a uniform body force $F_{1,0}$. (c) Demonstrating the use of the $l = 1,0$ body force to produce a high-β toroidal equilibrium.

obtained by equating the toroidal drift force F_R [Eq. (A1)] to the z-independent interference (or equilibrium) force $F_{1,0}$ (Ribe and Rosenbluth, 1970) per unit length, which results from the asymmetry produced by the sum of the impressed plasma excursions δ_1 and δ_0

$$F_{1,0} = \beta(3 - 2\beta)B_0^2h^2a^3\delta_1\delta_0/8; \qquad (\epsilon \ll 1) \tag{A8}$$

(see Fig. 45).

In the Scyllac and high-β Stellarator experiments (Ellis *et al.*, 1974; Fünfer *et al.*, 1974) the toroidal configuration of Fig. 45C exhibits a single gross MHD-unstable mode whose displacement from the mirror axis of the torus is of the form

$$\xi_1 = \exp(\gamma_1 t)\exp(kz - \theta), \tag{A9}$$

where k is very small ($2\pi/k \gtrsim 300$ cm in Scyllac). According to theory (Freidberg, Marder and Weitzner, 1974a) the growth rate of this mode is given by

$$\gamma_1^2 = h^2v_A^2\left[-\beta^2\left(\frac{a}{b}\right)^4 + \frac{\beta(4 - 3\beta)(2 - \beta)}{8(1 - \beta)}\epsilon^2\right]\delta_1^2, \tag{A10}$$

where v_A is the Alfvén velocity. The first term in brackets represents a dipole wall-stabilization term due to the $l = 1$ plasma currents. However because of the strong fourth-power dependence on a/b, this term is numerically small in the present experiments. The second term represents a weakly destabilizing term arising from the $l = 1$ fields. In present Scyllac experiments, this term is being stabilized by feedback-controlled $l = 0$ fields and corresponding δ_0 amplitudes which produce a compensating $F_{1,0}$ force [Eq. (A8)] in response to the optically sensed displacement ξ_1 of the plasma column. Freidberg and Ribe (1972) give the scaling applicable to large-scale wall-stabilized Scyllac systems.

In the reactor diagram of Fig. 27 the helical plasma is indicated with an appropriate wavelength λ of about 8 m.

REFERENCES

Artsimovich, L. A., 1964, *Controlled Thermonuclear Reactions* (Gordon and Breach Science, New York).

Badger, B., *et al.*, 1973, *Wisconsin Tokamak Reactor Design* (University of Wisconsin, Nuclear Engineering Department, UWFOM-68), Vol. I.

Bell, G. I., W. H. Borkenhagen, and F. L. Ribe. See Hall and Maple (1970) p. 242.

Booth, L. A., Ed., 1972, Los Alamos Scientific Laboratory Report, LA-4858-MS, Vol. 1.

Brueckner, K. A., and S. Jorna, 1974, Rev. Mod. Phys. **46,** 361 and 332.

Bunch, J. M., *et al.*, 1973, *Proceedings of the Fifth Symposium on Engineering Problems of Fusion Reactors,* Princeton, N. J., November 6-9, 1973. (IEEE, 1973), p. 189.

Burnett, S. C., *et al.*, 1971, *Proceedings, Fourth Conference on Plasma Physics and Controlled Nuclear Fusion Research,* Madison, Wis., June 17-23, 1971. (IAEA, Vienna) Vol. III, p. 201.

Burnett, S. C., W. R. Ellis, and F. L. Ribe. See Draper (1974) p. 160.

Butler, S. T., and M. J. Buckingham, 1962, Phys. Rev. **126,** 1.

Clarke, J. C., H. N. Fisher, and R. J. Mason, 1973, Phys. Rev. Lett. **30,** 89.

Chu, M. S., 1972, Phys. Fluids **15,** 415.

Dawson, J. M., 1973, Princeton Plasma Physics Laboratory Report MATT-1004.

Draper, E. L., Jr., Ed., 1974, *Technology of Controlled Thermonuclear Fusion Experiments and the Engineering Aspects of Fusion Reactors* (Technical Information Center, USAEC).

Ellis, W. R., *et al.*, 1974, "Plasma Equilibrium and Stability in the Scylloc Toroidal Sector Experiments," Nucl. Fusion, **14,** to be published.

Etzweiler, J. F., J. F. Clarke and R. H. Fowler, 1973, Oak Ridge National Laboratory Report, ORNL-TM-4083.

Forslund, D. W., J. M. Kindel, and E. L. Lindman, 1973, Phys. Rev. Lett. **30,** 729.

Fowler, T. K., and M. Rankin, 1966, Plasma Phys. **8,** 121.
Fraas, A. P., 1971, Oak Ridge National Laboratory Report ORNL–TM–3231.
Fraas, A. P., 1973a, Oak Ridge National Laboratory Report ORNL–TM–3096.
Fraas, A. P., 1973b, AIAA Paper No. 73-259, AIAA 11th Aerospace Sciences Meeting, Washington, D. C., January 10-12, 1973.
Fraley, G. S., E. J. Linnebur, R. J. Mason, and R. L. Morse, 1973, Los Alamos Scientific Laboratory Report LA-5403-MS. Unpublished.
Freidberg, J. P., and B. M. Marder, 1971, Phys. Rev. A **4,** 1549.
Freidberg, J. P., R. W. Mitchell, R. L. Morse, and L. I. Rudsinski, 1972, Phys. Rev. Lett. **28,** 795.
Freidberg, J. P. and F. L. Ribe, 1972, Comments on Plasma Physics and Controlled Fusion, **1,** 163.
Freidberg, J. P., B. M. Marder, and H. Weitzner, 1974a, "Stability of Diffuse High Beta Helical Systems" Nucl. Fusion, **14,** to be published.
Freidberg, J. P., R. L. Morse, and F. L. Ribe. See Draper (1974) p. 812
Fünfer, E., M. Kaufmann, W. Lotz, J. Neuhauser, and G. Schramm, 1973, *Proceedings, Sixth European Conference on Plasma Physics,* Moscow, Vol. I, p. 109.
Fünfer, E., *et al.*, 1974, "High-Beta Stillwater Experiments on ISAR T1." Nucl. Fusion **14,** to be published.
Futch, A. H., Jr., J. P. Holdren, J. Killen, and A. A. Mirin, 1972, Plasma Phys. **14,** 211.
Galeev, A. A., and K. Z. Sagdeev, 1970, Sov. Phys. Dokl. **14,** 1198.
Galeev, A. A., and K. Z. Sagdeev, 1971a, Sov. Phys. JETP **32,** 572.
Galeev, A. A., and K. Z. Sagdeev, 1971b, JETP Lett. **13,** 113.
Glasstone, S., and R. H. Lovberg, 1960, *Controlled Thermonuclear Reactions* (Van Nostrand, New York).
Golovin, I. N., Yu. N. Dnestrovsky, and D. P. Kostomarov. See Hall and Maple (1970), p. 194.
Gott, Yr. V., M. S. Ioffe, and V. G. Telkovsky, 1962, *Nuclear Fusion 1962 Supplement—Part 3,* p. 1045.
Gralnick, S., 1973, Princeton Plasma Physics Laboratory Report MATT-1013.
Hall, J. L., and J. H. C. Maple, Eds., 1970, *Proceedings, British Nuclear Energy Society* (BNES) *Conference on Nuclear Fusion Reactors,* 17–19, September 1969 (UKAEA, Culham Laboratory, 1970).
Hamilton, G. W., and J. E. Osher. See Draper (1974) p. 27.
Hancox, R., and I. J. Spalding, 1973, Nucl. Fusion **13,** 385.
Henderson, D. B., 1973, Los Alamos Scientific Laboratory Report LA–5086–MS.
Hovingh, J., and R. W. Moir, 1973, Lawrence Livermore Laboratory Report UCRL–51419.
IAEA Workshop on Fusion Reactor Design Problems, Proceedings, 1974, Culham, England, Jan. 29-Feb. 15, 1974 Nucl. Fusion Special Supplement 1974 (IAEA, Vienna, 1974).
Kaw, P. K., and J. M. Dawson, 1969, Phys. Fluids **12,** 2586.
Kidder, R. E., and J. W. Zink, 1972, Nucl. Fusion **12,** 325.
Krakowski, R. A., T. A. Coultas, and A. J. Hatch, Eds., 1973, *An Engineering Design Study of a Reference Theta-Pinch Reactor (RTPR),* Joint Argonne National Laboratory and Los Alamos Scientific Laboratory Report LA-5336/ANL-8019.
Kulcinski, G. L., and Conn, R. W. See IAEA (1974), p. 51.
Lawson, D. J., 1957, Proc. Phys. Soc. Lond. B **70,** 6.
Lee, J. D., 1973, Lawrence Livermore Laboratory Report UCRL–75141.
Leontovich, M. L., Ed., 1961, *Plasma Physics and the Problems of Controlled Thermonuclear Reactions* (Pergamon, New York), Vol. I–IV.
Lubin, M. J., and A. P. Fraas, 1971, Sci. Am. **224,** No. 6, 21.
Metz, W. D., 1972, Science **177,** 1180.
Mills, R. G., See Hall and Maple (1970) p. 322.
Mills, R. G. See Draper (1974) p. 1.
Mills, R. G., Ed., 1974b, Princeton Plasma Physics Laboratory Report MATT–1050.
Moir, R. W., W. L. Barr, R. P. Freis, and R. F. Post, 1972, *Proceedings, Fourth Conference on Plasma Physics and Controlled Nuclear Fusion Research,* Madison, Wis., June 17–23, 1971 (IAEA, Vienna) Vol. III p. 315.
Moir, R. W., and R. F. Post, 1969, Nucl. Fusion **9,** 253.
Mukhovatov, V. S., and V. D. Shafranov, 1971, Nucl. Fusion **11,** 67.
Nozawa, M., and D. Steiner, 1974, Oak Ridge National Laboratory Report, ORNL–TM–4421.
Nuckolls, J., L. Wood, R. Thiessen, and G. Zimmerman, 1972, Nature **239,** 139.
Nuckolls, J., J. Emmett, and L. Wood, 1973, Phys. Today, p. 46.
Ohta, M., H. Yamoto, and S. Mori, 1971, *Proceedings, Fourth Conference on Plasma Physics and Controlled Nuclear Fusion Research,* Madison, Wis., June 17-23, 1971 (IAEA, Vienna) Vol. III, p. 423.
Oliphant, T. A., 1973, Nucl. Fusion **13,** 521.
Oliphant, T. A., F. L. Ribe, and T. A. Coultas, 1973, Nucl. Fusion **13,** 529.
Persiani, P. J., W. C. Lipinski, and A. J. Hatch, 1972, Argonne National Laboratory Report ANL–7932.
Post, R. F. 1956, Rev. Mod. Phys. **28,** 338.
Post R. F., See Hall and Maple (1970) p. 88.
Post, 1973, Phys. Today **26, 30.**
Post, R. F., and Ribe, F. L., 1974, Science **186,** 397.
Ribe, F. L., 1973, *Joint Proceedings ANS/AIF International Conference on Nuclear Solutions to World Energy Problems,* Washington, D. C., Nov. 13–17, 1972 (American Nuclear Society, Inc., Hinsdale, Ill. 1973).
Ribe, F. L., T. A. Oliphant, and W. E. Quinn, 1965, Los Alamos Scientific Laboratory Report LA-3294-MS. Unpublished.
Ribe, F. L., and M. N. Rosenbluth, 1970, Phys. Fluids **13,** 2572.
Ribe, F. L., S. C. Burnett, and W. R. Ellis, 1973, U. S. Patent 3,748,226.
Ribe, F. L., Krakowski, R. A., Thomassen, K. I., Coultas, T. A. See IAEA (1974), p. 99.
Riepe, K. B., and R. E. Stapleton, 1973, *Proceedings of the Fifth Symposium on Engineering Problems of Fusion Research,* Princeton, N. J., Nov 6-9, 1973. To be published.
Riviere, A. C., 1971, USAEA Culham Laboratory, Abingdon, England, Report CLM–R 112, Appendix 3 (unpublished).
Rose, D. J., 1969, Nucl. Fusion **9,** 183.
Rose, D. J., 1971, Science **172,** No. 3985, 797.
Rose, D. J., and M. Clark, Jr., 1961, *Plasmas and Controlled Fusion* (M.I.T. Press and Wiley, New York).
Rosenbluth, M. N., 1970, Nucl. Fusion **10,** 340.
Rosenbluth, M. N., R. Hazeltine, and F. L. Hinton, 1972, Phys. Fluids **15,** 116.
Smith, B. H., R. J. Burleigh, W. L. Dexter, and L. L. Regimato. See Draper (1974) p. 610.
Spitzer, L., Jr., 1962, *Physics of Fully Ionized Gases* (Interscience Publishers, New York).
Sweetman, D. R., 1973, Nucl. Fusion **13,** 157.
Sweetman, D. R., *et al.*, 1971, USAEA Culham Laboratory Abingdon, England, Report CLM–R 112. Appendix 7.
Tenney, F. H. See IAEA (1974), p. 17.
Thiessen, R., and G. Zimmerman, 1972, Lawrence Livermore Laboratory Report UCRL–50021–72–1, p. 103.
Thiessen, R., and G. Zimmerman, 1973, Lawrence Livermore Laboratory Report UCRL–50021–73–1, p. 195.
Werner, R. W., *et al.*, 1973, Lawrence Livermore Laboratory Report UCRL–74054–2.
Werner, R. W., G. H. Corlsor, J. Hovingh, J. D. Lee, and M. A. Peterson. See IAEA (1974), p. 171.
Werner, R. W., G. A. Carlson, J. Hovingh, J. D. Lee, and M. A. Peterson. See Draper (1974a) p. 483.
Williams, J. M. See IAEA (1974), p. 219.
Williams, J. M., in W. C. Gough, Ed., 1973, CTR Engineering Systems Study Review Meeting, AEC Headquarters, Germantown, Md., Sept. 19, 20, 1973. USAEC Report WASH-1278.
Williams, J. M. and T. G. Frank, 1973, "Laser Controlled Thermonuclear Reactor Materials Requirements," in *Proceedings of the Fifth Symposium on Engineering Problems in Fusion Reactors,* Princeton, N. J., Nov 6-9, 1973.
Williams, J. M., T. Merson, F. Finch, F. Schilling, and T. Frank, 1974, *Proceedings of the First Topical Meeting on the Technology of Controlled Nuclear Fusion,* San Diego, Calif., April 16-18, 1974. To be published.
Yang, T. F., 1973, University of Wisconsin, Nuclear Engineering Department Report RDM-49. Unpublished.

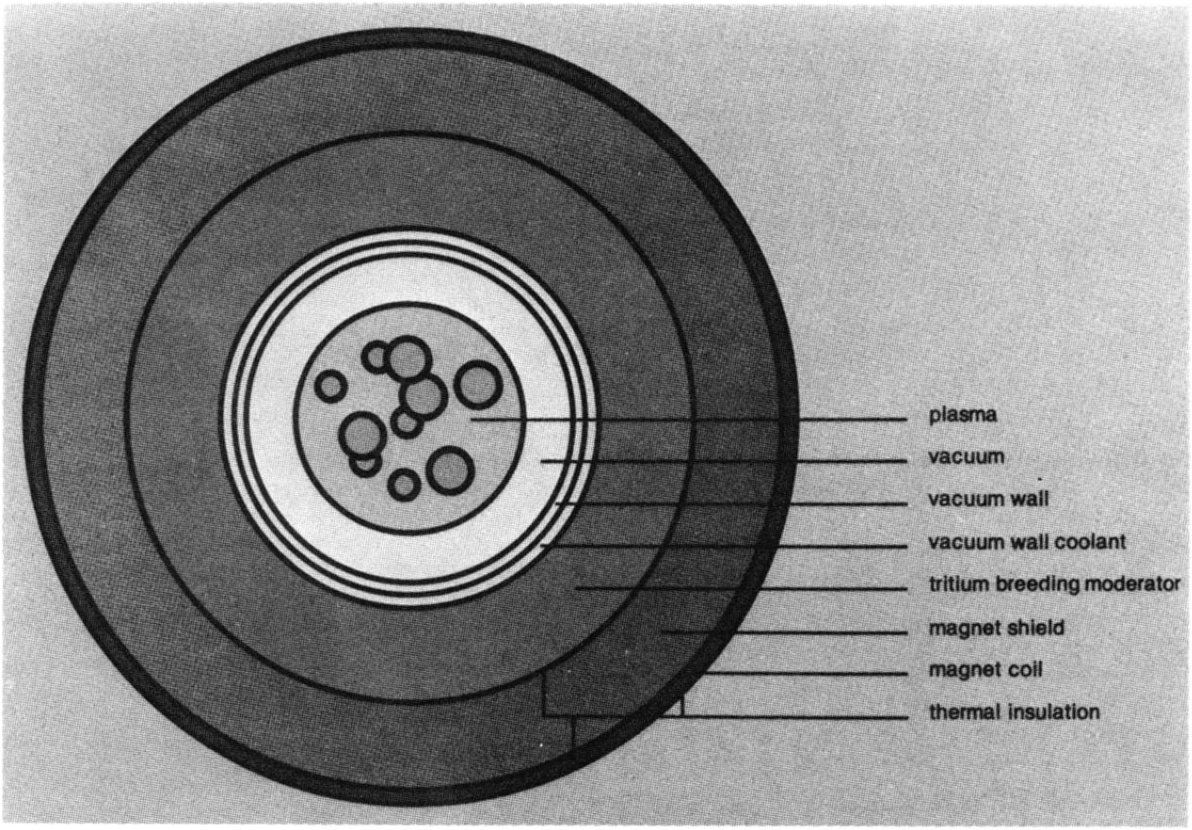

FIG. 1. Generalized cross section of a nuclear fusion reactor with magnetically confined plasma.

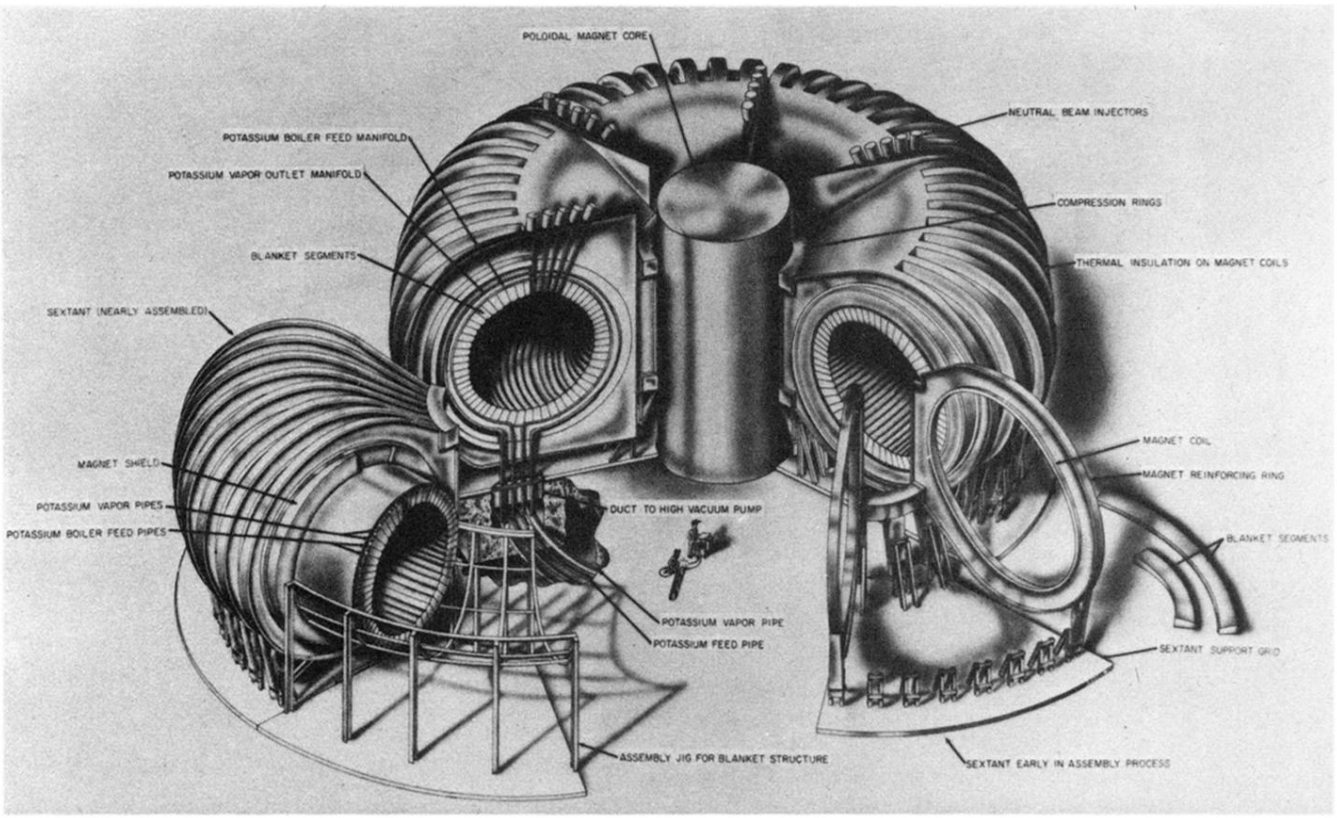

FIG. 13. General view of the ORNL conceptual tokamak fusion reactor.

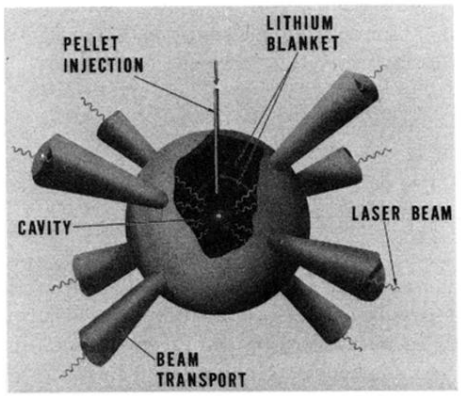

FIG. 2. Schematic view of a laser–pellet fusion reactor core.

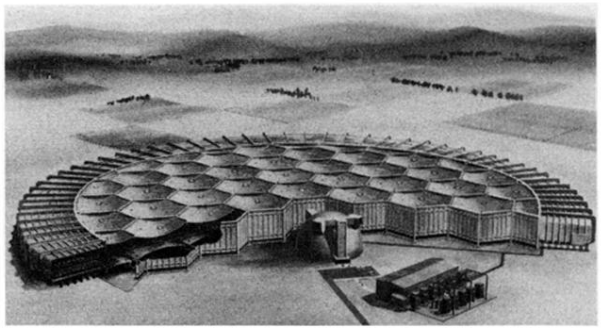

FIG. 36. Overall view of the LLL D–T magnetic-mirror fusion power plant. The direct-conversion equipment is shown behind the spherical reactor shield.

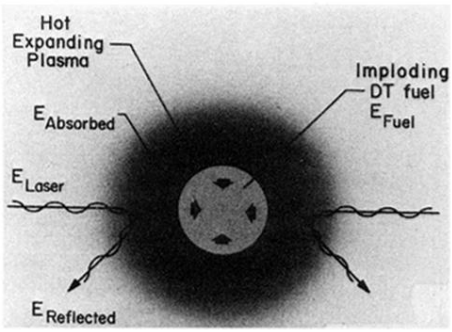

FIG. 38. Illustrating the absorption of laser light by a D–T fuel pellet in a laser-fusion reactor.

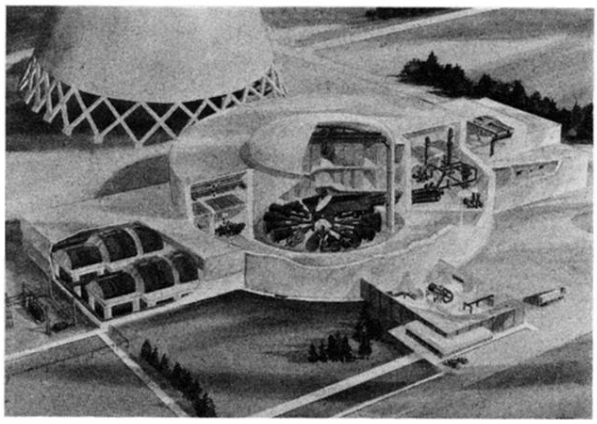

FIG. 44. Conceptual 1000-MWe laser fusion plant (Williams *et al.*, 1974).